Air-Sea Flux Measurements over the Southern Ocean

David James Tupman

Submitted in accordance with the requirements for the degree of
Doctor of Philosophy

The University of Leeds
School of Earth and Environment

August 2013

Acknowledgements

Abstract

The Waves, Aerosol, and Gas Exchange Study (WAGES) collected 18 months of near-continuous and autonomous turbulent air-sea flux estimates from the research vessel *RRS James Clark Ross*. Supporting meteorological and sea-state measurements were also made, with the objective of improving air-sea flux parameterisations. Making turbulence measurements from a ship is technically challenging, due to bias caused by platform motion and airflow distortion.

Typically, visual inspection of individual turbulence spectra is needed to quality control eddy covariance flux estimates; for WAGES the sheer volume of data motivated the development of an automated quality control method, to be performed on individual flux cospectra. The application of these tests allowed a robust relationship between the 10 m wind speed and the neutral drag coefficient to be developed, which had previously not been achieved with ship-based covariance measurements alone. This parameterisation is toward the higher end of the range of accepted values, and indicates some wind speed dependence of the Charnock parameter, rather than it being a constant.

A detailed investigation of turbulent flow distortion was made; insights into the physics were gained, and a novel correction method for motion-correlated flow distortion was developed and validated. Two major modes of motion-correlated flow distortion of the turbulence were found: one correlated to the pitch, acknowledge in the literature; a second and more powerful mode correlated to the rate of change of the pitch, not acknowledged in any publication.

The quality control and bias correction techniques developed for the momentum fluxes were transferred to a preliminary investigation of the sensible and latent heat fluxes. The uncertainty in the latent heat transfer coefficient was reduced considerably by use of the new techniques; however the sensible heat fluxes were dominated by noise, so discarded.

The methods and corrections developed in this thesis could be used to re-analyse the turbulent flux measurements from many ship-based campaigns; improving our understanding of the physics of air-sea exchange without need for additional expensive measurements.

Contents

Figures

(logarithmic) cospectral peak frequencies, and (b) the ratio of the covariances. Both parameters use the truncated ogive to remove low frequency contributions. Note the progression of the mean of both distributions from unity as thresholds are relaxed. 'Thresholds' indicates the permitted positive and negative deviation of the parameter from unity, and 'Means' the mean of the parameter within the data restricted to be within the threshold value from one

Tables

1 Introduction

The air-sea fluxes of momentum, sensible heat, and water vapour affect the circulation of both the atmosphere and the ocean. The turbulent exchanges of aerosol and trace gases are important terms in global biogeochemical cycles. The fluxes are therefore of importance to the local weather and sea-state, and to longer term climactic change.

Momentum transfer is mostly downward from the wind to the sea, acting to grow surface waves. The momentum flux also controls the turbulence intensity in the air-side and water-side boundary layers; turbulent motion controls the vertical gradients of heat and trace gas concentrations, therefore the rate of scalar exchanges across the interface. Evaporation from the oceans is a critical part of the hydrological cycle, and the surface oceans hold orders of magnitude more heat than atmosphere; both factors heavily influence the climates experienced by most of the global population. The ocean emits aerosol to the atmosphere by sea-spray; this aerosol act as nuclei for cloud droplet formation, and also directly reflects sunlight.

On a local scale, carbon dioxide transfer may be upward or downward, depending on environmental conditions, the air-sea carbon concentration gradient, and biological activity. However the global oceans are a net sink of carbon, so as the concentration of dissolved carbon increases in the surface oceans, they become a less efficient carbon sink; this is a potential positive feedback loop for global mean temperature increase. Ocean acidification is linked to increased carbon uptake, and many marine ecosystems and species are threatened. As regional ocean temperatures rise in a warming world, a greater proportion of the global ocean surface is likely to become stratified in the upper few metres. A warm shallow layer at the surface prevents vertical mixing of nutrients, effectively making the near-surface inhospitable for life.

Air-sea exchanges of momentum and energy are important to local weather, contribute to climate change, and are themselves likely to alter in response to climate change. It is therefore important to include air-sea exchanges in climate, weather, and wave forecasting models as best possible, and to identify areas of

uncertainty in our physical understanding of exchange. This allows uncertainties to be estimated in model outputs. In order to include air-sea exchange, parameterisations of the fluxes must be developed; it is impossible to explicitly include the metre- to kilometre-scale turbulent motions that control exchange, in regional- to global-scale models. Predictions of the fluxes must be made in terms of readily available mean conditions, such as the average wind speed, sea state parameters, and the air sea temperature difference.

In situ measurements of the fluxes and mean conditions can be used to develop parameterisations, and to validate modelled and remotely sensed data sets. Air-side flux measurement methods have time and spatial resolutions of tens of minutes and kilometres, respectively; this is adequate to capture changes in important flux forcing parameters such as the mean wind or sea state.

Many hundreds to thousands of individual air-side flux records are needed to compute statistically reliable relationships between the flux records and forcing parameters, because turbulently driven exchange has a high sampling uncertainty. To gather such a data set is technically challenging; measurements made from coastal flux towers are reliable but do not represent the open ocean. Publications of buoy- and mooring-based flux measurements are very recent and limited. Ships are still widely used because they are robust in high wind and seas, and readily deployable in the open ocean.

The Waves, Aerosol, and Gas Exchange Study (WAGES) collected 18 months of near-continuous and autonomous turbulent air-sea flux estimates. Time series with sampling frequencies high enough to capture turbulence were measured of: the wind vector; the temperature and humidity; the carbon dioxide concentration; and the size-segregated sea spray aerosol concentration. The objective was to use the eddy covariance, and to a lesser extent the inertial dissipation method to compute hourly-scale flux averages. Supporting meteorological and sea-state measurements were also made, with the objective of improving air-sea flux parameterisations. Large disagreements persist between parameterisation of trace gas and aerosol fluxes in terms of the ten metre mean wind speed; particularly at moderate to high wind speeds, during which wave breaking is known to have a substantial but poorly quantified influence on the fluxes. There are several causes

of disagreements between flux parameterisations that are expressed in terms of wind speed alone. Making open ocean eddy covariance measurements from a ship is technically challenging; ships are robust and mobile platforms that can be deployed in deep water and high seas, but meteorological measurements made from a ship suffer from bias caused by platform motion and airflow distortion. Additionally, the air-sea scalar fluxes are often small enough that even modern sensors suffer from poor signal to noise ratios. Also, the sea state and level of wave breaking are known to influence the fluxes, but sea state is not a deterministic function of wind speed alone. Therefore the fetch and local swell conditions cause scatter when comparing different flux parameterisations that are expressed in terms of wind speed only.

Early in the project it was found that the carbon dioxide fluxes, and measurements of the air-sea carbon dioxide concentration gradient, were too noisy to extract any useful information on the physics of exchange, or improve the parameterisation of this flux. Other members of the WAGES team were tasked with examining the aerosol fluxes. I personally examined the momentum, and sensible and latent heat fluxes. The level of disagreement between parameterisations in terms of wind speed is much lower than for carbon dioxide and aerosol; approximately 10% and 20% respectively for the momentum and sensible/latent heat fluxes.

There are no published momentum flux parameterisations that use solely ship-based open ocean eddy covariance measurements; this is because such flux measurements are consistently and obviously biased high by approximately 15-25%, when compared to a range of other measurement platforms and methods. The cause of the bias is often speculated to be a combination of airflow distortion and platform motion, because it appears as a spike in the flux cospectra at ship motion frequencies; however, no detailed investigation of this phenomenon has yet been published. Parameterisations that use inertial dissipation flux measurements have been widely published, but their validity is questioned by some because of the need for several controversial assumptions.

A literature review was first conducted, to ascertain what might be possible to achieve with the WAGES measurements, and how the measurements should be

interpreted given the likelihood of flow distortion and possible wave boundary layer effects. Following this the WAGES measurements were processed using standard published methods; a comparison of the eddy covariance, inertial dissipation, and results from a bulk flux algorithm showed the eddy covariance measurements to be extremely poor, and biased high on average by approximately 30%.

Typically, visual inspection of individual turbulence spectra is needed to quality control eddy covariance flux estimates; for WAGES the sheer volume of data motivated the development of an automated method. There are only a few published automated tests for turbulence records throughout the literature; in any case these tests were not appropriate for ship-based measurements, because the tests were developed for overland use and do not account for flow distortion bias or wave influence on the fluxes. A novel set of data quality tests, to be performed on individual flux spectra, were thus developed. The application of these tests allowed a robust and reasonable relationship between the 10 m wind speed and neutral drag coefficient to be developed, which had previously not been achieved with ship-based covariance measurements. This parameterisation is toward the higher end of the range of published parameterisations, and indicates some wind speed dependence of the Charnock parameter, rather than it being a constant. However, it is not possible to assert that the novel methods remove all forms of bias from flow distortion. It would be useful to compare the WAGES results to those from a co-located flux tower, in order to properly validate the novel method. Therefore the WAGES momentum flux parameterisation cannot at this point be concluded to be an improvement over any other parameterisation in the literature.

The novel quality control required each flux cospectrum to be interpolated over the range of motion frequencies, in order to gain sensible results. Interpolation is a purely empirical solution and has no physical justification. A thorough investigation of turbulent flow distortion was thus made; insights into the physics were gained, and a novel correction method for motion-correlated flow distortion was developed and validated. The corrected fluxes matched the interpolated results near-perfectly, except during a combination of large rolling motions, and

low wind speeds. Two major modes of motion-correlated flow distortion of the turbulence were found: one correlated to the pitch, acknowledged in the literature; a second and more powerful mode correlated to the rate of change of the pitch, not previously acknowledged in any publication.

The quality control and bias correction techniques developed for the momentum fluxes were transferred to a preliminary investigation of the latent heat fluxes. The uncertainty in the latent heat transfer coefficient was reduced considerably by use of the new techniques.

The main contribution of this thesis to the air-sea exchange scientific community is an improvement in the understanding of bias in turbulent flux measurements; bias induced by the use of a moving, bulky platform. The methods developed here could be used to re-analyse the turbulence measurements from many ship-based studies. The results from WAGES itself are fairly limited in terms of improving air-sea flux parameterisations, but re-analysis of other measurements would be relatively inexpensive and may yield significant improvements to the accuracy of flux parameterisations.

2 Literature Review

This thesis reports the analysis of ship-based measurements of the turbulent air-sea fluxes of momentum, heat, and moisture, within the lowest tens of metres of the atmospheric boundary layer. Interpreting the measurements requires an understanding of how the lower atmosphere behaves; in particular, how turbulence controls lower atmospheric fluxes, and the physics of a coupled wave-wind system. The near-surface atmospheric layer, turbulence, and air-sea exchange are first introduced qualitatively. Well established relationships between average atmospheric properties, turbulence, and vertical fluxes are discussed relating to flow over an ideal flat and homogenous surface. The physics of turbulence and air-surface interaction are more complicated in a coupled wave-wind system than over a flat planar surface, so modifications to the idealised boundary layer are discussed. Airflow distortion over the ship biases measurements; general discussion and results are then provided, with the specific modelled flow corrections used for WAGES reserved for the next chapter. Finally a literature review of air-sea momentum flux parameterisations is provided; the scalar fluxes are a minor part of this thesis so discussion of those parameterisations is reserved for the appropriate chapter.

2.1 The atmospheric surface layer above an infinite flat surface

2.1.1 Qualitative description of the surface layer

The Atmospheric Boundary Layer (ABL) is defined by Garratt (1983) as "*the layer of air directly above the Earth's surface in which the effects of the surface (friction, heating and cooling) are felt directly on time scales of less than a day, and in which significant fluxes of momentum, heat, and matter are carried by turbulent motions on a scale of the order of the depth of the boundary layer or less*". The depth of the ABL can range from several kilometres in highly convective environments such as sub-tropical deserts, to tens of metres over relatively cold surfaces, where vertical air motion is suppressed by stable stratification. The ABL is typically several hundreds of metres thick over the open ocean at mid- to high-latitudes during moderate to high wind speeds

(defined here to be greater than 5 m s^{-1}), by far the most common circumstances encountered during WAGES. There are several sub-layers within the ABL, but only the lowest tens of metres are relevant to this work.

In the molecular sub-layer, the lowest few millimetres near the surface, the vertical scalar fluxes between the sea and air are controlled by molecular diffusion, and the wind speed tends to zero due to the no-slip requirement at the interface. The rate of renewal of the thin air- and water-side layers next to the interface controls the diffusion gradient of scalars across the interface, and therefore the rate of scalar transfer. Momentum transfer in this layer manifests as force from the air acting to disturb the water surface.

Above the molecular sub-layer, in the surface layer, the wind speed increases with height logarithmically, causing shear that supports a downward directed momentum flux which is carried by turbulent motions. In the surface layer, the vertical fluxes of scalars and momentum are controlled almost completely by turbulent motion, and are nearly constant with height (to within 10% of the interfacial value; in most texts the 10% threshold defines the vertical extent of the surface layer).

Near-surface atmospheric behaviour over a flat planar surface is similar to boundary layer flow observed in engineering applications such as the effect of a floor on fluid flow. The self-similarity between boundary layer flows of all length scales (assuming high Reynolds number flow in which inertial forces dominate viscous forces) is a major underlying principle of boundary layer meteorology. The surface layer typically extends up to the lowest 10% of the ABL by height, which means that shipboard measurements taken at heights of order 10 metres are almost always within the surface layer. This allows the eddy covariance technique, a direct measure of the turbulent fluxes, to evaluate the interfacial fluxes by assuming that the turbulent flux at the measurement height is nearly equal.

The mean wind speed is zero at a surface-dependent height - named the roughness length – which is typically of order millimetres over water, even in high seas; this compared to roughness lengths over hilly terrain of order tens of metres. Over water, the roughness of the surface - i.e. how much momentum

transfer is characteristic for a given mean wind forcing - has a complex dependency on the state of the waves, themselves driven by the wind. Disagreements between studies that attempt to parameterise the open ocean roughness length persist. Above the height of the roughness length, the wind speed increases approximately logarithmically with height within the surface layer. Deviation from the logarithmic profile is controlled by the sign and gradient of the vertical air density profile. The profile controls the stability of the boundary layer; whether rising air parcels continue to rise (unstable atmosphere) or change direction and sink (stable atmosphere). In unstable conditions, when the buoyancy flux is upward, convection leads to greater vertical mixing of mean air properties, so reduction in the wind speed gradient. Conversely, in stable conditions, there is greater stratification of mean properties so the wind speed gradient is greater than logarithmic. The vertical temperature and humidity profiles have some dependency on the history of the boundary layer, but change logarithmically with height within the surface layer, assuming that the vertical fluxes of heat and water vapour are constant. It is noted that the majority of WAGES measurements were taken during near-neutral conditions, when the contribution to turbulent motion from stability is relatively weak compared to wind shear; i.e. wind shear drives most of turbulence generation.

In the surface layer, the influence of the Coriolis force is negligible, so there is little rotation of the mean wind direction with height (the Ekman spiral). The vertical gradient of wind speed causes shear stress oriented in the mean wind direction, and instabilities in the flow break down into turbulence. Momentum transfer to the ocean has contributions from shear stress and form drag (the latter manifests as wind causing the growth of surface waves). In some cases it can have an upward contribution from swell (non-locally generated waves), providing that the swell phase speed is faster than the wind speed, or the swell propagates in a substantially different direction to the wind. Swell effects on momentum exchange and the structure of surface layer turbulence are poorly understood.

Over the mid- to high- latitude oceans, the air temperature is usually slightly cooler than the ocean by up to 2 °C; this is a state of dynamic equilibrium, between radiative cooling of the air, and a sea to air sensible heat flux. Most of

the time the uppermost few metres of the sea are well mixed by wind stress, and so differences between the surface 'skin' (several molecules thick) temperature and the water temperature measured at a few metres depth are small. This is not always the case - tropical oceans can have a steep gradient in the near-surface water temperature and significant loss of surface skin layer heat due to evapouration. When the air-sea temperature difference is large, convection tends the air-sea temperature difference back to equilibrium; typical horizontal air advection speeds cannot sustain a high air-sea temperature gradient far from coasts or sea surface temperature fronts. This means almost the entire marine surface layer is weakly unstable to neutral over the open ocean. Stull (1988) gives typical ranges for sensible heat fluxes ranging from 0-30 W m^{-2} and latent heat fluxes ranging from 50-200 W m^{-2}; both upward directed.

In the marine atmospheric surface layer, at heights of tens of metres and during moderate to high wind speeds, creation of turbulence can be mostly attributed to shear stress, with weaker creation and suppression terms caused by the atmospheric density profile. Turbulence is unpredictable in terms of individual air parcel motions. However, time or spatially averaged statistics can be used to study the relationships between turbulence, vertical fluxes, and average meteorological conditions. Examples of useful statistics are the variances of the turbulent wind components, or the covariance of the turbulent vertical wind component and air temperature fluctuations about the mean (this particular covariance evaluates the vertical sensible heat flux).

The following section describes standard quantitative relationships between turbulence and average conditions. The surface layer above an ideal infinite, flat, and homogenous surface is discussed, for which many simplifications can be made. Complexities caused by coupling with the wavy ocean surface, and by airflow distortion by the ship are introduced in due course; these have implications for measuring interpreting the WAGES measurements.

2.1.2   Quantitative surface layer relationships

Any measured scalar quantity or vector component may be split by Reynolds decomposition into mean and turbulent parts:

$$A(t) = \bar{A} + A'(t) \tag{2.1}$$

where $A(\mathbf{t})$ is the quantity at time t, the overbar indicates the time average of all A, and the prime indicates the fluctuation of the instantaneous value from the mean. It is implicit that the mean of A', over all times that A is measured, is equal to zero. Hereafter, time is always assumed to be the independent variable and omitted from expressions. Four decomposition 'rules' are stated below, so called because they are not derived, but are conditions required for Reynolds decomposition; Monin and Yaglom, 1971. Below, B is a second time dependent atmospheric variable similar to A, and c is a constant:

$$\bar{A} + \bar{B} = \overline{A + B} \tag{2.2}$$

$$c.\bar{A} = \overline{c.A} \tag{2.3}$$

$$\frac{\partial \bar{A}}{\partial t} = \overline{\frac{\partial A}{\partial t}} \tag{2.4}$$

$$\overline{\bar{A}.B} = \bar{A}.\bar{B} \tag{2.5}$$

Generally, these rules require that operations (addition, multiplication, differentiation, and averaging) are commutative - the ordering of operations does not affect the final outcome. If commutation is not valid for a given variable, then manipulation and interpretation of the Reynolds decomposed equations of turbulent motion becomes impossible.

Reynolds averaging rules are valid for variables whose ensemble averaged statistics are constant. Such averages are equal to time averages of infinite series, providing that turbulent statistics are perfectly stationary. Whilst this does not occur during real turbulent flows, it can be approximated by dividing a time series into sections, providing that statistics within those sections converge to near-constant values. The choice of time series length when making turbulence measurements is very important, and usually ranges from around 10 minutes to a

few hours depending on the conditions, measurement height, and the time scales of important atmospheric processes.

Taylor's hypothesis requires that the mean wind transports turbulence past the sensor quickly enough so that the turbulence can be assumed to be unchanged during the total advection time. This allows direct comparison of spatial scales with temporal scales of turbulence. Taylor's hypothesis is valid when the standard deviation of the streamline wind component is less than half of the mean wind speed (Willis and Deardorff, 1976), a condition met almost constantly during WAGES.

The vertical fluxes of momentum (τ), sensible heat (*H*), and latent heat *(Q)* are related to the turbulent wind and scalar components by

$$\left(\overline{u'w'}^2 + \overline{v'w'}^2\right)^{1/2} = \frac{\tau}{\rho} = u_*^2 \tag{2.6}$$

$$\overline{T'w'} = \frac{H}{\rho c_p} = u_* t_* \tag{2.7}$$

$$\overline{q'w'} = \frac{Q}{\rho l_h} = u_* q_* \tag{2.8}$$

where *u*, *v* and *w* are the streamline, crosswind, and vertical components of the wind vector (m s^{-1}), *T* is the true air temperature (K), *q* is the specific humidity (kg kg^{-1}), u_* is the friction velocity, and t_* and q_* are scaling variables for the heat and water vapour fluxes; i.e. characteristic turbulent fluctuation values. τ is the wind stress (N m^{-2}), and *H* and *Q* are the sensible and latent heat fluxes (W m^{-2}). c_p is the specific heat capacity of dry air (J kg^{-1} K^{-1}) and l_h the latent heat of vaporization of water (J kg^{-1}). ρ is the moist air density (kg m^{-3}). The left hand terms in Eqs. 2.6 to 2.8 can be directly measured providing that sensors can sample the highest frequency (smallest spatial scale) turbulent motions with adequate signal to noise levels. Modern sonic anemometers and hygrometers sampling at 20 Hz can usually achieve this for typical open ocean momentum, heat and moisture fluxes.

It can be shown that the flux measured at a given height within the surface layer is approximately equal to the interfacial surface value, the latter being of more

interest to those seeking to develop air-sea flux parameterisations. The momentum conservation equation in the streamline direction is

$$\frac{\partial(\rho_d u)}{\partial t} + \boldsymbol{grad}(\boldsymbol{U}.\rho_d u) = S \qquad (2.9)$$

where $\boldsymbol{U}$ is the wind vector (with orthogonal u, v and w components); $\boldsymbol{grad}$ is the standard 3-component gradient operator, and S is the sum of the source and sink terms of momentum (i.e.: forces) in the streamline direction. The drag, Coriolis, and pressure gradient forces are all negligible within the surface layer above a flat and uniform surface, providing it is above the highest physical surface elements. In the case of oceanic measurements, these are the tops of the highest waves; at measurement heights of approximately 15 m this was not a concern for the overwhelming majority of WAGES measurements. Viscous forces are negligible in the surface layer, and buoyancy forces are only of importance in the *vertical* wind conservation equation. We can thus neglect the source term in eq. 2.9.

Density fluctuations are assumed to be negligible compared to the mean (the Boussinesq approximation), and the density term approximated as constant. If $\boldsymbol{U}$ is written as separate x, y, and z components, and Reynolds decomposition is applied, then this yields an equation with 37 terms on the left hand side. However, by assuming horizontal homogeneity and stationarity, and choosing coordinates so that the mean vertical and perpendicular wind components are zero, every term but one is found to be zero, leaving one important result:

$$\frac{\partial(\overline{u'w'})}{\partial z} = 0 \qquad (2.10)$$

Using the same assumptions, the vertical flux of any given scalar can also be shown to be constant with height by derivation from the mass conservation equation. The assumption of a constant vertical flux in the surface layer is critical to the rest of this thesis, because WAGES turbulent flux measurements were taken approximately 15 m above the ocean surface.

A set of flux measurements in isolation are of little use to the climate, weather, and wave modelling communities; co-measured mean conditions are required to develop flux parameterisations. To allow comparison of conditions between experiments, the average values (e.g. wind speed, air temperature) must be

converted from the measured height to a common standard height (10 m is used throughout the literature) using established vertical profile estimations. The correction is significant, typically of order -1 m s^{-1} for the majority of WAGES measurements. The functional form of the logarithmic vertical profile of wind speed is derived theoretically as follows.

The equations that govern molecular diffusion across a concentration gradient are adapted for turbulent exchange; flux-gradient relationships controlled by molecular and turbulent mixing behave similarly. The momentum flux is selected as an example, but similar methodology can be applied to scalars to yield logarithmic scalar profiles. The momentum turbulent diffusion equation is

$$\frac{\tau}{\rho} = K_m \frac{\partial \bar{u}}{\partial z} \tag{2.11}$$

where K_m (m^2 s^{-1}) is the turbulent diffusion coefficient for momentum. Using dimensional analysis followed by integration with respect to height, the following relation (Eq. 2.12) can be obtained and used to convert wind speeds measured at height z to their predicted value at 10 m

$$U_{10} - U_z = \frac{u_*}{k} \ln \left(\frac{10}{z} \right) \tag{2.12}$$

where U_z is the mean streamline wind speed at height z, and k is the Von Karman constant. The most commonly quoted value for k is 0.4; a range between experiments of 0.35 to 0.43 is reported in Kaimal and Finnegan (1994), although most values are close to 0.4. Eq. 2.12 is only valid in a neutrally stratified surface layer, in which the virtual potential temperature gradient and flux are zero.

The virtual potential temperature is the temperature of a dry air parcel of equal density and pressure to a given moist air parcel, brought adiabatically to a reference pressure of 1000 mb

$$\theta_v = \theta \, (1 + 0.61q) \tag{2.13}$$

$$\theta = T \, (\frac{1000}{P})^{R/c_p} \tag{2.14}$$

where θ_v is the mean virtual potential temperature (K), θ is the potential temperature (K), P is the air pressure (mb), and R is the ideal gas constant (J mol^{-1}

K^{-1}). The vertical profile of θ_v has considerable influence on the vertical fluxes, profiles, and turbulence. In unstable conditions, when the buoyancy flux is upward and θ_v decreases with height, a rising air parcel is less dense than the surrounding air and so continues to rise. Convective cells usually grow to the height of a capping inversion in θ_v at the boundary layer top. In unstable conditions the buoyancy flux is downward and θ_v increases with height, meaning that a rising air parcel is denser than the surrounding air and returns downward. This state suppresses turbulence and results in a thinner surface layer. The majority of WAGES measurements were taken in near neutral conditions, where buoyancy has little influence on the surface layer and turbulence is mostly generated by shear instability.

Monin and Obhukov (1954) proposed that above homogenous flat surfaces, the structure of surface layer turbulence can be predicted using only a few parameters: the height, the buoyancy parameter g/θ_v, and the momentum and buoyancy fluxes. They postulated that when many statistics are made non-dimensional by multiplication with combinations of the above parameters, they become functions of the stability parameter (Eq. 2.15) only; although each function must be determined empirically. The stability parameter is defined as

$$\frac{z}{L} = -\frac{(g/\overline{\theta_v})(\overline{w'\theta'_v})}{u_*^3/kz} \qquad (2.15)$$

where L is the Obhukov length (m). The stability parameter quantifies the split between wind shear and convective forcing in creating turbulence (or destroying it in stable cases).

The stability parameter is negative in unstable conditions, and the magnitude indicates the ratio of shear and convectively driven turbulence generation; if $|z / L|$ is greater than 1 then buoyancy forces contribute more. The validity of similarity theory has been proven in many experiments, and dimensionless functions empirically derived using flux and profile measurements (e.g.: Hogstrom, 1988; Businger et al., 1971) made over flat homogenous land surface types. Similarity theory has also been validated over the open ocean (e.g.: Edson et. al., 1998; Edson et al., 2004) and the open ocean dimensionless equations

match those from over land studies well – providing that the measurement height is above the direct influence of the waves.

One critical application of similarity theory in this work is the need to correct the measured mean wind speed to a value that would be expected at 10 m – in order to compare WAGES results to other studies. If an additional stability dependent term is carried through the derivation, Eq. 2.12 is modified to become

$$U_{10} - U_z = \frac{u_*}{k}\left(\ln\left(\frac{10}{z}\right) - \Psi_m(10/L) + \Psi_m(z/L)\right) \qquad (2.16)$$

where ψ_m is the integrated stability correction for the wind profile. The empirically determined wind and scalar profile functions applied in this thesis are from the review of Dyer (1974), with integrated forms taken from Paulson (1970). A second use of similarity theory is required in order to use the inertial dissipation flux measurement technique; this is introduced after turbulence spectral features are discussed.

2.1.3 Turbulence Spectra

In order to understand turbulence and fluxes, and to identify records with unusual behaviour, spectral representations of turbulent statistics are commonly used. Fourier transforms can be performed on single time series to produce power spectral densities (Eq. 2.13), or on the product of two time series to produce cospectral densities. The variance and spectrum are related by

$$\sigma_u{}^2 = \int_0^\infty S_u(f)df \qquad (2.17)$$

where $\sigma_u{}^2$ is the horizontal wind variance ($m^2 \ s^{-2}$), $S_u(f)$ is the power spectral density of horizontal wind ($m^2 \ s^{-2} \ Hz^{-1}$), and f is the frequency (Hz). Figure 2.1 shows a typical 30 minute time series of horizontal wind speed measured during WAGES, and the corresponding power spectral density.
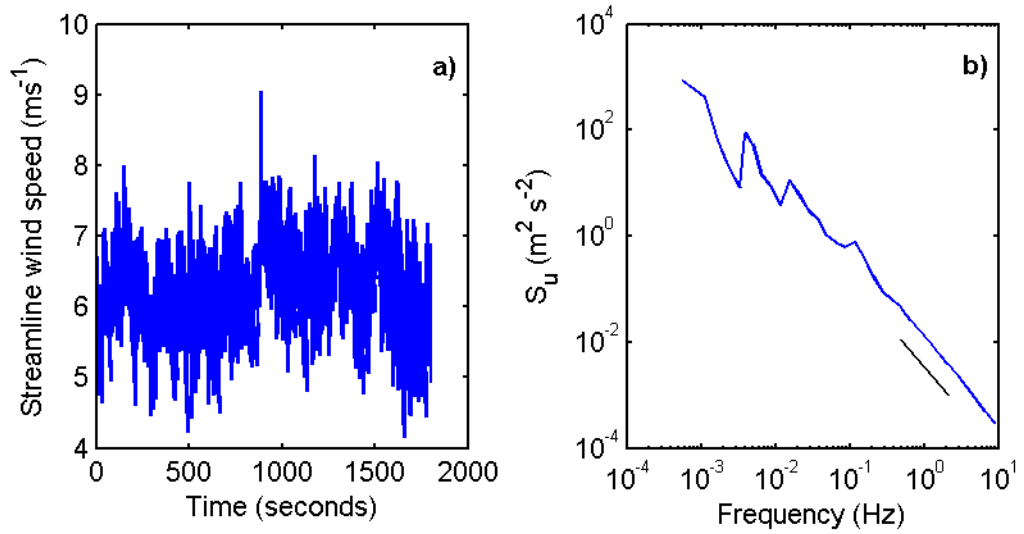
Figure 2.1 – a) Time series and **b)** power spectral density (S_u) of a 30 minute series of the streamline wind speed u. The black line in **b)** shows the predicted -5/3 gradient

The energy-containing region, around 0.01 Hz in this example, contains most of the wind variance. This part represents the largest eddies; their size is controlled by height and stability in neutral and stable cases, and by the full boundary layer height in unstable cases (Kaimal et al., 1972). Turbulence in this example (measured during moderate wind speed and a low positive heat flux - near neutral stratification) was generated mostly from vertical wind shear, and so the largest vertical motion scales of these eddies are limited by the height above the sea surface (about 15 m).

Progressing toward higher frequencies, into the inertial subrange, there is a well constrained -5/3 gradient, which was theoretically predicted by Kolmogorov (1941) who postulated that the rate of energy loss through dissipation *solely* controls the transfer rate of energy from larger to ever smaller scales in the inertial subrange. Using dimensional arguments it can be shown that

$$S_u = \alpha . \varepsilon^{2/3} . f^{-5/3} . \left(\frac{2\pi}{U_z}\right)^{-2/3} \tag{2.18}$$

where ε is the dissipation rate of turbulent kinetic energy (TKE; $m^2\ s^{-3}$), and α is the Kolmogorov constant. The choice of the Kolmogorov constant is reviewed by Hogstrom (1996), who recommends 0.52, with an uncertainty of ±0.02. Eq. 2.18 implies that a measurement of the spectral density in the inertial subrange can be used to accurately compute the dissipation rate of TKE. This can be used to estimate the momentum flux, as follows. The TKE budget equation is defined by

$$\frac{\partial \overline{e}}{\partial t} = -(\overline{u'w'})\frac{\partial \overline{u}}{\partial z} + \frac{g}{\theta}(\overline{\theta'w'}) - \frac{1}{\rho}\frac{\partial(\overline{P'w'})}{\partial z} - \frac{\partial(\overline{ew'})}{\partial z} - \varepsilon \qquad (2.19)$$

where e is the turbulent kinetic energy per unit volume ($m^2\ s^{-2}$). Assuming that the time derivative on the left hand side is zero, and normalising by the parameter $k\,z\,/\,u_*^{\,3}$, the non-dimensional terms are

$$0 = \varphi_m - \frac{z}{L} - \varphi_\in - \varphi_t - \varphi_p \qquad (2.20)$$

where φ_m is the production term for shear generated turbulence, $z\,/\,L$ represents the production or loss due to the buoyancy flux, $\varphi_\in$ is the loss term from dissipation, φ_t and φ_p are turbulent and pressure transport terms According to similarity theory each term is a function of stability only; the functions have been empirically determined numerous times over land, with good agreement between studies (Dyer and Hicks, 1970; Wyngaard and Cote, 1971; Kaimal et al., 1972; Champagne et al., 1977; Dyer and Bradley, 1982).

If the two transport terms can be neglected, then the dissipation term is simply the sum of the shear and buoyancy terms; all locally generated turbulence is dissipated locally. Substituting $u_*^{\,2}.\varphi_m/kz$ for ε in Eq. 2.20, and replacing the normalised dissipation term with the normalised shear and buoyancy terms, yields

$$\frac{f.S_u(f)}{u_*^{\,2}} = \frac{\alpha}{(2\pi k)^{2/3}}[\varphi_m - z/L]^{2/3}\left(\frac{fz}{U}\right)^{-2/3} \qquad (2.21)$$

Therefore if the well-known stability-dependent form of the non-dimensionalised shear term is applied, it follows that the momentum flux can be calculated by rearranging Eq. 2.21 in terms of u_*. This is the inertial dissipation (ID) flux

estimation method; analogous relationships between scalar spectra and dissipation allow calculation of scalar fluxes using this method.

The validity of the ID method for air-sea flux estimation is the subject of debate (Janssen, 1999; Taylor and Yelland, 2001; Janssen, 2001); the argument being whether or not local turbulent production can be equated to local dissipation, neglecting the transport terms. Kaimal and Finnegan (1994) give the following description, appropriate over an ideal land surface: In unstable cases the transport term matches the buoyancy generation term, and the imbalance term is the difference between shear generation and dissipation. In stable cases shear generation matches dissipation and the imbalance makes up for buoyancy loss. We are however mostly concerned with near-neutral cases.

Monin and Yaglom (1971) show that in theory, the transport terms in near-neutral conditions are negligible; this is supported by the observations of Hicks and Dyer (1972), and Dyer and Hicks (1982). However, Wyngaard and Cote (1971) and Champagne et al. (1977) find that dissipation exceeds production. The cause of this is found by Hogstrom et al. (2002) to be large eddies created at the ABL top by shear instability and transported downward, leading to non-local turbulence at the surface. McBean and Elliot (1975) show that whilst the transport terms are not negligible, they usually cancel each other in near-neutral conditions. Fairall and Larsen (1986) state that transport terms are about 25% of the dissipation term at near-neutral. It is clear that even over a flat homogenous land surface, contrasting arguments about the relative importance of terms in the TKE budget persists; this casts doubt on the reliability of the inertial dissipation method. Hogstrom (1996) presents a more complete discussion of the results of TKE budget experiments and quantification of the dimensionless terms as functions of stability. Further complications are introduced over a wind-wave coupled surface, and by airflow distortion caused by the ship, discussed in due course.

Common general spectral forms have been consistently observed over land (e.g. Kaimal et al., 1972) which are similar over the ocean (e.g.: Drennan et. al., 1999; Smedman et al., 2003; Miller et al., 2008). Standard forms for the full spectra and cospectra for the neutral case are provided by Kaimal et al. (1972).

$$\frac{-fC_{uw}(f)}{u_*^2} = \frac{14.f.\left[\frac{z}{U}\right]}{(1 + 9.6.f.\left[\frac{z}{U}\right])^{2.4}} \qquad (2.22)$$

Kaimal et al. (1972) also show corrections to the standard forms to account for the stability dependence of the energy-containing region. The corrections are valid for stable conditions only, where negative buoyancy restricts the height scale of eddies. Corrections cannot be made during unstable conditions, when the height of the full ABL controls the motion scales in the energy-containing region.

2.2 Wave influences on the surface layer

Unlike fluid flow over a flat surface, or turbulent air flow over homogenous flat grassland, an air-water interface is coupled; each responds to the forcing of the other over a wide range of length and time scales. Water is a thousand times denser than air, so it responds slowly to energy input from the wind, and retains kinetic energy long after the wind forcing is removed. A full account of wind-wave coupling is far beyond the scope of this thesis; Janssen (2004) provides a comprehensive review.

Four particular issues are addressed from the literature. First, in order to rely on the eddy covariance technique, the assumption of a constant vertical flux up to the measurement height is required. Second, the effect of the waves on wind and flux spectra must be understood in order to use spectra for data quality control. Third, to reliably correct the measured wind speed to an equivalent 10 m height, the standard logarithmic profile relation must be valid, or a modification made. Fourth, the influence of wind-wave interaction and on the dimensionless TKE budget terms must be understood in order to use inertial dissipation flux estimates. A brief qualitative account of wind-wave interaction is presented first, below.

Consider an initial state: a calm sea over which a neutrally stratified and turbulent flow begins to pass. At first, the no-slip interfacial condition leads to shear stress in the vertical wind profile, and forces downward transfer of momentum to the sea, creating a surface current. This current causes shear stress with the underlying water, and a water-side turbulent layer forms. Instabilities appear at

the surface as capillary waves, increasing the aerodynamic roughness of the surface as they grow. Form drag is caused by the pressure difference between the near and lee side of the growing waves, and gravity waves begin to grow; the exchange of momentum by form drag is downward at this point. This sea state is a termed a developing pure wind sea. As the wave field develops, the wave length, peak energy phase speed and significant wave height all increase, and the wave spectrum becomes narrower. Figure 2.2 shows wave height spectra during offshore winds of fetches; the further from shore, the more developed the wave field. An overview of theoretical and empirical efforts to determine wave growth laws is provided by Janssen (2004; chapters 2 and 3).
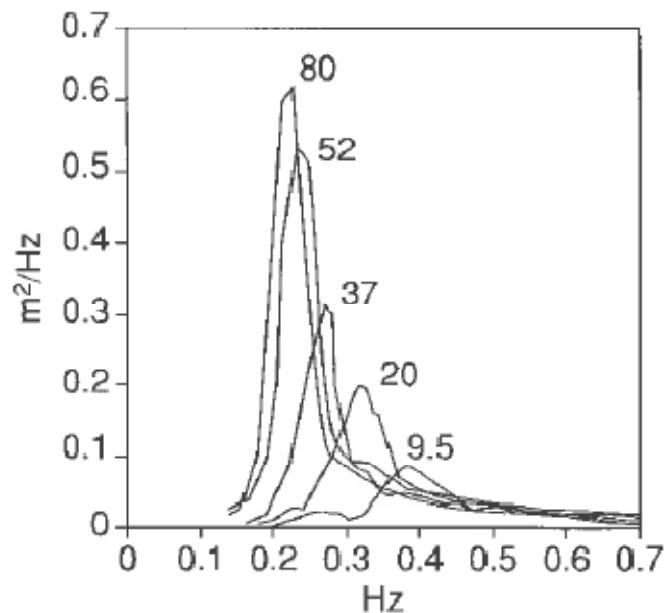
Figure 2.2 – Wave height spectra from several offshore wind cases of different fetches (shown in km), demonstrating the evolution of a pure wind sea. From Janssen (2004), who adapted the plot of Hasselmann et al. (1973).

The wave age parameter is commonly used to describe the sea state:

$$\text{wave age} = c_0 / (U_{10} . \cos \emptyset) \tag{2.23}$$

where c_0 is the phase speed of the peak energy waves, and $\emptyset$ is the angle between wind and peak wave propagation directions. When the phase speed of the peak

energy wave frequency approaches the wind speed at the wave crest height, the wave field becomes mature does not evolve further, until the wind speed or direction changes. Drennan et al. (1999), Dobson et al. (1994) and Sjoblom and Smedman (2002) give an upper limit on wave age for a developing wave field somewhere between 0.5 and 0.9. Wave ages above this threshold but below 1.2 indicate a mature or fully developed sea. Wave ages above 1.2 indicate that swell begins to dominate (Pierson and Moskovitz, 1964). The swell limit is greater than unity because the use of the 10 m wind speed is rather arbitrary; Hwang et al. (2011) discuss use of a more appropriate scaling height of half of one peak wave length. In developing pure wind seas most studies (e.g.: Drennan et al., 1999; Edson and Fairall, 1998; Sjoblom and Smedman, 2003) agree that Monin Obhukov similarity in the atmospheric surface layer is valid above heights of order one metre.

When the local wind speed drops, the waves do not immediately decay to a new equilibrium state, because of inertia. They continue to propagate, with minimal energy loss in deep water. Swell travels to other local-wind driven wave fields, thousands of kilometres away, resulting in a mixed sea with several modes in the energy spectrum and any possible combination of propagation directions. Most of the open ocean has at least some swell component in the wave field, which is why momentum transfer on average over the open ocean may be expected to be different than from coastal sites. Swell can introduce an upward directed momentum transfer component, waves pushing the air and creating a wave-induced wind jet within a thin layer just above the height of the wave crests (Hristov et al., 2003). This can cause to a wave influenced atmospheric internal boundary layer (WBL) that does not follow similarity theory or the spectra of Kaimal et al. (1972). The height of this layer can extend up to several tens of metres in swell-dominated low-wind speed conditions (2 to 5 m s^{-1} Drennan et al., 1999; Smedman et. al., 2003).

Following a change in the wind forcing, the shorter waves in the spectrum reach a new equilibrium more quickly than the longer waves, as Figure 2.3 illustrates. The top panel shows how a change in wind speed takes some time to affect the root-mean-square (RMS) wave height; the halving of wind speed over day 8

barely affects the longer and higher waves, and shows that time scales up to days may be required for equilibrium wind-wave states to be reached. The bottom panel shows that progressively longer period waves take more time to respond to a change in wind speed.
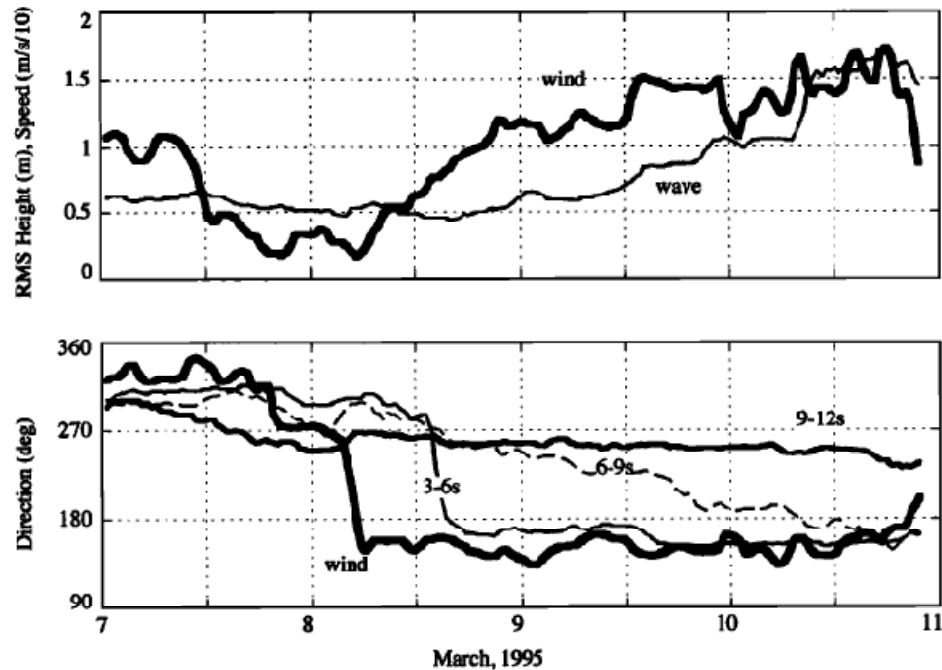
Figure 2.3 – from Reider and Smith (1998). Wind and wave time series of several days length, measured 30 miles from the Californian coast from R/P FLIP. The top panel shows the RMS wave height and wind speed. The bottom panel shows wind and wave propagation directions, for three different bands of wave period

2.2.1 Stress and turbulent spectra

Shear turbulent stress is not the only contribution to the total momentum flux, unlike over land. There is a split between the shear turbulent and wave-induced momentum fluxes (Phillips, 1977):

$$\tau_t + \tau_w = 0 \qquad\qquad (2.24)$$

where τ_t and τ_w indicate turbulent stress and wave induced momentum flux respectively. Momentum conservation demands a constant total vertical momentum flux in horizontally homogenous and stationary conditions – so one fundamental assumption required for EC (constant flux) is valid. There is however potential for flow recirculation, which invalidates Taylor's hypothesis.

Kawai (1982) used tracers to visualise flow separation and recirculation above a wave field in a laboratory - Figure 2.4 is a schematic based on the images acquired during that work. As discussed regarding the possibility of a local drag force at the measurement height, maximum wave heights during the WAGES periods studies are almost always below 15 metres, so flow recirculation is very unlikely to affect the results.
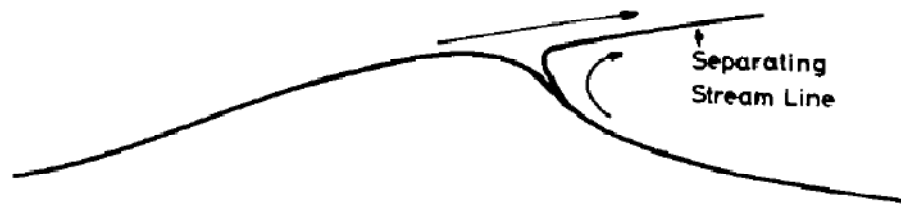
Figure 2.4 – A schematic of flow separation caused by waves from Kawai (1982)

If the measurements are taken above the recirculation zone but within the influence of the wave boundary layer (only relevant for WAGES during significant swell and low wind speeds), the wind velocity and flux cospectra no longer follow similarity expectations. The well predicted cascade of energy from the spectral peak to the viscous size ranges is interrupted by a narrow band input of energy at the longest surface wave lengths. Hristov et al. (2003) show that wave-wind energy exchange occurs in a thin layer at the height at which the wind speed is equal to the peak-energy wave phase speed. Upward momentum transfer causes an anomaly in turbulent spectra measured within the WBL at the swell wave frequencies, typically the lowest frequencies of the wave spectrum. Above the critical height the effects of the WBL decay as $e^{-\kappa z}$ (e.g.: Hwang et. al., 2011, Makin and Mastenbroek, 1996), where κ is the swell wave number (m^{-1}).

Drennan et al. (1999) measured wind and momentum flux spectra at 12 m above water level from a tower (12 m water depth) installed in Lake Ontario, that encountered both long (hundreds of km) and short (1 km) fetches. They found that when swell outran weak winds, there was a peak in the vertical wind spectrum at the lowest wave frequencies (Figure 2.5) and a smaller anomaly in the horizontal wind spectra. A similar anomaly was found in the momentum cospectra (Figure 2.6) during strong swell.
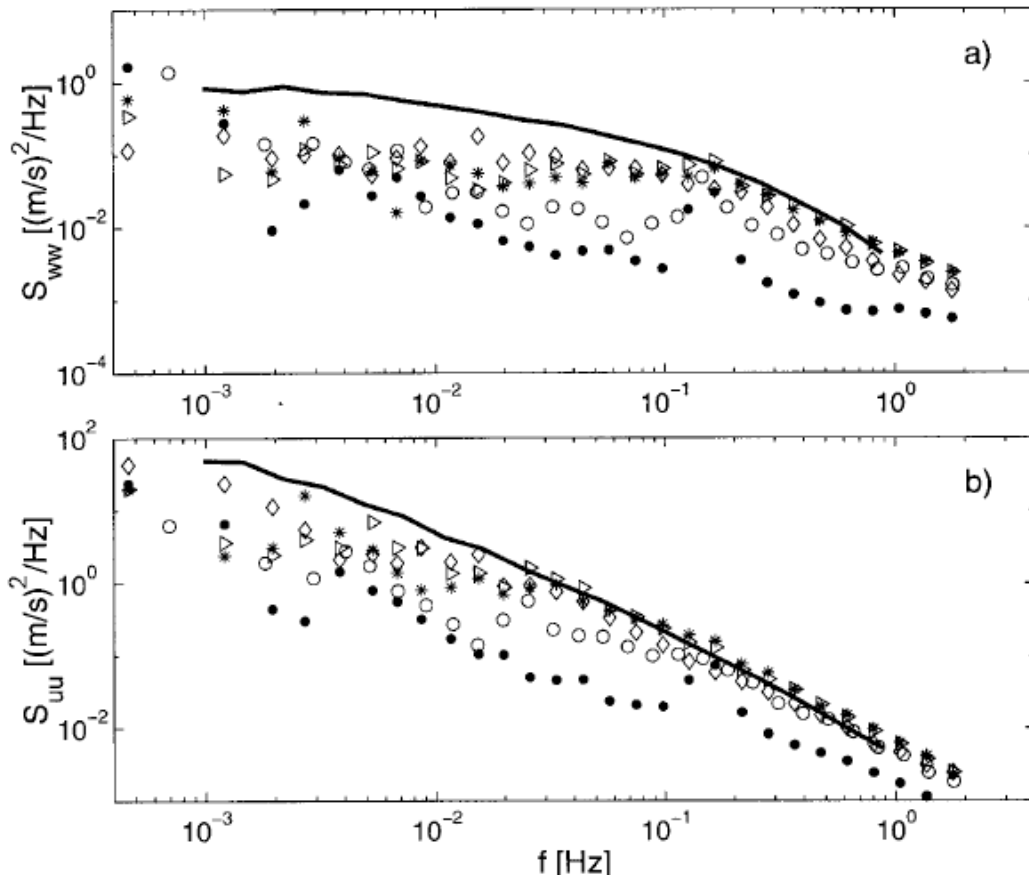
Figure 2.5 – Averaged a) vertical wind and b) horizontal wind spectra taken when swell was faster than the wind speed during the study of Drennan et al. (1999). Wave ages of all markers are 2, except for the diamonds, whose wave age is 1.6. U_{10} is 4-5 m/s. The peak just above 0.1 Hz is approximately the same as the swell wave frequency. The solid line is the averaged spectra of pure wind sea cases only, for comparison.

These anomalies occur above wave ages of 1.4, when swell is faster than the wind, over a range of U_{10N} of 2 to 5 m s^{-1}. Cases when the swell was not significantly faster than the wind (wave ages less than 1.4) did not exhibit the anomaly in the spectra. However, Smedman et. al. (2003) performed a similar study from a coastal tower in the Baltic Sea, which has a flux footprint for onshore winds similar to unlimited fetch deep water (Smedman et al 1999); although a correction had to be made to the wave spectra for shoaling. The major difference between their findings and those of Drennan et al. (1999) was that Smedman et al. (2003) observed spectral anomalies at wave ages above just 0.8, which includes mature pure wind seas as well as swell. The platform of Smedman

et al. (2003) is arguably a better representation of the open ocean due to its larger fetch and steeper coastal gradient.
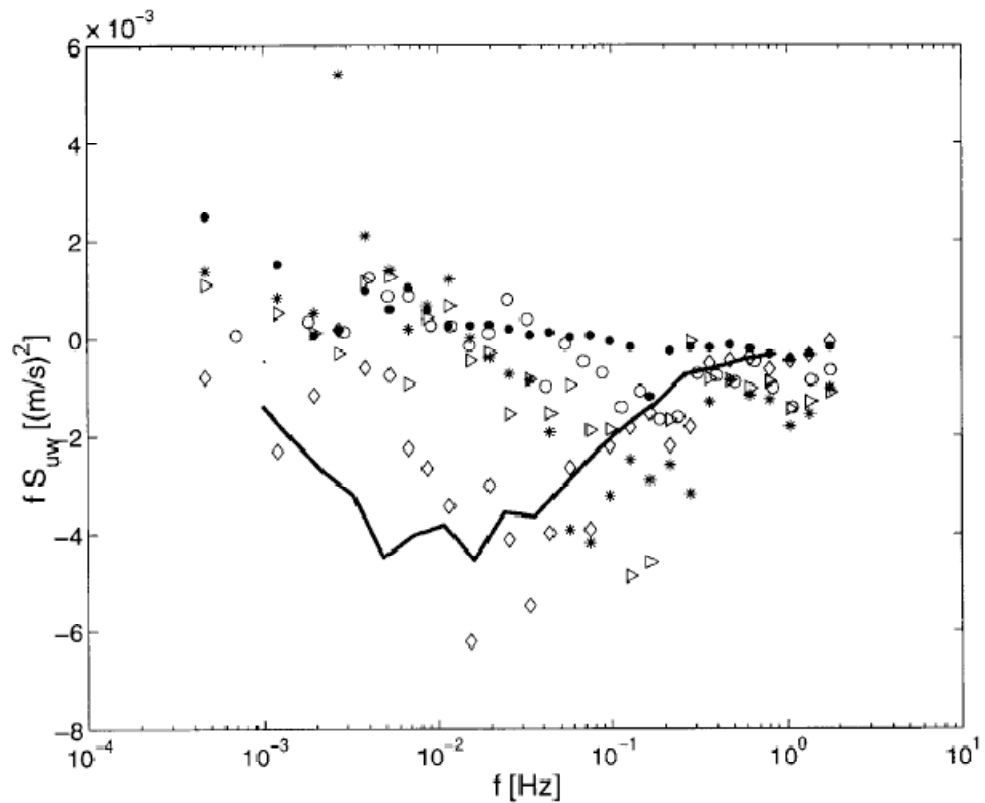
Figure 2.6 – Momentum flux cospectra measured when swell was faster than the wind speed during the study of Drennan et al. (1999). Wave ages of all markers are 2, except for the diamonds, whose wave age is 1.6 U_{10} is 4-5 m/s. The peak just above 0.1 Hz is approximately the same as the swell wave frequency. The solid line is the averaged spectra of pure wind sea cases only, for comparison.

Miller et al. (2008) acquired true open ocean momentum fluxes from a stable low flow-distortion platform (*R/P FLIP*), specifically designed minimise bias in air-sea flux measurements. They primarily discuss the effect of platform motion corrections using a motion sensor, but they also provide an example (Figure 2.7) of a set of motion corrected spectra. They only found contamination at 3.5m height in the cospectra, but in the vertical wind component, there is contamination distinguishable up to 8.7 m. The spectra shown were calculated from one record measured when the 10 m wind speed was 7 m s^{-1}.

Reider and Smith (1998) used *R/P FLIP* to measure wind stress at 8 m above sea level, with co-measured wave height spectra. They showed that the momentum flux spectrum could be split into low (0.06 Hz and less), middle (0.06 to 0.16 Hz) and high frequency (greater than 0.16 Hz) bands. Relatively, these correspond to motions at boundary layer depth scales, form drag that is well correlated with the wave height and turbulent wind stress that affects the high frequency wave spectrum. They showed that the direction of the high and low frequency stress was in the wind direction, but that the middle band was controlled by the peak energy wave propagation direction.
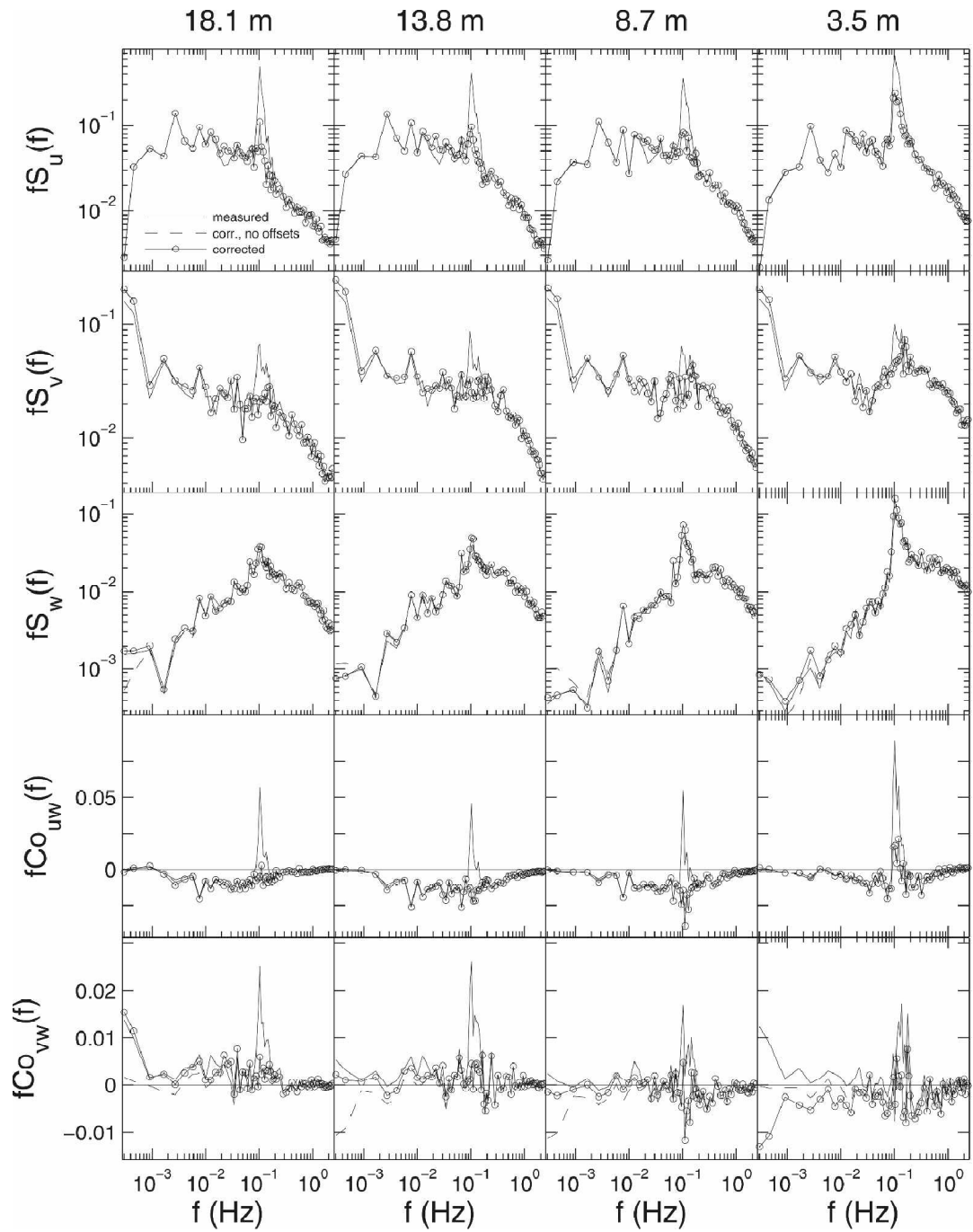
Figure 2.7 – Taken from Miller et al. (2008). Wind component spectra and cospectra measured at four heights.

2.2.2 Vertical wind profile

The mean wind speed correction (Eq. 2.16) from the measurement height to 10 m requires an assumption that the vertical wind speed profile obeys similarity theory. Most evidence (e.g.: Edson and Fairall, 1998; Hare et al., 1997; Drennan et. al 1999) suggests that except during a combination of low wind and dominant swell conditions, the standard vertical wind profiles are valid above approximately one metre. On the basis of this, the corrections applied to WAGES data were carried out as in Eq. 2.16 with confidence. However there is some evidence to the contrary from the measurements of Sjoblom and Smedman (2003). They measured the wind profiles from a coastal flux tower that has been shown (Smedman et al., 1999) to have a measurement footprint representative of the open ocean. They found three different types of profile, displayed in Figure 2.8; WAGES measurements are closest to Level 2.
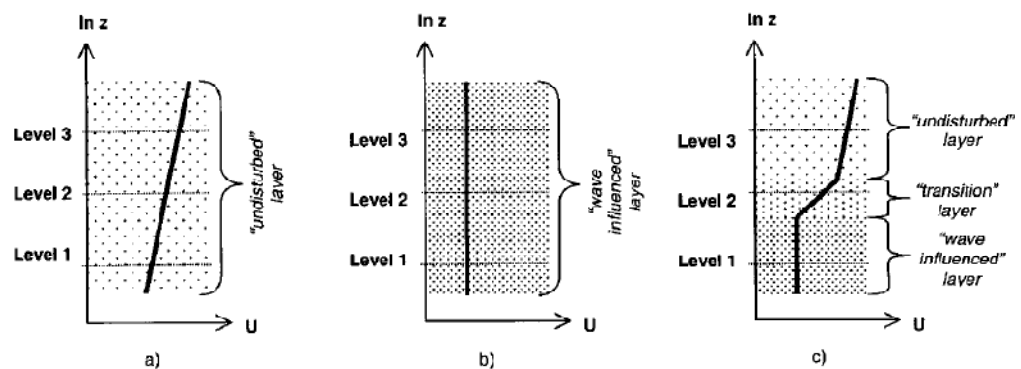
Figure 2.8 – Taken from Sjoblom and Smedman (2003). Schematics of vertical wind profiles for a) growing pure wind seas, b) swell dominated conditions and c) mature wind seas. Levels 1, 2, and 3 correspond to 10m, 18m and 26m above mean sea level.

They found that for growing seas (wave age less than 0.5), a logarithmic profile was valid, but that as the wind speed falls and the wave age increases, a transition layer develops at level 2 which is steeper than logarithmic. This is caused by the growth of a constant wind speed layer below, in response to upward momentum flux contributions from swell. This eventually results, when the wave age becomes greater than 1.2, in a constant wind speed layer of order 30 m in height.

Figure 2.9 demonstrates that for near neutral ($|z/L| < 0.025$) cases, the 18 m measurements rarely have a normalised wind gradient close to 1. This appears to

be the case only in unstable conditions, and developing seas with moderate winds. In all other conditions, the normalised wind gradient is larger than 1, up to as much as 2 at high wave ages conditions under stable stratification. That the wind profile is affected in mature seas is not prevalent throughout the literature (e.g.: Drennan et al., 1999; Hare et al. 1997; Edson and Fairall, 1998) but noted here as potential source of bias to U_{10N} computations. The coastal tower used has advantages in that air flow distortion is minimal compared to, for example, a ship. There may be flaws in the use of the tower measurements to represent the open ocean, particularly from shallow water effects, despite deep water conditions immediately offshore, where the closest point on the flux footprint is.
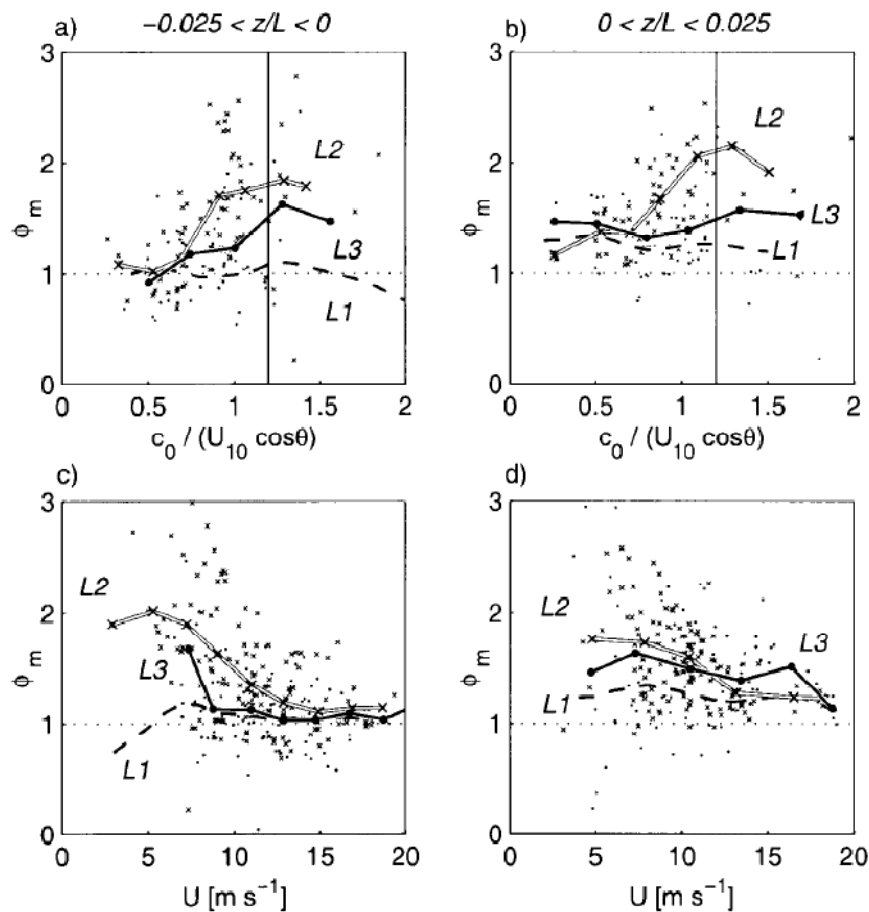
Figure 2.9 – Taken from Sjoblom and Smedman (2003). The normalised wind gradient (φ_m), versus wave age and wind speed at near-neutral (|z/L|<0.025). L1, L2 and L3 are measurement heights of 10 m, 18 m and 26 m above mean sea level. a) and c) are slightly unstable, and b) and d) slightly stable.

2.2.3 Effects on TKE terms

Several studies over the ocean support the balance of turbulent production and dissipation in near-neutral conditions (Large and Pond, 1981; Smith, 1992; Fairall and Larsen, 1986; Yelland et al 1998; Taylor and Yelland 1999). Edson and Fairall (1998) show that the stability-dependent forms of the non-dimensionalised TKE budget terms over the ocean are similar to those over land, except during slightly unstable conditions. Some suggest an imbalance term is necessary in near-neutral conditions and that the term is a function of wind speed and wave age (Dupuis et. al., 1995; Sjoblom and Smedman, 2002, Jansen et al 1999, Hogstrom 1990; Edson and Fairall 1998). All the studies listed agree that in swell-dominated and low wind speed conditions the assumption of balance is not appropriate.

Janssen (1999) argues that dissipation must be less than production, because some turbulent energy must be lost by the generation of gravity waves rather than be dissipated at the smallest scales. This manifests as an enhancement to the pressure transport term. The validity of Janssen's (1999) study was debated by Taylor and Yelland (2001) and Janssen (2001). The key points of Taylor and Yelland (2001) are that several of Janssen's (1999) predictions are simply not observed. Many authors (Edson and Fairall, 1998; Yelland and Taylor, 1996) show that a stability dependent imbalance correction term is required to remove stability dependence in ID flux results. However, Yelland et al. (1998) re-analysed the measurements of Yelland and Taylor (1996) to show that the apparent imbalance term was in fact aliased from airflow distortion effects (detailed later in section 2.3); when flow distortion was corrected for, the apparent imbalance term was removed. Taylor and Yelland (2000) show that an imbalance term is not required because the apparent imbalance term is caused by random measurement errors having a non-linear effect on average results; they could recreate the observed imbalance term by synthesising artificial measurements containing a random error term. Sjoblom and Smedman (2002) find that in near-neutral conditions, and low wave ages, production exceeds dissipation; linking their findings in to those of Hogstrom et al. (2002), who found the downward transport of large shear

generated eddies has a complex interaction with the wave field, and modulates the surface layer turbulence.

To summarise, the ID method is controversial. When comparing ID to EC fluxes, both methods must be considered to have possible bias; i.e. there is no 'gold standard' reference measurement available.

2.3 Airflow distortion

Ship-based meteorological measurements are affected by airflow distortion. The superstructure of the ship causes the mean flow to lift, and can cause acceleration or deceleration of the flow, depending on the relative wind direction. Mean flow distortion affects the interpretation of meteorological measurements, specifically: the assumption of zero vertical flux divergence; the use of the inertial dissipation method; and the computation of the neutral-equivalent 10 m wind speed (U_{N10}). Modelling studies have yielded reliable corrections for the *mean* flow and are discussed here. The influence of flow distortion caused by a *moving* platform on the *turbulent* wind measurements is much more complicated. This phenomenon is not well understood, so is the subject of a full chapter of this thesis.

Flow acceleration/deceleration invalidates the assumption of a constant vertical flux because air must flow in from elsewhere to fill the divergence/convergence region. Fortunately, flow accelerations at the WAGES turbulence sensors, for bow-on flow, are of order 1% (Yelland et al., 2002), which leads to only a small error in the assumption of a constant momentum flux gradient. Other sources of error to flux parameterisations, introduced throughout the thesis, are far larger. We therefore assume that mean airflow divergence is zero; this may not be reasonable for data sets from other ships and/or relative wind directions. For example, flow onto the beams of the WAGES research vessel is decelerated by 13%. Fluxes calculated by EC are assumed to be unbiased by *mean* flow distortion for bow on flow; i.e. *turbulent* flow distortion does affect EC flux measurements.

In order to derive flux parameterisations, the mean wind speed must be measured at a standard height, or corrected to a standard height (typically 10 m) by assuming a near-logarithmic vertical wind speed profile. Except during a

combination of low mean wind speed and swell dominating the wave field, similarity theory is obeyed at heights of tens of metres; if there were no flow distortion then Eq. 2.16 may be used with confidence to convert the measured mean wind to U_{N10}. However, airflow distortion means that inappropriate values of height (z) and wind speed at the measurement height (U_z) will be input unless corrections are applied.

The ID method requires knowledge of the height (Eq. 2.21) in order for apply parameterisations of the horizontal wind spectrum in the inertial sub rage of frequencies. Turbulence intensity is shown to take around 5 seconds to reach a new equilibrium value after a change in height (Henjes, 1996). The Computational Fluid Dynamics (CFD) modelling of Yelland et al. (2002) show that during bow-on winds, uplift of the air takes place over approximately 30 horizontal metres; approximately 2-3 seconds at typical relative wind speeds during WAGES. Therefore the measured turbulence intensity is not that expected of unimpeded flow at the sensor height, and a height displacement correction is required for the ID method.

Yelland et al. (1994) conducted a theoretical study of how sensitive the inertial dissipation flux and U_{N10} computation are to mean flow distortion. Many of their results are expressed in terms the 10 m neutral drag coefficient, CD_{N10}; defined as

$$CD_{N10} = \frac{u_*^2}{U_{N10}} \qquad (2.25)$$

Applying a typical range from the literature of the Kolmogorov constant of ±0.01 biased CD_{N10} by only 2%. A typical lift of the mean flow by 1.5 m biased CD_{N10} low by 10%. A 5% underestimate of the wind speed at the sensor height overestimates CD_{N10} by 15%. Yelland et al. (1994) also used measurements to demonstrate that flow distortion must be corrected for; they compared mean wind speeds and ID fluxes from four anemometers installed at several well-exposed positions on the foremast. They found that bias in CD_{N10} between each pair of anemometers was on average 17-27%, but between ID fluxes, the mean bias only a maximum of 3%.

CFD corrections applied to the same measurements were found to remove almost all bias between CD_{N10} from the four instruments (Yelland et al., 1998); this gives

confidence in the CFD corrections of Yelland et al. (2002) applied directly in this thesis, derived by the same research group and methods. A second and more comprehensive validation is presented by Yelland et al. (2002), who modelled a range of wind directions from -30 to +30 degrees from bow-on of flow around the *RRS Charles Darwin* and *RRS Discovery*. They found that the measured wind speed differences between several pairs of well exposed anemometers were within 2% of the modelled differences on average.

2.4 Flux parameterisations

2.4.1 Wind speed dependence

Throughout the literature, the roughness length, as an alternative to CD_{N10}, is often used to characterise momentum exchange. For consistency in this thesis, results from the literature are expressed as CD_{N10} parameterisations; converted from the roughness length if presented as such. The roughness length is defined as the height above the surface at which the neutral logarithmic wind profile tends to zero, and is derived by setting the wind speed at one height to zero in Eq. 2.12. Doing so yields

$$U_{Nz} = \frac{u_*}{k} \left(\ln \left(\frac{z}{z_0} \right) \right) \qquad (2.26)$$

where z_0 is the roughness length (m). Stull (1988) gives maximum marine roughness lengths of millimetre scales, compared to metre scales for urban areas and tens of metres for mountainous terrain.

Over land surfaces, CD_{N10} (and z_0) is usually a constant, independent of atmospheric conditions (except above surfaces such as over snow or sand, which change in response to the wind). Over water, CD_{N10} is dependent on the sea state, which itself depends on the wind history and specific contributions from swell. CD_{N10} is commonly parameterised in terms of U_{N10} in order to be used in atmospheric and ocean models. Sea state measurements from WAGES were not available at the time of writing, but the influence of sea state is discussed qualitatively in due course. However, a direct comparison of the WAGES results to U_{N10} parameterisations is possible, so a quantitative review of such studies is

provided. To summarise the findings of the review up-front; differences in CD_{N10} parameterisations of approximately 10% persist, over a U_{N10} range of 5 to 15 m s^{-1}. The spread is likely caused by differing: flux measurement techniques; specific flow distortion biases for each vessel/platform and accepted relative wind direction range; and local swell conditions. It is unlikely that a parameterisation of CD_{N10} in terms of U_{N10} alone can be any more accurate than within approximately 10% due to the influence of sea state. Details of the literature survey are presented throughout the remainder of this section.

Charnock (1953) used dimensional arguments to show that the roughness length can be parameterised by

$$z_0 = z_{CH} \frac{u_*^2}{g} \qquad (2.27)$$

where z_{CH} is the non-dimensional Charnock parameter. Charnock (1953) validated this relationship empirically and found z_{CH} to be 0.012. A constant Charnock parameter corresponds to a linear dependency of the drag coefficient on the wind speed. An additional term can be added to Eq. 2.27 to account for flow over a smooth surface, important at low wind speeds:

$$z_0 = 0.11\, v/u_* + z_{CH} \frac{u_*^2}{g} \qquad (2.28)$$

where v is the dynamic viscosity of the air (kg m^{-1} s^{-1}). This accounts for the consistently observed deviation of the roughness length from Eq. 2.28 at low wind speeds (below 4 m s^{-1}; Godfrey and Beljaars, 1991). However, measurements taken when U_{N10} was below 5 m s^{-1} are not examined in this thesis, because the relevant modelled mean flow distortion corrections are not valid in this range (Yelland et al., 2002).

CD_{N10} and z_0 can be interchanged by

$$CD_{N10} = \left[\frac{k}{\ln\left(\frac{z}{z_0}\right)} \right]^2 \qquad (2.29)$$

so z_0 parameterisations, which are provided in some publications, are converted to CD_{N10} parameterisations to allow direct comparison. The conversion is not trivial;

an iterative algorithm is required, because z_0 contains a u_* term so the conversion cannot be performed analytically. An algorithm was written that started with initial values of u_* of 0.4 m s^{-1} at all wind speeds, and Eq. 2.28 and 2.29 were iterated to convergence. Perturbing the initial value of u_* did not change the outcome, and conversions between CD_{N10} and z_0 were precise and successfully tested against several figures throughout the literature (e.g. Edson et al., 2013 provide figures of both CD_{N10} vs. U_{N10}, and z_0, vs. U_{N10}).

Several parameterisations of the drag coefficient in terms of wind speed are displayed in Figure 2.10 and discussed below. The results can be grouped into three broad groups: COARE 3.0, Edson et al, (2013) and Yelland and Taylor (1996) are the highest; Yelland et al (1998) and Smith (1980) are in the middle; and Large and Pond (1981) is a step lower. It is important to note here that no published parameterisations are based solely on uncorrected EC measurements. In fact published sets of EC momentum fluxes are rare; Edson et al (1998) show them to be biased high from realistic values by about 15% by flow distortion. Pedreros et al. 2003 find 23% high bias. The work of this thesis addresses this particular problem and in fact provides the first reasonable parameterisation based solely on ship based EC fluxes.
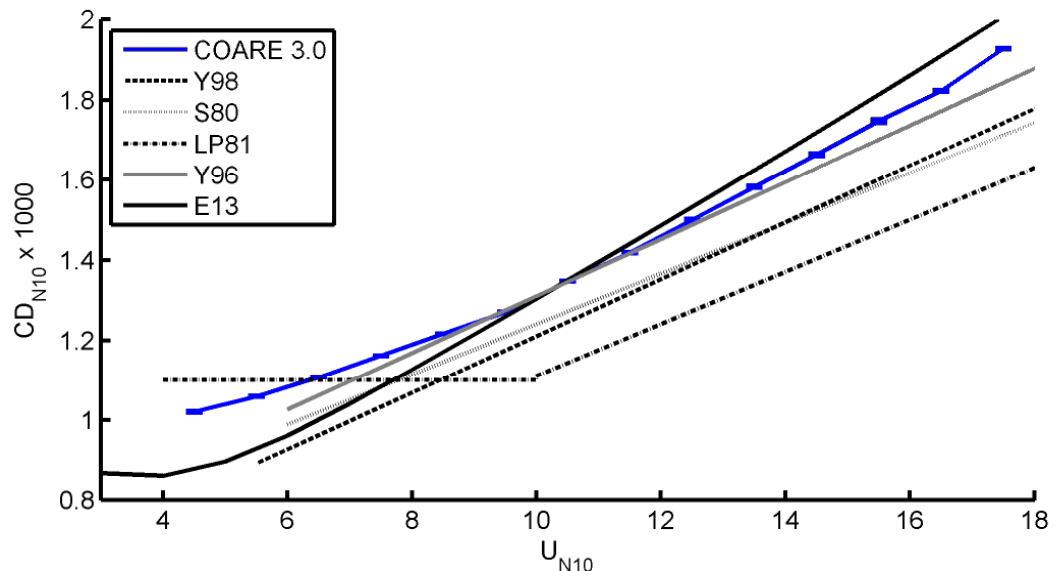
Figure 2.10 – Drag coefficient parameterisations of COARE 3.0 (Fairall et al, 2003); Yelland et al (1998; Y98), Smith (1980; S80), Large and Pond (1981; LP81), Yelland et al. (1996; Y96) and Edson et al. (2013; E13)

- 47 -

Smith (1980) used open ocean flux measurements from a stable platform with low flow distortion (the Bedford Institute of Oceanography stable platform) to obtain a Charnock parameter value of 0.011, nearly identical to Charnock's original value. Fairall et al. (1996) obtained the same z_{CH} by using a large set of measurements over the tropical open oceans (with mean 10 m wind speeds up to 12 m s^{-1}), and so a constant z_{CH} was incorporated into the bulk flux algorithm developed from that work (Coupled Ocean Atmosphere Response Experiment (COARE) bulk flux algorithm v.2.6). It was apparent that a constant z_{CH} did not model the ocean roughness adequately in moderate to high winds (greater than 10 m s^{-1}; Figure 2.11), so a wind speed dependent z_{CH} was adopted in a later COARE algorithm (v.3.0; Fairall et al., 2003). However, whilst Fairall et al. (2003) had an extensive set of measurements with U_{N10} up to 18 m s^{-1}, all measurements were made from ships/bulky platforms, without mean flow distortion corrections, and were a composite of EC and ID fluxes. The EC results were larger than the ID by about 10% on average. It is likely that COARE 3.0 is affected by flow distortion bias, but because measurements from a variety of vessels and relative wind directions were used, it is not possible to estimate the magnitude or direction of this bias.

Yelland et al. (1998) observed excellent agreement with Smith (1980). This is encouraging because a very large volume of flow distortion corrected ID measurements from over the open ocean (Yelland et al., 1998) agree well with open ocean EC measurements (Smith, 1980) taken from a platform with low flow distortion and very restricted platform motion. Compared to these two studies, the parameterisations of Large and Pond (1981) and Yelland and Taylor (1996) were biased by several percent. The bias is likely due to these studies using ship-based ID measurements without correcting for airflow distortion.
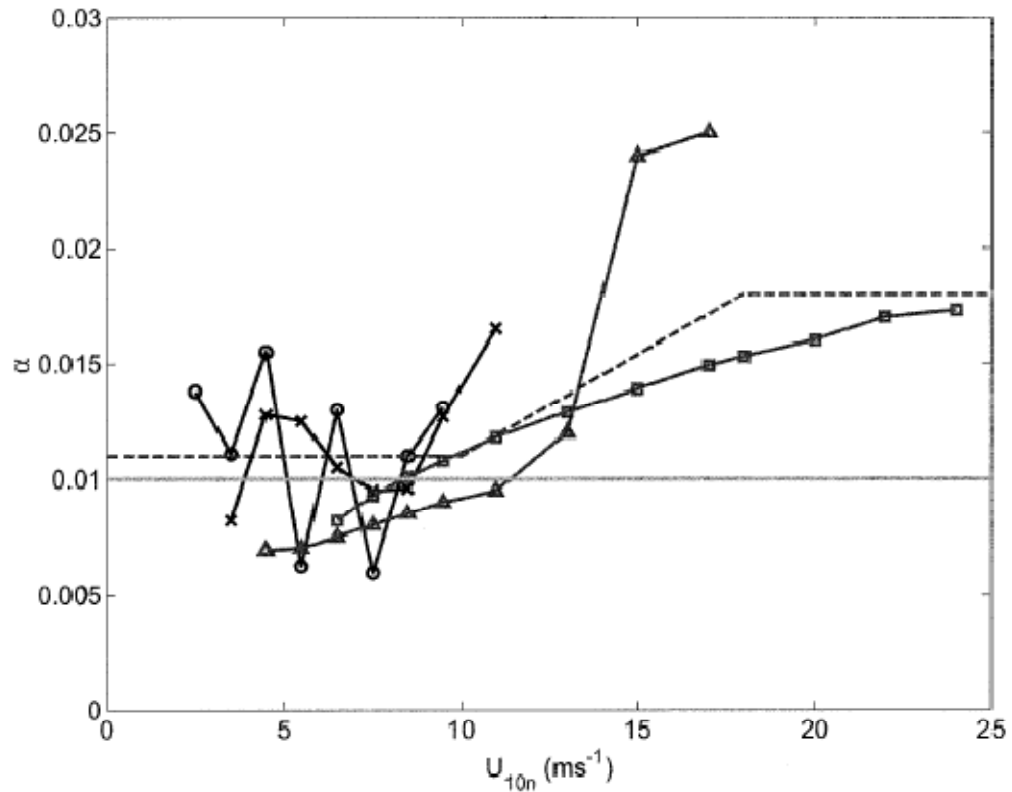
Figure 2.11 – From Fairall et al. (2003) – 'Estimates of the charnock parameter from various field campaigns: X, COARE; O, SCOPE; Δ, MBL; □, Yelland and Taylor (1996). The dashed line is the COARE 3.0 relationship'. Note that their left hand axis label (α) is equivalent to z_{CH} in this work.

There are arguments both in favour, and against, the validity of COARE v.3.0. Recent work by Edson et al (2013) used results of several measurement campaigns to derive a new wind speed dependent z_{CH} parameterisation. Results from ships were avoided; they used results from buoys and moorings (CLIMODE; Climate Mode Water Dynamic Experiment; Marshall et al., 2009) and the stable low profile research platform *FLIP* (MBL; Marine Boundary Layer Experiment; Hristov et al., 2003). At the moderate wind speed range agreement with COARE v.3.0 is found, providing some validation. The authors describe a transition from fully rough flow to smooth flow over the wind speed range 4 to 8.5 m s^{-1}. During fully rough flow the momentum flux is almost entirely caused by form drag, and in smooth flow viscosity controls the momentum flux. There is a transition regime between the two. They calculate a more gradual transition

from 4 to 8.5 m s^{-1} in an update (COARE v.3.5) to the algorithm, by using a wind speed dependent Charnock parameter. Data at very high winds is sparse but there are observations that the drag coefficient reduces toward very high wind speeds (above 25 m s^{-1}), and this new parameterisation takes this into account. This is however beyond the scope of WAGES (5 to 15 m s^{-1}).

There is some evidence from ID studies that COARE v.3.0 and Edson et al. (2013) are both biased high. The wind speed dependent z_{CH} parameterisation of Yelland and Taylor (1996) was cited by Fairall et al. (2003) as a major reason for their use of a wind speed dependent Charnock parameter at moderate to high wind speeds. Yelland and Taylor (1996) had a large set of ship-based ID flux measurements from over the Southern Ocean, a region known for well-developed sea states and long fetches, caused by the absence of boundaries in the east-west direction. However, the same research group (Yelland et al., 1998) re-analysed their data using what are now widely regarded as essential corrections for mean air flow distortion induced by the ship (e.g.: Dupuis et al., 2001; Pedreros et al., 2003). This re-analysis yielded a constant Charnock parameter (0.011). The dependency of the Charnock 'constant' on the wind speed dependent parameter is the subject of some debate, because of the concern over the validity of the ID method (e.g.: Janssen 1999). However since we are *certain* that Yelland et al. (1998) is an improvement on Yelland and Taylor (1996), this would indicate that COARE v.3.0 and Edson et al. (2013) are biased high. Although the measurements of Yelland et al. (1998) are from the Southern Ocean with a higher general level of swell; this would mean a larger upward flux contribution and a reduced overall momentum flux compared to the mid latitude studies of Edson et al (2013).

In summary, there is broad agreement to within approximately 10% between parameterisations of the drag coefficient. Each study has potential weaknesses, so it is not possible rely on one over another. Given that local swell conditions may also cause variability between studies, direct comparison of any parameterisation with WAGES may be flawed. Using a large set of ship based flux measurements alone; it was never a possibility that my own work could resolve differences between parameterisations. However, it was possible to conduct an investigation

of EC bias related to flow distortion, and development of novel correction methods relevant for ships.

2.4.2   Sea State influence

Whilst sea state measurements were not available at the time of submission, and so not possible to compare to WAGES measurements, it is of interest to review the effect on the surface drag that sea state may have, to qualitatively account for scatter from any wind speed dependent parameterisation developed from WAGES.

There is strong evidence that sea state parameters have influence on the drag. For example, Rieder and Smith (1998) used a stable open ocean platform (*R/P FLIP*) and found that 28% of the variability in CD_{N10} was related to wave age and significant wave height. Many studies have found a wave age dependency of the Charnock parameter (Smith et al., 1992; Oost et al., 2002; Johnson et al, 1998; Vickers and Mahrt, 1997); at higher wave ages the drag coefficient increases for a given wind speed. However there is disagreement between wave age parameterisations; the parameterisation developed in one study does not predict the behaviour of another well. Taylor and Yelland (2001) reanalysed the results of several campaigns. They found that a single wave height and steepness parameterisation can account for the variability in results more successfully than any proposed wave age parameterisation. Using the Taylor and Yelland (2001) height and steepness relationship, only 10% of remaining variability is fetch-dependent. This implies that young and old pure-wind seas have roughly the same CD_{N10} vs. U_{N10} relations, and only swell consistently modifies the drag.

The studies that use near coastal data (Smith et al., 1992; Oost et al., 2002; Johnson et al., 1998) are not suitable for assessment of a wave age dependency of the drag coefficient; shoaling of waves as they enter shallow water causes a rise in steepness and height, and therefore in the drag. Drennan et al. (2003) also point out that these studies suffer from a limited range of wave peak phase speed, and so the wave age variability is spurious; only the wind speed contributes significantly. Yelland et al. (1998) cast further doubt on the wave age influence by showing that variability in the drag coefficient can appear to be related to

wave age, but has a much closer correlation with the change in wind direction. The apparent wave age influence in this case is an effect aliased from flow distortion. Yelland et al., (1998) do not find a significant wave age dependence of the drag coefficient in their own data. However, Drennan et al (2005) did find that wave age parameterisations are successful when examining very young pure wind seas – with wave ages below 0.2.

The effects of swell on the drag coefficient have been studied for relatively simple cases: for example Donelan et al. (1997) find that swell opposing the wind direction increases the drag. Grachev and Fairall (2001) find that swell following the wind decreases the drag. How this impacts the average open ocean drag coefficient is likely to depend on the local swell characteristics. Reider and Smith (1998) showed if the swell-correlated momentum flux fraction was removed, CD_{N10} vs. U_{N10} relations showed much less scatter.
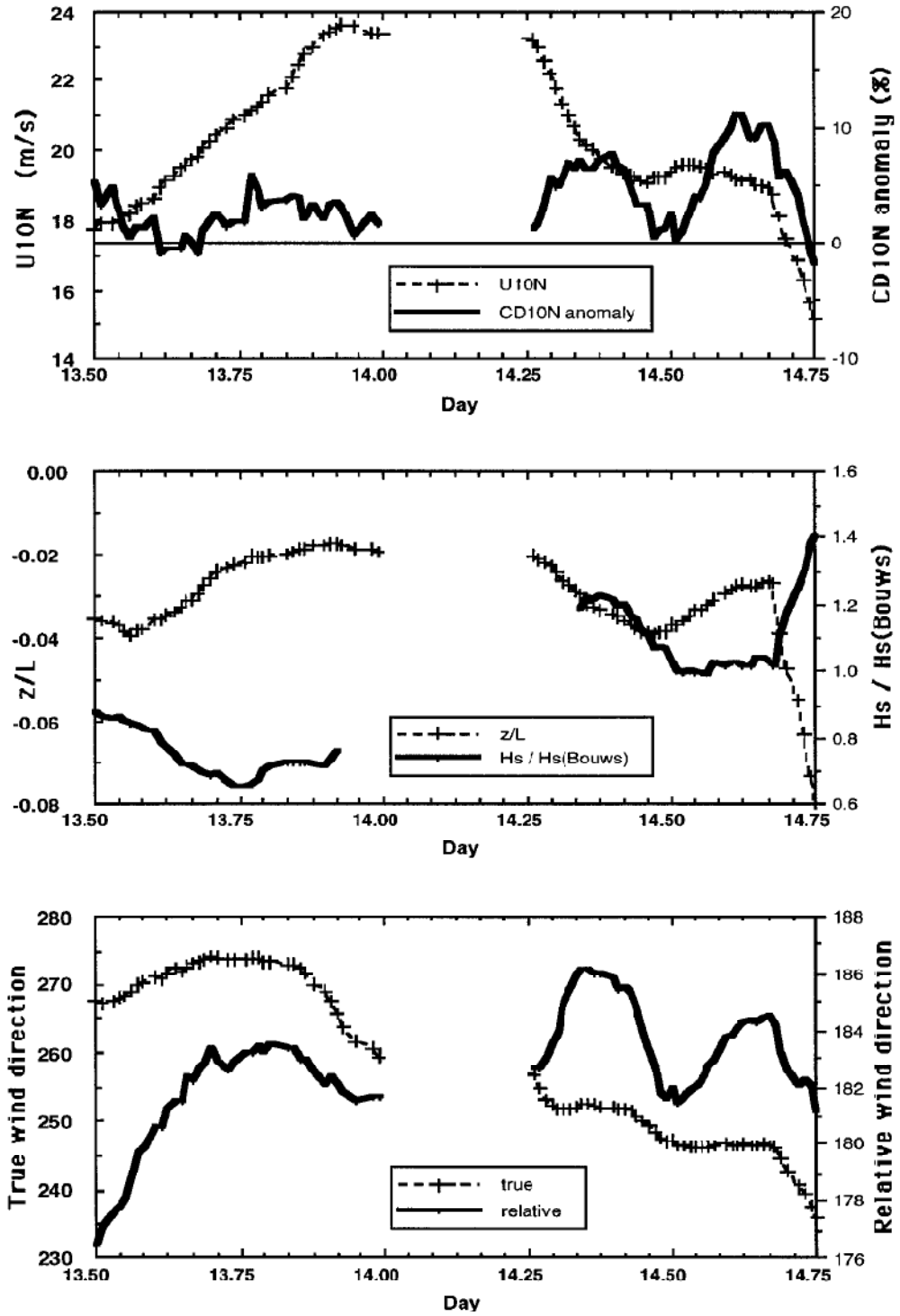
Figure 2.12 – From Yelland et al. (1998), the top panel shows the anomaly in the drag coefficient – its deviation from the expected value for that wind speed. The lower two panels show stability, wave height, true and relative wind directions; it is clear that the drag coefficient anomaly is closely correlated to the relative wind direction.

2.5   Literature review summary

This chapter had two main objectives: to verify that flux and other meteorological measurements made over the open ocean from ships can be interpreted sensibly; and to collect and critically assess a set of momentum flux parameterisations to compare my own final thesis results to. The key findings were that:

- Assumption of similarity theory and standard 'textbook' surface layer relations are valid in the marine surface layer, providing there is not a *combination* of dominant swell and low wind speeds. WAGES analysis is thus restricted to measurements during which U_{N10} is greater than 5 m s^{-1}

- Marine flux cospectra obey the standard Kaimal et al. (1972) 'bell shape', except in conditions of low wind and dominant swell

- *Mean* airflow distortion affects ID (but not EC) flux measurements, and the mean wind speed measurement. Modelled corrections are however available for WAGES and very accurate (to within 2%). No such corrections exist for *time-varying* flow distortion, which affects EC measurements and is the subject of chapter 5

- The ID method is controversial because of assumptions regarding the balance of TKE terms. It is used in this thesis as a reference measurement only

- Drag coefficient parameterisations agree to within about 10% in the moderate (5 to 15 m s^{-1}) wind speed range. Improvement is unlikely to be possible without inclusion of the sea state

3   WAGES

3.1   Overview

The Waves, Aerosol, and Gas Exchange Study (WAGES) is a UK Natural Environment Research Council funded project co-managed by the National Oceanography Centre (NOC), Southampton and the University of Leeds. Near-continuous measurements of the air-sea fluxes of CO_2, aerosol, heat, moisture and momentum were made from June 2010 until August 2013. Supporting measurements were made of meteorological conditions, the sea state, and of wave breaking. WAGES directly followed on from the High Wind Air-Sea Exchange (HiWASE) study (Prytherch et al., 2010b) and SEA-Spray gas flux And Whitecaps (SEASAW) project (Norris et al. 2012, 2013a,b); both projects were part of the UK's contribution to the Surface Ocean Lower Atmosphere Study (Brooks et al. 2009a,b). The period from June 2010 until April 2012 is discussed in this work. My own work includes all processing and analysis using the raw instrument outputs.

3.1.1   Transition from HiWASE to WAGES

HiWASE collected open ocean flux measurements for three years (September 2006 until December 2009) from the Norwegian weather ship *MS Polarfront*, which was stationed near-continuously at 'Station Mike' (66°N 3°E), with around three days per month when the ship was in port or transit. WAGES was originally designed to continue from the long term measurements of HiWASE on the *Polarfront*, with additional aerosol flux instrumentation from SEASAW installed. Unfortunately, in 2009 the Norwegian Meteorological Institute withdrew funding for the *Polarfront* and the ship was withdrawn from service that December, three months after the formal start date of WAGES. A replacement vessel was sought that routinely operates in high wind and sea conditions, and has well exposed sites at which meteorological sensors could be installed. The *RRS James Clark Ross* (JCR; Figure 3.1) was chosen, a vessel run by the British Antarctic Survey. It operates in the Southern Ocean for most of the year, returning to the UK for refit and a brief northern hemisphere season, typically from June until September.

Figure 3.1 – The *RRS James Clark Ross*, image courtesy of Ben Moat.

This work examines the flux measurements that were made on the JCR whilst the ship conducted its routine activities. There were 5 manned Intensive Observation Periods (IOPs) during the period covered in this thesis, each of a few weeks in duration. During IOPs, maintenance of instrumentation was carried out, a number of additional measurements were taken, and some dedicated days per cruise were allocated, during which WAGES had control of ship science activities. Dedicated WAGES hours were often taken in an opportunistic way, to fit around the cruise plan of other scientific parties with which ship time was shared. During dedicated WAGES time the ship was usually oriented so that the average wind direction was onto the bow, which improves the quality of flux measurements because the flux sensors were on the foremast. Dedicated time was therefore mostly taken during high wind speed events, to maximise the volume of best-quality high wind speed measurements in accordance with WAGES objectives. Two additional activities were also undertaken during IOPs; the first was the deployment of a spar buoy that measured the wave spectrum and counted wave breaking events (similar to that detailed by Pascal et al., 2011). The second was the deployment of

a balloon mounted aerial camera that acquired sea surface photographs, which were later processed to yield whitecap fraction estimates using the method of Callaghan and White (2009). Many of the regular activities of the JCR, such as mooring deployments or CTD casts, required the ship to hold position. This fact was exploited to yield many more measurements with bow-on winds, by leaving a standing request with the officers to face the ship into the wind, if doing so was safe and convenient.

The transfer of operations away from the *Polarfront* was not ideal, but using the JCR was considered to be the best available way to continue the project. One great advantage of the *Polarfront* was that the ship almost constantly held position, and was oriented so that flux sensors were well exposed to the wind, which meant the fraction of usable data was higher from HiWASE than from WAGES. Around 5500 useful hours of flux data were available from two years of HiWASE (pers. comm. John Prytherch) as opposed to around 1800 hours found using the same quality control criteria for two years of WAGES. An additional loss was the ship borne wave recorder, measurements from which could be used to compute the significant wave height.

3.2   Instrumentation

Whilst the full instrument list is provided for completeness here, only a select group of measurements are relevant to this thesis. This includes: all the Autoflux sensors with the exception of CLASP; the wheelhouse top meteorological sensors; the Rotronic meteorological sensors; the sea surface temperature (SST) measurements; and the navigational data

3.2.1   Flux instrumentation

The "Autoflux" flux measurement and logging system (Yelland et al., 2009) was used during WAGES. It was specifically designed for long term autonomous deployment. At the start of every hour, Autoflux began acquiring outputs from a suite of instruments sampling at 20Hz, mounted on the foremast (Figure 3.2). Two-way communication between Autoflux and NOC Southampton was set up via an Iridium satellite link. Diagnostics, and inertial dissipation fluxes, could

thus be checked remotely, and commands such as system reboots could be sent without the need for a ship visit. Faults could be detected early so maintenance was more efficiently planned, and data losses caused by system crashes were minimised. Ship visits were carried out several times a year to perform maintenance, retrieve data, and clear local data storage space.

The suite of sensors logged by Autoflux consisted of a Gill Solent R3A 3-axis sonic anemometer, a Systron Donner MotionPak 3-axis motion sensor, two Licor Biosciences Li-7500 open path infra-red H_2O/CO_2 gas analysers, and a Compact Lightweight Aerosol Spectral Probe (CLASP; Hill et al., 2008). A major mid-campaign instrument change was made in November 2011 when one of the Li-7500s was replaced with an improved model, the Li-7200. The new sensor was better suited for marine use (the design based on the innovative method of Miller et al., 2010) but experienced many technical faults over the dates relevant to this thesis, so the Li-7200 measurements are not discussed in this thesis.

The Sonic Anemometer samples the wind vector and the so-called sonic temperature at 100 Hz. Wind components are computed from the difference in the forward and backward travel times of a sound wave between each of three pairs of transducers; air advection alone causes the difference. The 'sonic' temperature (closely related to the virtual temperature) is calculated from the absolute travel times of the sound wave between the transducer pairs, taking advantage of the fact that the absolute speed of sound is a function of air density, which in turn is a function of virtual temperature (Kaimal and Gaynor, 1991). Block averaging is used to reduce the sonic anemometer output frequency from 100 Hz to 20 Hz, the latter being the maximum sampling rate of the Li-7500.

The motion pack measures three orthogonal rotation rates and accelerations, required to provide high frequency corrections to the wind vector for ship motion and attitude. The motion pack outputs were connected to the sonic anemometer auxiliary inputs in order to synchronise the two instruments.

Figure 3.2 – Foremast platform of the JCR, viewed from the bridge, showing flux instrumentation on the starboard side. Image courtesy of Ben Moat.

The Li-7500 samples H_2O and CO_2 densities within a volume open to largely unrestricted air flow (an open path as opposed to a closed path sensor). The Li-7500 measures the extinction of light beams of several frequencies (split by a chopper wheel with alternating filters) as they travel through the sensing volume. Two narrow band frequencies (2.59 μm and 4.26 μm) coincide with the molecular absorption bands of water vapour and CO_2, so extinction is directly proportional to the density of those gases. Comparison of both with the extinction of a 'null absorption' reference beam at 3.95 μm allows the extinction from molecular absorption by H_2O and CO_2 to be isolated, so the gas densities can be calculated. The Li-7500 output series were synchronised with the anemometer and motion pack during post-cruise processing by use of an externally generated square wave signal, input into both the Li-7500 and sonic anemometer auxiliary inputs. Two Li-7500s were used, so as to enable assessment of motion-induced measurement bias in the CO_2 density (Yelland et. al., 2009). One Li-7500 is shrouded to provide a control measurement from which motion bias is quantified to yield a correction. Whilst CO_2 densities are not examined here due to poor signal to noise

levels of the CO_2 flux, times when Li-7500s are shrouded must be excluded from analysis of scalar fluxes. Washers were also installed to address an issue regarding sea spray contamination of the Li-7500 optics; the CO_2 density measurements can be biased by contamination of optics by hygroscopic particles (Prytherch et al., 2010a), but H_2O densities are negligibly affected.

CLASP takes size segregated aerosol concentrations samples at 10Hz, high enough to be used in turbulent flux calculations. This thesis does not examine CLASP measurements, so the instrument is not discussed further.
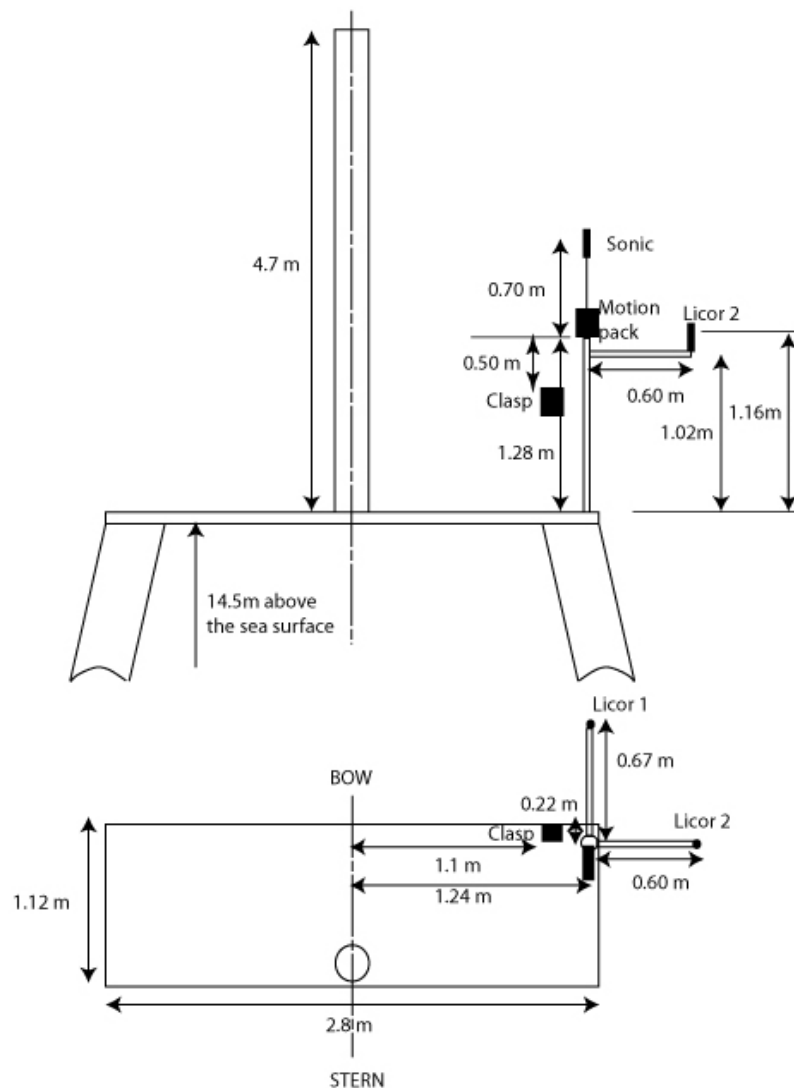
Figure 3.3 – Schematic of Autoflux sensors on the foremast platform of the JCR, courtesy of Ben Moat.

To interpret flux measurements, precise knowledge of the sensor positions and orientations is essential, relative to one another and to the ship itself (Figure 3.3). The Foremast Platform deck, above which the sensors are installed, is 14.5 m above mean sea level for a typical draught of 5.6 m. The anemometer sensing region is 1.9 m above the platform deck, so the anemometer height is on average 16.4 m above sea level. The anemometer was physically fixed to the same mounting plate as the motion pack, with negligible horizontal offsets and a 0.7 m vertical offset between the anemometer sensing area and the bottom of the motion pack. Several different pairs of anemometer and motion pack installations were used over the 18 month study period. The fore and starboard Li-7500s were 0.67 m and 0.6 m respectively offset horizontally from the motion pack, and had a sensing height of 1.16 m above the deck.

3.2.2 Meteorology and sea state sensors

An NOC-built aspirated psychrometer and a Vaisala Temperature and Humidity sensor (model HMP45A until 23rd June 2011, when replaced with model HMP155) were installed on the wheelhouse top, port side, to measure meteorological conditions (Figure 3.4). The height above mean sea level of the Psychrometer and Vaisala were 18.7m and 18.5m respectively. An Eppley Precision Infrared Pyrgyometer measured down-welling infrared (3.5 to 50 µm wavelength) and a Kipp and Zonen CM11 sensor measured down-welling solar (310-2800nm wavelength). The wheelhouse top measurements were sampled every 10 seconds.

The ship had a number of sensors that were used but not installed specifically for WAGES. Bulk upper ocean temperature was measured at the inlet to the non-toxic water supply, sampled at 6m depth, using a PRT 100 Platinum Resistance Temperature sensor. A Seabird SBE45 microTSG Thermosalinograph provided salinity measurements. Water properties were sampled at 5 s intervals. Meteorological instruments were used to provide back up when equivalent WAGES sensors failed. Two pressure sensors (Vaisala PTB201B1A2B) were installed in the Underway Instrument and Control room at 8 m above sea level. There were two Rotronic MP103A temperature and humidity sensors, although one completely failed throughout WAGES, also on the foremast but significantly

above the WAGES flux sensors, at a height of 20.4m above sea level. On 21st July 2011 both sensors were replaced with HC2-S3 Rotronic sensors. The Rotronics were required as replacements for the Psychrometer and Vaisala for significant periods. Radiative fluxes were measured by a Kipp and Zonen SP lite, and a Kipp and Zonen PAR lite. The ship's meteorological instruments were all sampled every 5 seconds. A Gill 'Windmaster' sonic anemometer measured relative wind speed and direction, sampling every 2 seconds; note that any reference to the 'anemometer' is to the Gill R3A.

Figure 3.4 – Meteorological sensors on the wheelhouse top. Image courtesy of Ben Moat.

Navigational data was sampled at 1Hz by a Kongsberg Seapath 200 Heading, Attitude and Positioning sensor; these data were required in addition to the MotionPak outputs in the motion correction procedure. In September 2010, a MIROS 'WAVEX' X-band scanner was installed; it sampled for 2 of every 5 minutes, and calculated two dimensional wave spectra and parameters such as the significant wave height and zero crossing period. Seawater CO_2 concentration were measured by Plymouth Marine Laboratory using the method of Cooper et al. (1998). Photographs of the sea surface were taken autonomously from the bridge

port side, at a range of different samplings rates throughout WAGES and used to obtain whitecap fraction estimates using the method of Callaghan and White (2009).

3.2.3 Data Logging

Full details of data logging, communications, and powering are given by Moat et al. (2010), and a summary provided here. Autoflux sensors output to a four port Digi PortServer (Model: TS 4 W MEI), via four separate serial connections. The four ports were connected to: the R3A sonic (RS485); each of the two Li-7500s (RS232); and CLASP (RS232). Data were transmitted by the PortServer via a wireless Ethernet connection to an Access Point/Bridge (MiLAN W2331GUS) installed below the wheelhouse top. A direct Ethernet link from the Access Point/ Bridge to the ship's local network allowed a SUN Fire V210 system to interface with the 4 serial connections to Autoflux sensors as if there was a direct connection, by use of Realcom software. The SUN Fire station had separate programs running that acquired the four Autoflux data streams for 58.3 minutes from the start of every hour. During the remaining 1.6 minutes of the hour, the acquisition programs calculated turbulent spectra, before saving each time series record (70'000 20 Hz samples in length) in binary (Sonic Anemometer and MotionPak) and ASCII (Li-7500s) formats. During the subsequent hour (whilst Autoflux data were continually received), additional parameters (diagnostics, the inertial dissipation fluxes and some turbulence statistics) were calculated and saved in separate ASCII files. These calculations were performed on records split into sections 1024 samples long; the length is a historical legacy because it is less computationally expensive to perform Fast Fourier Transforms on series of lengths that are a power of 2, although this is no longer a relevant factor given modern computing power. No time variable is appended to the 20Hz data, but the SUN Fire station clock is synchronised to the clock of the GPS, allowing the flux instrument series to be time matched to data from non-turbulent instruments.

The meteorological sensors on the wheelhouse top communicated directly via Ethernet connection to the SUN Fire station through a second Digi PortServer. Software logged and saved hourly ASCII streams, appending the SUN Fire system time (matched to GPS time) to each sample. Use of separate acquisition

programs for each data stream removed the vulnerability of the system to one stream failing. To further improve autonomy, monitoring software was installed that restarted failed programs.

Data streams from the GPS, Rotronics, Windmaster anemometer and the water temperature and salinity were available on the ship's network. These were acquired and saved by the SUN Fire station in hourly ASCII files: The SUN Fire station appends the GPS time to all data from the ship's network (except the navigational data which already had the correct GPS time stamp) so that each value in the hourly records has a common reference time. The time stamp on the streams directly taken from the ship's network suffered from drift and so it was necessary to substitute in the GPS time.

Uninterruptible Power Supply (UPS) units supplied DC power to the Autoflux instruments via the ship's internal wiring. UPS were used to ensure that in the event of a temporary power loss a clean power down and restart could be done. Supply to the sonic anemometer, the Li-7500s, and CLASP was 24 V from one UPS. Another UPS supplied the MotionPak (±15 V), the foremast platform Digi PortServer (12 V), and the Li-7500 washer pumps (12 V). A third UPS powered the Iridium modem (12 V), the Digi PortServer (12 V) below the wheelhouse top deck, the wheelhouse top meteorology sensors (12 V for the psychrometer fan and 24 V for the psychrometer and Vaisala).

3.3 Post-cruise processing

My own analysis work began using the full archive of raw hourly data records, prior to any quality control or post-cruise processing. Therefore many records in the archive were from times when the ship was in port, and from times when instruments failed. This section describes the sequence of data processing applied to all raw hourly files in order to obtain the following: half hour long turbulence records with ship motion effects removed; half hour true temperature and humidity series from the flux instrumentation; and average meteorological parameters over each half hour. The same procedure was applied equally to all records where possible, including, say, data from port calls. Quality control was carried out after processing was complete when producing each figure or result

presented in this thesis. All processing was carried out in Matlab using bespoke code written either by myself or credited where appropriate.

3.3.1 Conversion into Matlab compatible files

During conversion of the raw data streams into hour long Matlab arrays, several distinct technical issues arose, although final results were not affected. During this processing step, units of all variables were converted to SI standards.

There were two specific periods when a loss of power followed by a restart caused the serial protocol that the Digi PortServer was programmed to expect to return to the default of RS232; this is incompatible with the output of the anemometer. The dates in question were 16th Feb – 18th March 2010, and 10th Oct – 24th Nov 2011, inclusive. The effect of the protocol change on the binary output was that single bytes of value 162 (pers. comm. Robin Pascal) were added (an addition, not a replacement) to binary messages at seemingly random positions; throughout the whole hourly record. This meant that the rogue byte shifted the rest of the bytes down the message, so the real data was not in the expected position in the message. This meant that the extracted Matlab files had series with a significant fraction of corrupt values. However, these periods covered more than two whole months of useful ocean measurements, so it was worth the effort to recover the files. The problem was resolved by using the checksum value output by the anemometer at the end of each binary message. The checksum byte was located just before the two bytes that were 'start of line' markers of the subsequent message. A reference checksum was manually calculated for each message and compared to the checksum output by the anemometer; if there was not a match, then that message had individual bytes with a value of 162 removed. This removed more than 99% of corruptions.

A second problem was concurrent with the February to March 2010 incident above. Presumably during Feb 16th 2010 power cycle incident, a resistor in the Sonic Interface Unit (which provides the synchronisation square wave) blew, which resulted in the frequency of the sync signal as seen by the sonic being altered very slightly. Synchronisation was still possible because the drift was negligible over a few square wave cycles.

A persistent issue affected the conversion of all ASCII streams to Matlab variables; a wide variety of corruptions in each ASCII streams arose from time to time. Sometimes single lines were corrupted in an otherwise good record; sometimes the corruption was over many months but only affected a single comma-separated value in each line; either way data was recoverable. Bespoke extraction codes were developed to rather laboriously check every individual line, and even the contents of every delimiter pair for unexpected values.

3.3.2 Spike removal

The raw time series of the flux instruments had suspect individual values, or 'spikes' that needed to be accounted for. A first pass simply identified extreme single values that were well out of a generous realistic range; extreme outliers can heavily influence statistics. A second pass used a running window of length 30 seconds and moved in 15 second intervals to create a series of windows covering the whole series. Within each window, the standard deviation was calculated using the middle 98% of ranked data points within the window; ranking and removing the outermost 2% prevented spikes from distorting statistics in the window whilst not noticeably influencing the standard deviation. Data points which lay 3.5 standard deviations above or below the mean were identified as spikes and replaced, unless there were 10 or more concurrent points. 10 points or less (half a second) was chosen to be acceptable for spike replacement because it was found that suspect data periods were usually either 'long' (many more than 10 suspect points and not acceptable for spike replacement) or 'short' (only several points so acceptable for spike replacement).

To replace spikes, the corresponding value from a 21-point running median filtered series was substituted. 21 points ensure that replacement values for suspect periods up to 10 data points in length were derived using values unaffected by spikes.

The Li-7500 H_2O density output was not suitable for the first pass because there were many hourly series that had reasonable perturbations but with a suspect mean offset which could yield unrealistic, even negative, densities. The Li-7500s were periodically calibrated to avoid this, although it was suggested (Ian Brooks, pers. comm.) that the cause may be saturation of the internal CO_2 and H_2O

scrubbing chemicals. Mean values of specific or relative humidifies were therefore not reliable from either Li-7500.

Spike removal was less important for the low rate meteorological data, because only the half hour mean of these data were used. A 7 point running mean was used with two passes (extreme values and 3.5 standard deviations).

3.3.3 Synchronisation of flux sensors

The motion pack outputs were sampled by the sonic anemometer auxiliary inputs, and so no additional synchronisation is required; this is not the case for the Li-7500s. The different serial ports were opened by the SUN Fire unit sequentially, leading to a time delay between the start of acquisition of the anemometer stream, and each the Li-7500 streams. The time delays were generally found to be around 1 s but the daily average could be up to 5 s for some periods. Over the data set, the average delay between the acquisitions of the Li-7500 #1 stream after the anemometer had started was 1.1 seconds; 2.1 seconds for Li-7500 #2. Standard deviations of delays were 0.25 s, highlighting the need to perform a lag correction tailored for each hour rather than an average correction.

To correct for the delay, an externally generated square wave signal (period of approximately 10 s) was input into the anemometer and each Li-7500. Artificial lags were imposed by removing the first *1, 2, 3...200* values from the anemometer square wave series, and last *1, 2, 3...200* values from the Li-7500 square wave series. For each artificial lag the covariance between each square wave series was calculated. The artificial lag that resulted in the maximum covariance was the best lag estimate, correct to within 1/40 s. The number of values corresponding to the lag was removed from the start of each of the anemometer/ motion pack series, and from the end each of the Li-7500 series. The first samples were time stamped as precisely on the hour, with each subsequent timestamp increased by 1/20 s. Note that the first samples, time-stamped as the start of the hour, were actually sampled some short time after; this is addressed during motion correction when time-matching the navigational data.

3.3.4 Motion Correction

Wind measurements taken from a fixed sensor on a moving platform are directly contaminated by the motion of the platform. The ship typically experienced wave-induced motion with periods of around 5 to 25 s. The anemometer had many degrees of freedoms with which to move in and rotate about, which could each affect any of the three measured wind vector components. There were also the ship's horizontal mean motion, and high frequency modes of motion induced by vibration. A motion correction strategy must account for motions across the whole frequency range. The method of Edson et al. (1998) was adopted here, using corrections from the motion pack and the GPS. The objective was to compute a motion-corrected wind vector in a true earth frame of reference (north, east, and up), as if measured from a stationary flux tower on a flat plain with an anemometer perfectly aligned with the horizontal in a right handed system, with the x axis pointing east, the y axis pointing north, and the z axis pointing up. Matlab scripts were adapted from those developed by Ian Brooks on the SEASAW project (Brooks, 2008).

The motion pack and anemometer were installed (Figure 3.5) on the same mounting plate, which ensures that the raw outputs are in almost exactly the same horizontal plane. The motion pack is aligned as best possible to point down the centreline of the ship; the group installing the sensor communicate with a relatively distant observer at the centre of the bridge who is better placed to judge. The anemometer was fixed to the plate using an anticlockwise rotation until locked into place. This meant that the anemometer had a yaw offset of about 8 degrees to port from the motion pack.
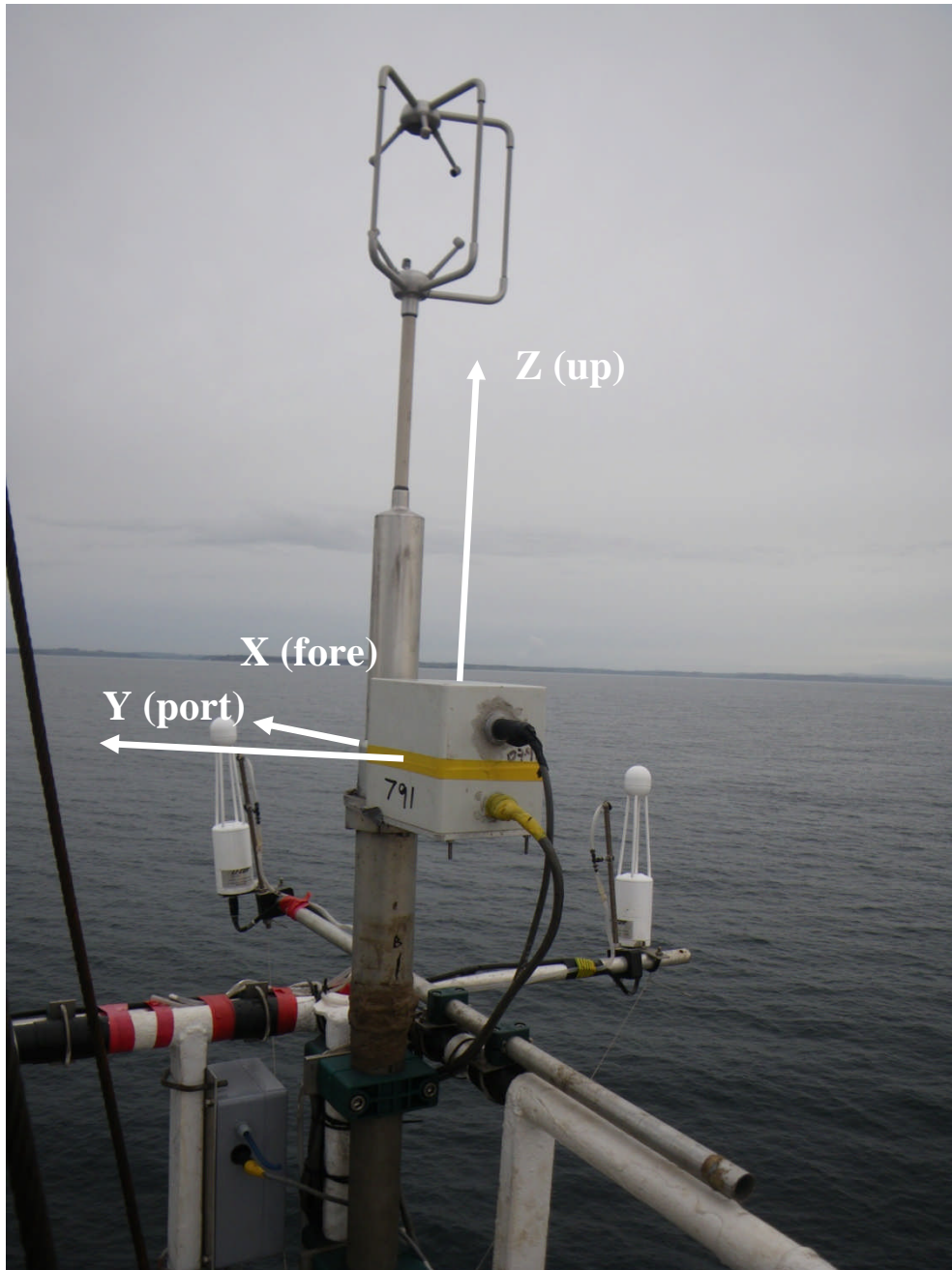
Figure 3.5 – Autoflux from the foremast platform, photographed facing between fore and starboard. The motion pack is the central grey box, aligned facing to fore. The anemometer is directly above; all three spars are toward aft. The anemometer is aligned approximately 8 degrees to port from centreline – defining its alignment direction as the vector from the middle spar to the central strut. Photograph courtesy of Margaret Yelland.

Figure 3.5 also illustrates the frames of reference of the raw motion pack outputs. The motion pack outputs an orthogonal set of accelerations and rotation rates. The raw motion pack output sign conventions are adjusted by analogue filters and then by Matlab extraction code to ensure that the coordinates of the outputs

define an orthogonal right handed system very close to that to that used by the anemometer. Accelerations ($m^2\,s^{-2}$) are defined as a_x, a_y and a_z: positive to fore; positive to port; and positive upward respectively. Rotation rates R_x, R_y and R_z are positive for a clockwise rotation about each positive x, y and z directions; i.e.: positive port up, bow down, and bow to port respectively.

The anemometer outputs 3 orthogonal wind components, in $m\,s^{-1}$, according to the sign convention UVW (not U'V'W') used in Figure 3.6; subscript 'R' indicates the raw measurement frame of reference. u_R is positive from the middle spar to the central strut (nominally aft to fore), with an additional 30 degrees rotation to anticlockwise to port; v_R is positive 90 degrees to anticlockwise of u_R (so is nominally starboard to port with an additional 30 degree rotation toward aft); w_R is positive up the central strut (nominally upwards). u_R, v_R and w_R therefore define a right handed system that is similar to x, y, and z, but rotated by 30 + 8 degrees anticlockwise when viewed from above. There are also small differences in the tilt from the absolute horizontal between the two sensors.
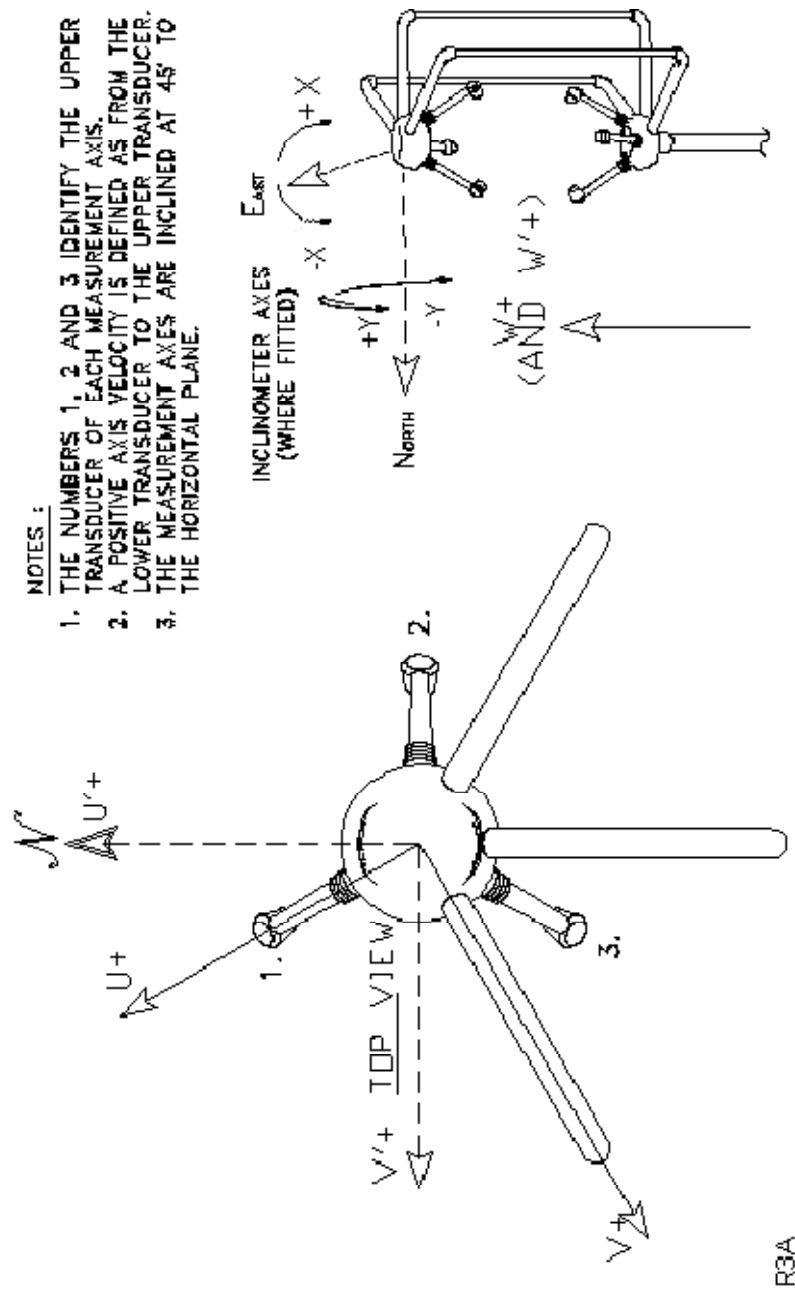
Figure 3.6 – Extracted from the Gill R3A 3-axis sonic anemometer user manual (page 44). The output frame of reference during WAGES is UVW, not U'V'W'. In the figure, U' nominally points towards the bow and V' to port.

The anemometer wind components were then transformed into the frame of reference of the motion pack. Three consecutive rotations were applied using a transformation matrix **M** that incorporates each consecutive rotation, noting that the ordering of rotations affects the outcome. The specific ordering is consistent with Edson et al. (1998) and Brooks (2008).

$$U_{FINAL} = M.U_{INITIAL} \tag{3.1}$$

$$U = \begin{bmatrix} u \\ v \\ w \end{bmatrix} \tag{3.2}$$

where **U** is the wind vector, and the subscripts refer to the frame of reference. **M = Y. P. R** where each of the right hand terms defines a transformation matrix that rotates the reference frame by each single angle of yaw (*Y*), then pitch (*P*), and then roll (*R*):

$$Y = \begin{bmatrix} cos\,(Y) & -sin(Y) & 0 \\ sin(Y) & cos(Y) & 0 \\ 0 & 0 & 1 \end{bmatrix} \tag{3.3}$$

$$P = \begin{bmatrix} cos\,(P) & 0 & -sin(P) \\ 0 & 1 & 0 \\ sin\,(P) & 0 & cos(P) \end{bmatrix} \tag{3.4}$$

$$R = \begin{bmatrix} 1 & 0 & 0 \\ 0 & cos(R) & -sin(R) \\ 0 & sin(R) & cos(R) \end{bmatrix} \tag{3.5}$$

P is positive for an upward rotation the x-axis (bow up), *R* is positive for an upward rotation of the y-axis (port up), and *Y* is positive for an anticlockwise rotation of thee x-axis toward the y-axis (bow to port), note that this is not a true right handed coordinate system. The pitch, roll and yaw offsets between the anemometer and the motion pack were derived from laboratory tests post-deployment. There were 5 combinations of motion packs and anemometers during the investigation period, and all had similar offsets: Pitch and roll offsets ranged from 0.49 to -0.61 degrees with typical uncertainties in the offset of each combination of ±0.05 degrees. Yaw offsets ranged from -7.2 to -8.2 degrees with uncertainties of ±0.2 degrees. Brooks (2008) investigated misalignments between the anemometer and motion pack by applying artificial misalignments to data from the *RRS Discovery*. A pitch misalignment of 1 degree led to a 1.8% mean

bias in momentum fluxes; a roll misalignment of 1 degree caused a RMS error of 3.8%.; a yaw misalignment of 1 degree had a negligible effect. The uncertainties quoted in the laboratory results are therefore adequate for purpose.

There are three corrections that need to be made to the wind vector in order to transform it from the motion pack frame to a true earth frame of reference. The first corrects misalignments of the anemometer with respect to the earth; without this step, when the anemometer pitches upward, the measured vertical wind will have contamination from the horizontal wind. The second correction, applied after misalignment correction, deducts the translational velocities of the anemometer with respect to the earth from the wind vector. Velocities and alignments are equal for both the motion pack, and the wind vector in the motion pack frame of reference. The third correction is required to remove the translational velocities of the anemometer induced by rotation about the motion pack; this is a relatively minor (cm s^{-1} scales when the total motions are m s^{-1} scales) correction compared to the other two, because during WAGES the anemometer and motion pack are adjacent.

Time series of translational velocities and alignments are needed, which requires single integrations of the motion pack accelerations, and of the rotation rates, respectively. Series integrated from the raw motion pack data have temporal drift caused by accumulations of adding small systematic errors in raw measurements. To address this, a high pass filter was applied to the accelerations and rotation rates prior to integration. The filter transfer function had a cosine transition between 0.016 Hz 0.0083 Hz (1 and 2 minute periods respectively), so wave-induced motions were not removed by filtering because they are at higher frequencies. After filtering, the starts and ends of all motion and wind series were truncated, in order to remove ringing effects.

High pass filtering removes the mean tilts with respect to the earth, and lower frequency velocities; they need to be reintroduced after integration. The mean tilts are computed from low pass filtered acceleration series. The low pass filtered series were derived by deducting the high pass filtered series from the raw series. Low frequency pitch and roll series were computed from the low frequency a_x and a_y series; any non-zero value *must* be gravitationally induced, and a simple

trigonometric calculation with the gravitational acceleration vector yields the low frequency pitch and roll angles with respect to the true horizontal.

Low frequency yaw, and x and y velocities, were computed from the low pass filtered heading, course-over-ground, speed-over-ground measurements from the ship's navigation data. The low frequency z velocity is of course zero. To synchronise the GPS series with the motion pack, a correlation analysis similar to that outlined in section 3.2.3 (synchronisation of the Li-7500 and anemometer) was carried out. R_z from the motion pack, and the rate of change of heading from the GPS (interpolated to a 20 Hz time base), were used to calculate the offset.

The matrix transformations required to correct the wind vector from the motion pack frame of reference to the true earth frame are given by Edson et al. (1998), and not repeated here. Their application results in a wind vector series that has been corrected for ship motion, and is in the true earth frame of reference. The time series of the three orthogonal earth frame wind components, after motion correction, are defined (all in m s^{-1}) as u_E, v_E, and w_E: positive to the east, to the north, and upward, respectively.

3.3.5   Rotation into the streamline frame of reference

The ship induces an upward tilt to the mean air flow; this is accounted for by using well-established methods appropriate for analysing wind flow over a slope, where a similar tilt of the mean flow from the horizontal is observed. The double rotation method (e.g. Aubinet et. al., 2010) is commonly used to transform the earth-frame wind components into a streamline frame of reference.

The two mean horizontal components are used to define the first rotation, in the horizontal plane

$$\theta = tan^{-1}\left(\frac{\overline{v_E}}{\overline{u_E}}\right) \tag{3.6}$$

$$u_H = u_E.\cos(\theta) + v_E.\sin(\theta) \tag{3.7}$$

$$v_H = -u_E.\sin(\theta) + v_E.\cos(\theta) \tag{3.8}$$

where θ is the angle (radians) between the mean true east and mean streamline wind directions, positive anticlockwise. u_H and v_H are the streamline and cross-stream wind components, positive in the wind direction, and at 90 degrees anti-

clockwise, respectively. The subscript '*H*' indicates horizontal streamline coordinates (to be distinguished from tilted streamline coordinates). The mean of u_H is the mean horizontal wind speed, and the mean of v_H is zero.

At this point an additional correction (pers. comm. Margaret Yelland) is made to w_E, to account for the translational velocity of the ship. When the ship is not underway, w_E has some aliased component from u_H, caused by an upward tilt of the mean flow caused by the superstructure of the ship. It is a standard correction to remove this. However, if the ship *is* underway – the typical JCR speed over ground when underway was 7 m s^{-1} – then an *additional* component is aliased into w_E from the motion-induced component of the relative wind. This is shown in Figure 3.7; w_E as output by the motion correction procedure has a component ($\Delta \overline{w}$) induced by steaming. This was be deducted to find the true vertical wind series $\overline{w_{TRU}}$, that is then used with $\overline{u_{TRU}}$ to define a mean upward tilt angle of the flow. A deduction of a single mean value to w_E is desired; there should be no differences between w_E' and w_{TRU}', because only the effects of *mean* horizontal ship motion are removed.
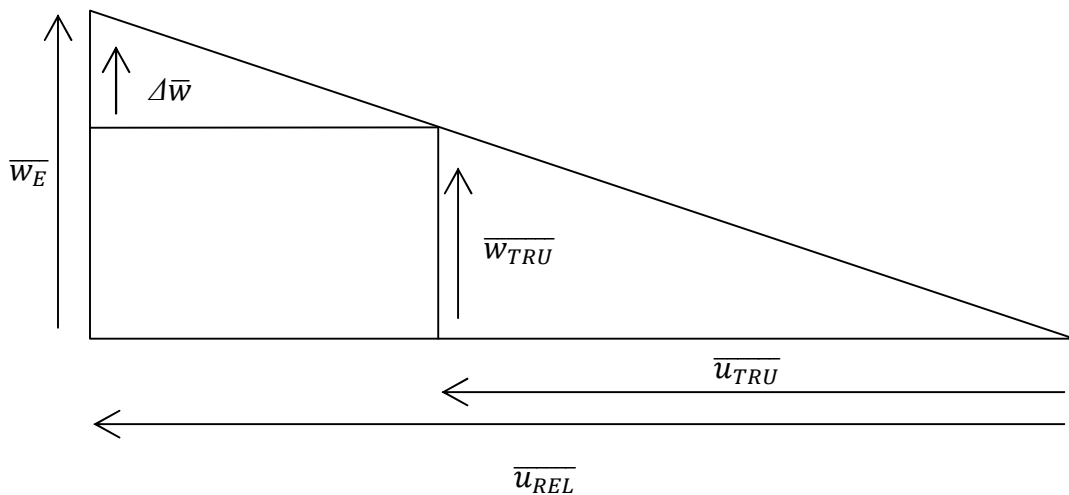
Figure 3.7 - Influence of mean horizontal ship motion on the measured vertical wind. Adapted from a sketch by John Prytherch.

The algebra is relatively simple: β defines the ratio of the true and relative mean wind components; equal for both *u* and *w*.

$$\beta = \frac{\overline{u_{TRU}}}{\overline{u_{REL}}} = \frac{\overline{w_{TRU}}}{\overline{w_E}} \qquad (3.9)$$

Δw is then expressed in terms of known means:

$$\Delta \overline{w} = \overline{w_E} - \overline{w_{TRU}} \qquad (3.10)$$

$$\Delta \overline{w} = \overline{w_E} - \overline{w_E} . \beta \qquad (3.11)$$

Then w_{TRU} is simply the difference between w_E and Δw, ensuring that the perturbation is separated:

$$w_{TRU} = \overline{w_{TRU}} + w \qquad (3.12)$$

$$w_{TRU} = w_E - \Delta \overline{w} \qquad (3.13)$$

$$w_{TRU} = w_E - [\overline{w_E}(1 - \beta)] \qquad (3.14)$$

To keep subscripts consistent with the horizontal streamline frame of reference, after this correction, w_{TRU} is referred to hereafter as w_H.

The second standard rotation was then made; it is in the plane of the horizontal streamline and the true vertical directions, and rotates the horizontal streamline wind components into tilted streamline wind coordinates:

$$\gamma = tan^{-1}\left(\frac{\overline{w_H}}{\overline{u_H}}\right) \qquad (3.15)$$

$$u_S = u_H . \cos(\gamma) + w_H . \sin(\gamma) \qquad (3.16)$$

$$w_S = -u_H \sin(\gamma) + w_H . \cos(\gamma) \qquad (3.17)$$

where γ is the angle (radians) between the mean horizontal streamline and mean tilted streamline wind components; positive upward from the horizontal plane. Subscript 'S' indicates streamline coordinates.

A brief validation of the Yelland correction was carried out (Figure 3.8). It is not suitable at this point to discuss the detailed corrections and quality controls that make up a large part of subsequent chapters of this thesis; these are discussed logically in due course. To ensure a sensible comparison, roughly 1000 records that passed all data quality controls and had corrections applied were used. The mean EC fluxes with the Yelland correction applied agreed with the results of a

bulk algorithm (COARE 3.0; Fairall et al. 2003) to within a few per cent, with a standard deviation of individual differences of 20%. The level of agreement was not affected by splitting the records into those when the ship was steaming ahead or holding position. However if the Yelland correction was not applied, there was disagreement between the COARE 3.0 and EC fluxes, that was a strong function of the ship's velocity. The results agreed within a few per cent when the ship was holding position, but were biased – EC results were about 25% higher than COARE 3.0 results - when the ship was steaming.
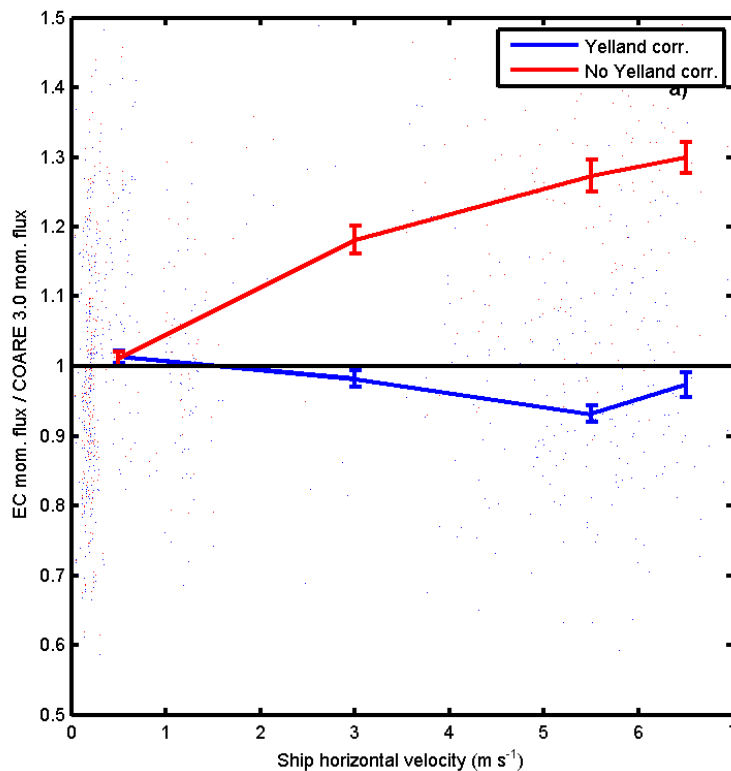
Figure 3.8 – Effect of the Yelland correction on the ratio of the average eddy covariance momentum fluxes and those from COARE 3.0.

3.3.6 Choice of time series length

Selecting a time averaging period is a compromise between two competing constraints. Long sampling periods risk a change of turbulent statistics and/or mean atmospheric conditions over the record; for example from mesoscale fluctuations or frontal passages. Short sampling periods may not adequately

sample the largest turbulent motions. The low frequency part of the cumulative integral of the flux cospectrum - the ogive function (Figure 3.9) - can be examined for unexpectedly large low frequency signals (a symptom of non-stationarity) or lack of convergence (a sign that the sampling period was too short). Using a 30 minute series length, it was found that almost all momentum flux ogives had converged at the low frequency limit. 30 minutes is well within the range of periods chosen for air-sea EC studies: Miller et al. (2010) used 13.7 minutes; Prytherch et. al. (2010b) used 20 minutes; Smith (1980) used "about" 40 minutes; Huebert et. al. (2010) used 40 minutes.
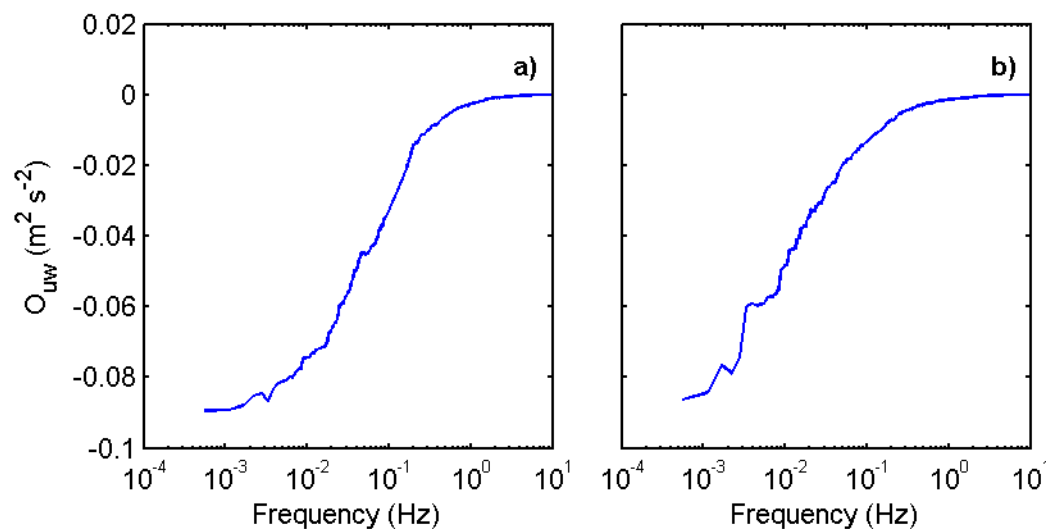
Figure 3.9 – Example of a) an ogive of the momentum flux that shows convergence toward low frequencies; b) an ogive that does not converge. The flux estimate from record b) is therefore less reliable than from a).

Even if all systematic biases are known and corrected for, variability between individual flux estimates persists from random variability of the turbulence. At a fixed point one cannot precisely repeat a measurement, so instead must assume stationary and horizontally homogenous statistics, which will inevitably have a degree of error (particularly of poorly sampled eddies with low frequencies; Finkelstein and Sims, 2001). Fairall et al. (2000) give a statistical sampling uncertainty of order 20% for 1 hr flux measurements, although this is stated to be highly dependent on conditions. Lee et al. (2004) state that the different choices

of time series trend removal, rotation methods, and sample averaging times can affect the covariance by up to 10-25% in total. These numbers give some idea of the expected variability between flux estimates even when conditions are stationary and measurements ideal.

At this point a set of half hour records of motion-corrected streamline wind vectors have been defined. However, the development of a flux parameterisation requires more data, such as the average 10 m wind speed and atmospheric stability per record. The processing of half-hourly mean parameters is now discussed.

3.3.7 Mean temperature and relative humidity

Mean values of sonic air temperature and relative humidity derived from the anemometer and Li-7500 were found to be biased significantly (several degrees C, tens of per cent humidity) from the other meteorological sensors, and so were unsuitable for the calculation of average conditions. Only Rotronic #2 was available up until the July 2011 refit, when both #1 and #2 were replaced (for clarity, the replacements named here as #1 and #2). Rotronic #1 was never required due to complete coverage from Rotronic #2. There were therefore three instruments available for measurements of true air temperature and relative humidity; the psychrometer, the Vaisala, and Rotronic #2 (hereafter named the Rotronic). The psychrometer and Vaisala were regularly calibrated and checked during ship visits, whereas the Rotronic was not. The Vaisala suffered from many periods of failure, and so the Psychrometer was chosen to be the primary measurement of temperature and relative humidity. However, the other two sensors were often required as backups, so offsets were calculated and corrections applied when a substitute to the Psychrometer was needed.

Figure 3.10 shows that the Vaisala had a humidity dependent temperature offset from the psychrometer. The humidity dependence is not well-defined, making the Vaisala a poor secondary temperature reading, so it was never used. The Rotronic temperature offset from the psychrometer had more scatter than the Vaisala, but no obvious humidity dependence. The change in the offset corresponds to the date when the Rotronic was replaced. The offsets used when the Rotronic temperature was required are shown by the two clear peaks in Figure 3.10.f; the

Psychrometer was higher by 0.82˚C prior to July 2011, and lower by 0.11˚C after sensor replacement.
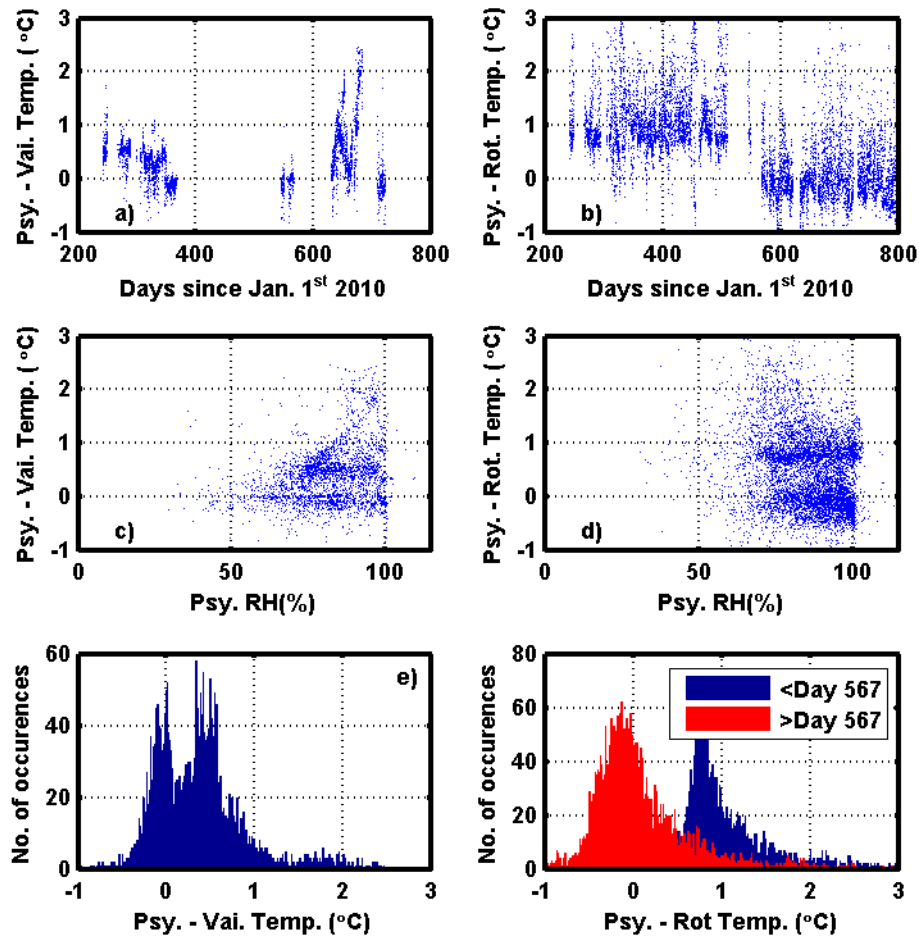
Figure 3.10 – Differences in true air temperature readings between the Psychrometer and Vaisala, and the Psychrometer and Rotronic. a) and b) show date dependence of the offset, c) and d) show relative humidity dependence, and e) and f) show histograms of the offset. In f), pre refit is in blue, and post refit in red

Figure 3.11 shows that both the Vaisala and Rotronic have a humidity offset from the Psychrometer that is correlated slightly with the humidity itself, although the scatter in the Vaisala offset is less than the scatter in the Rotronic offset. For relative humidity, the psychrometer was designated the primary sensor, the Vaisala the secondary and the Rotronic #2 the tertiary. The psychrometer humidity reading was discarded when the water reserve dried up or froze; these events were logged by the crew on a daily basis.

The relative humidity (RH) offsets, when plotted as a function of the psychrometer relative humidity, show an obvious sharp diagonal cut-off; i.e. there is a limit to how much larger the Vaisala/Rotronic RH can be than the psychrometer RH, at very high RH. This is almost certainly because RH is an atmospheric variable with an upper saturation limit. For example if the Psychrometer reads 95% RH, then the Rotronic at most can read 100% RH; the instrument is not capable of reading higher. This is only an issue at very high relative humidity (above 90%); during analysis of the latent heat transfer coefficients (Chapter 6) such records are rejected because the magnitude of random error in the RH measurement approaches the size of the air-sea RH difference (e.g. the Vaisala has random error of +/- several percent, even before the mean offset with the psychrometer is computed). Since random error is biased in one direction because of saturation at the upper limit, a normal distribution of random error in the air-sea RH difference cannot be assumed, and the statistics of the average latent heat transfer coefficients will be poor.

When the Rotronic is used as a substitute, the offsets take into account the elevation difference between the sensors. The offsets between the Rotronic and Psychrometer measurements depend on the vertical scalar profiles as well as instrumental offset, but the two influences cannot be separated. There may therefore be some small stability dependent bias in the best estimate of the mean temperature and humidity when the Rotronic was used
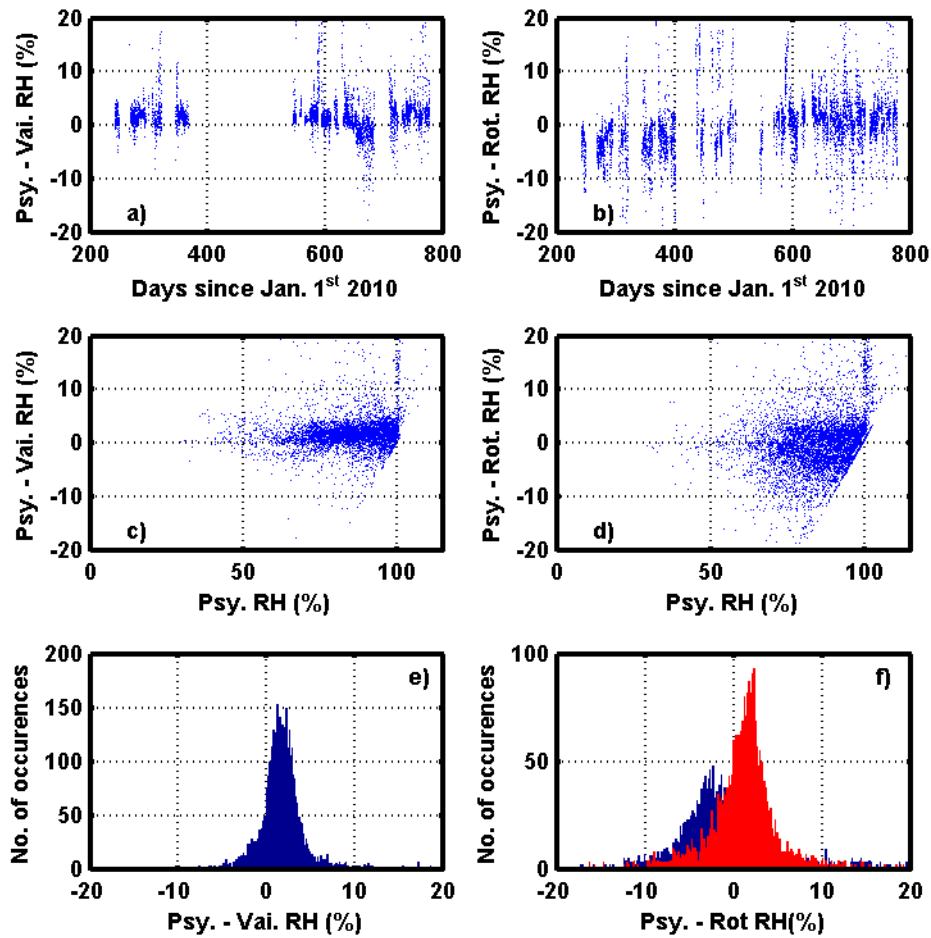
Figure 3.11 - Differences in relative humidity temperature between the psychrometer and Vaisala, and the psychrometer and Rotronic. a) and b) show date dependence of the offset, c) and d) show relative humidity dependence, and e) and f) show histograms of the offset. In f), pre refit is in blue, and post refit in red

3.3.8 Calculation of mean conditions

To develop drag coefficient parameterisations, the fluxes must be compared to the mean conditions at a standard reference height, rather than the measured height, to allow fair comparison between studies. The mean streamline wind speed measured by the anemometer was therefore corrected to a 10 m neutral equivalent value, using a stability-corrected near-logarithmic wind profile, to derive U_{N10}. The correction is relatively straightforward:

$$U_{N10} = U_Z + \frac{u_*}{k}\left(\ln\left(\frac{10}{z}\right) - \Psi_m(10/L) + \Psi_m(z/L)\right) \hspace{2cm} (3.18)$$

However, knowledge of the momentum and scalar fluxes is required to perform the correction as stated. The measured EC and ID fluxes could have been used but then bias in a given flux record would then affect both the flux and U_{N10} terms in the computed drag coefficient. U_{N10} is therefore calculated independently, using the COARE 3.0 bulk flux algorithm, which iterates to a solution using parameterised drag and scalar transfer coefficients. COARE 3.0 was developed using several large open ocean data sets from a variety of platforms and was considered by Brunke et al. (2003) to be one of the best performers; their study tested many flux algorithms against large sets of observations. Also extracted from COARE 3.0 were the Obuhkov length and the air-sea 10 m temperature and humidity differences.

Key inputs to COARE 3.0 are the wind speed, temperature, relative humidity, and the heights at which they were measured. Recalling from the literature review, a correction for mean flow distortion must be carried out. Distortion of the mean flow has been modelled around several vessels (e.g.: Dupuis et al., 2003; Pedreros et al., 2003; Yelland et al., 2002), and corrections to the wind speed and flow height were available for the JCR from Yelland et al. (2002). Unfortunately at the time of writing, only two modelled corrections were available; for bow-on flow and beam-on flow. The corrections to the mean flow are a very strong function of relative wind direction (e.g.: Figure 3.12), and corrections for one flow angle are only valid out to approximately ±10 degrees. This meant that only records that had mean relative wind directions within ±10 degrees of bow-on could be used to develop flux parameterisations. Records with beam-on winds were rejected because the momentum flux cospectra were of poorer quality, the modelled mean flow correction is much larger with more uncertainty associated with it, and there were much fewer beam-on data than bow-on.
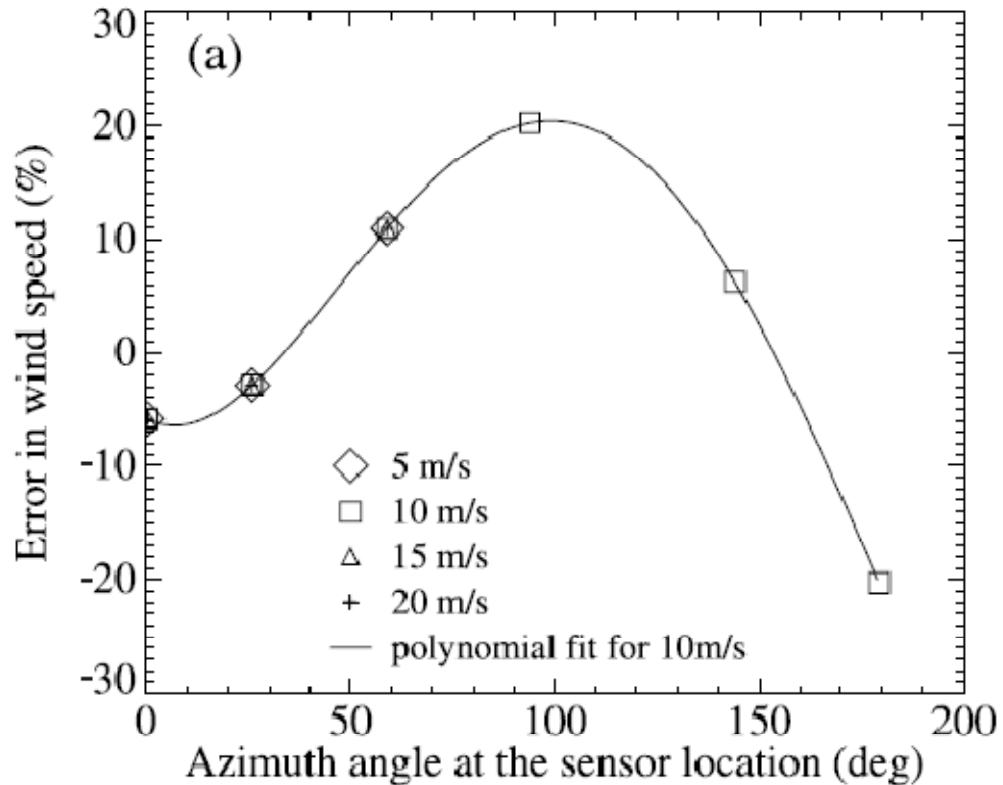
Figure 3.12 – From Dupuis et al (2003). Bow-on winds are at 0 degrees. The error in the measured wind speed is the change induced by flow distortion; it is very sensitive to the relative wind direction, though not to the wind speed.

Yelland et al (2002) used Computational Fluid Dynamics modelling to produce the corrections for the JCR; the model results were well matched to real data - the differences in measured mean wind speeds between pair of anemometers. The flow at the anemometer height (16.4m ASL) is decelerated by 1.3% and lifted by 1.6 m. The random errors in these corrections when compared to measurements were of order 1-2% When inputting this information to COARE 3.0, it is equally valid to use either the true height and the 1.3% correction, or to use the displaced height (18.0 m ASL) and the correction for that height (acceleration of 0.4%). The former option was chosen after the two methods were found to yield almost identical U_{N10} values for several test records.

The heights of the temperature and relative humidity measurements were input as the true instrument heights of 18.6 m ASL. Flow height displacement is thought

to be large over the bridge (about 7 m; pers. comm. Margaret Yelland) and so the air measured there originated at an altitude of about 10 m. Adiabatic expansion responds relatively instantly to flow height changes, so that the temperature and relative humidity have adjusted to the new pressure by the time they are measured. However this does not alter the potential temperature or the specific humidity. For example; during an upward heat flux there is a negative potential temperature gradient with height. The air measured will have originated from a lower height than the sensors, and so will be biased high with respect to the true potential temperature at 18.6 m (measured well away from the ship, say). Due to uncertainty in flow displacement corrections at the wheelhouse top this issue is impossible to precisely correct; it is simply acknowledged that the COARE 3.0 outputs of ΔT_{N10} and ΔQ_{N10} may have some residual bias from the true value.

Whilst most of the work of this thesis discusses the momentum fluxes, the final chapter presents a more limited discussion of the scalar fluxes. To compute these fluxes, the time series of true temperature and specific humidity were be calculated from the 'sonic' temperature (approximately equal to the virtual temperature), and the H_2O density.

$$T_{TRUE} = T_{SONIC}(1 + 0.15. q) \qquad (3.19)$$

$$q = \rho_{H2O}/\rho_{AIR} \qquad (3.20)$$

Where q is the specific humidity in kg water vapour per kg moist air, and ρ_{H2O} and ρ_{AIR} are the densities (kg m^{-3}) of water vapour and moist air. It is clear that q is required to calculate T_{TRUE} and that T_{TRUE} (via the air density) is needed to calculate q. An iterative method starting with ρ_{AIR} as 1.25 kg m^{-3} was found to converge to steady solutions after one or two iterations. The mean temperature is taken from the low frequency meteorological sensors, and the perturbations in temperature from the sonic anemometer; the mean sonic temperature is unreliable, with bias between sensors of similar model (pers. comm. Ian Brooks).

3.3.9   Calculation of fluxes

Prior to flux computation, a linear trend was removed from the turbulent time series, to remove variability caused by low frequency trends and instrumental

drift. An alternative method to remove low frequency variation is to directly apply a low-pass frequency filter. Such filtering is used by Moncreiff et al (1997), whereas Rannik et al (2001) use a linear detrend; the latter find that use of a filter is only a small improvement when there is prior knowledge of the nature of the low frequency variation, otherwise the detrending option is better.

The final step of all processing was to compute the fluxes themselves, using equation 2.6 for the EC flux and equation 2.21 for the ID flux. There are two additional considerations for the ID flux. First, the 1.6 m flow displacement correction is deducted from the anemometer height. This is because turbulence takes several seconds to readjust to a new height (Henjes 1996) when the mean flow is displaced, and so it is more appropriate to use a height of 14.8 m in the ID flux calculation. A correction is also made to the high frequency part of the u_S spectrum, to remove bias caused by the block averaging from 100 Hz to 20 Hz (Henjes 1999).

The processing and calculations shown thus far were applied to all flux records where possible, yielding 25'127 half hour momentum flux estimates. This included all the data that was obviously not useful, including port calls and periods of key instrument failure. This was filtered progressively, as detailed in the next section.

3.4   Quality control

3.4.1   Major events and data losses

After the summer 2010 refit, WAGES instruments were installed whilst docked in Vigo, Spain, during June 2010. Following this, the transit to Immingham was used as a shakedown cruise to test the flux instrumentation. The JCR follows a regular annual cycle of operations; a northern hemisphere summer season is completed in the summer and early autumn. The JCR then heads to the Southern Ocean for the Antarctic summer until March or April when it returns to the UK for refit work and then the next northern season. The scheduling and log of significant events from June 2010 to April 2012 is shown in Table 3.1.

Dates	Comments
25/05/10 – 06/06/10	**JR254A –** Vigo to Immingham. Prior to sailing, Autoflux and bridge cameras installed. Instrument testing.
13/06/10 – 30/07/10	**Arctic Season** Transit to Svalbard and cruises frequently in sea ice.
31/07/10 – 02/10/10	**Refit in UK –** Wave radar, mean meteorological sensors and CLASP installed.
02/10/10 – 25/10/10	**Southern Ocean Transit to Stanley**
25/10/10- 28/04/11	**Antarctic Season –** includes two IOP cruises (see below) and a wide range of marine research work.
14/12/10 – 17/12/10	**JR254B** Kite camera tested but failed. Buoy deployments.
19/03/11 – 06/04/10	**JR254C** Helikite successfully tested, buoy deployments and WAGES cruise time in winds up to 20m/s.
28/04/11 – 15/05/11	**Northern transit to UK**
27/07/11 – 14/09/11	**Arctic Season –** Work around Svalbard. In July 2011 the ships meteorological sensors are replaced
24/09/11 – 20/10/11	**Southern transit** – Motion sensor fails 10th Sept, undetected until 27th November on next IOP. Flux data rejected.
23/10/11 – 25/04/11	**Antarctic Season -** includes two IOP cruises (see below), wide range of marine science work. End of data used in this thesis.
27/11/11 – 26/12/11	**JR254D** – Licor 7200 installed. Motion sensor repaired.
27/03/12 – 24/04/12	**JR254E –** Licor 7200 replaced at end of cruise

Table 3.1 – Itinerary and event log for June 2010 until April 2012

Daily metadata was available from NOC internal web pages, managed by Ben Moat; there were dates of port calls, instrument failures, Li-7500 shrouding, psychrometer reservoir freezing or drying out, and other useful miscellaneous

notes. This information was turned into a set of Matlab flag arrays, time matched to each record, so that data filtering was flexible and automatic.

The following filters were applied progressively: 5407 records were removed from the data set when the ship was in port; the motion pack failed for 2038 records; there were no temperature readings for 80 records and no relative humidity readings for 503 records. When the non-toxic water supply was switched off (usually in sea-ice) there was no sea temperature measurement, this removed 3743 records. At this point there were 13'356 records that passed the most basic quality control.

Several parameters were then examined for unrealistic values. 50 records had mean relative wind speeds greater than 27 m s^{-1}; further scrutiny showed these to be from corrupted anemometer data. 807 were rejected when the wind direction was from ±60 degrees of astern, because the turbulence would inevitably be contaminated. 329 records were rejected when the relative mean tilt (calculated using the relative mean wind speed) was outside the range of -5 to 12 degrees; these were found to be from corrupt anemometer data or taken at very low mean wind speeds (less than 3 m s^{-1}). Fluxes calculated from very low wind speed data are not reliable because of the uncertainty in the mean tilt. At this point 12'170 data remained.

Figure 3.13 and Figure 3.14 show the track of the JCR in the Southern Ocean, with line colour indicating half hourly mean values of true wind speed, wind direction relative to the ship, air temperature and sea surface temperature. Figure 3.15 and Figure 3.16 show similar track plots from the northern hemisphere. Figure 3.17 shows the distribution of mean conditions throughout the two years, split into data from below 48° South and the remainder. Note that the remainder includes all data from north of 48˚S, which are included in histograms, but only data from above 35˚N are shown in the track plots, for clarity.7656 records were from the Southern Ocean, and 4514 from north of 48˚S.

Looking at Figure 3.17 and all 12170 values; 88% of half hourly averages of the 10m mean wind speed (U_{10}) are between 4 and 16 ms^{-1}, and the median is 8.4 m s^{-1}. 93% of sea surface temperatures (*SST*) are below 6˚C, but values extend up to 28˚C in the relatively small data set from the tropics. The difference between air

and sea temperatures (ΔT_{10}) is defined as the sea temperature minus the 10 m air temperature (T_{air10}). ΔT_{10} follows an approximately normal distribution with a zero mean, with a slight skew toward stable conditions. This means that the surface layer turbulence is overwhelmingly wind driven, as can be seen from the stability parameter, which is between +/- 0.3 for 86% of data. Encouragingly there is a large peak in the relative wind direction for bow on flow, during which data quality is higher than for other relative flow directions. 32% of relative wind directions are within 30 degrees of bow on, and 56% within 60 degrees of bow on.

The data not from the Southern Ocean are from the Atlantic transit legs across the equator, and from various cruises around the UK, Western Europe, and the Arctic. Naturally, conditions vary tremendously, but there was a consistent period of operations to the west of Svalbard. Here, the relative wind direction appears to be very frequently from aft, and when this is the case, these data must be rejected. Cruise reports detailed that a considerable amount of science work in the Arctic involved shallow coastal waters and sea ice.

.
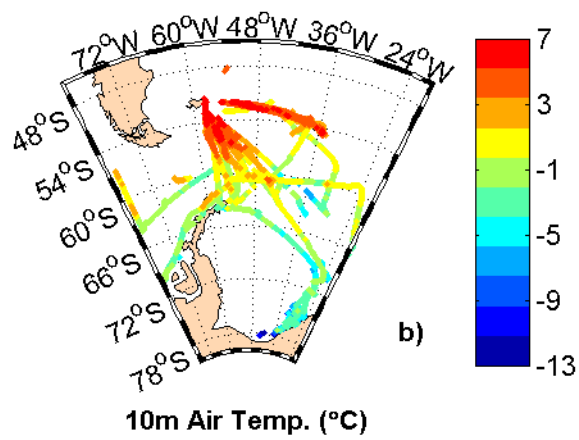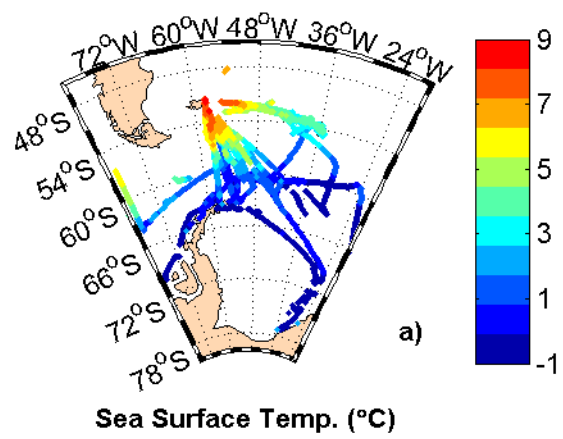
Figure 3.13 – Track plot in the Southern Ocean region, coloured by a) Sea surface temperature, and b) air temperature.
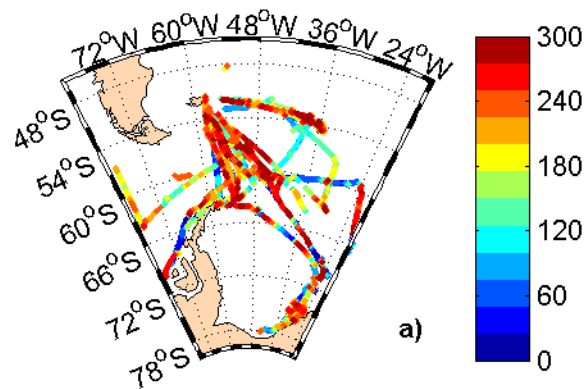
Relative Wind Dir. (180° = bow on, 270° = Stb. on)
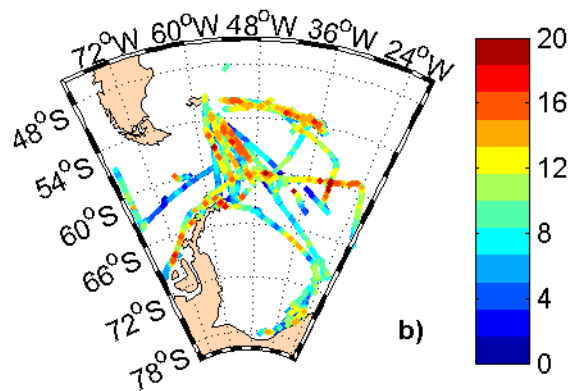
10m Mean Wind Speed (m/s)

Figure 3.14 - Track plot in the Southern Ocean region, coloured by a) relative wind direction and b) mean true wind speed. 180 degrees is for bow on flow, and 270 is for starboard on flow

a)

Sea Surface Temp. (°C)

b)

10m Air Temp. (°C)
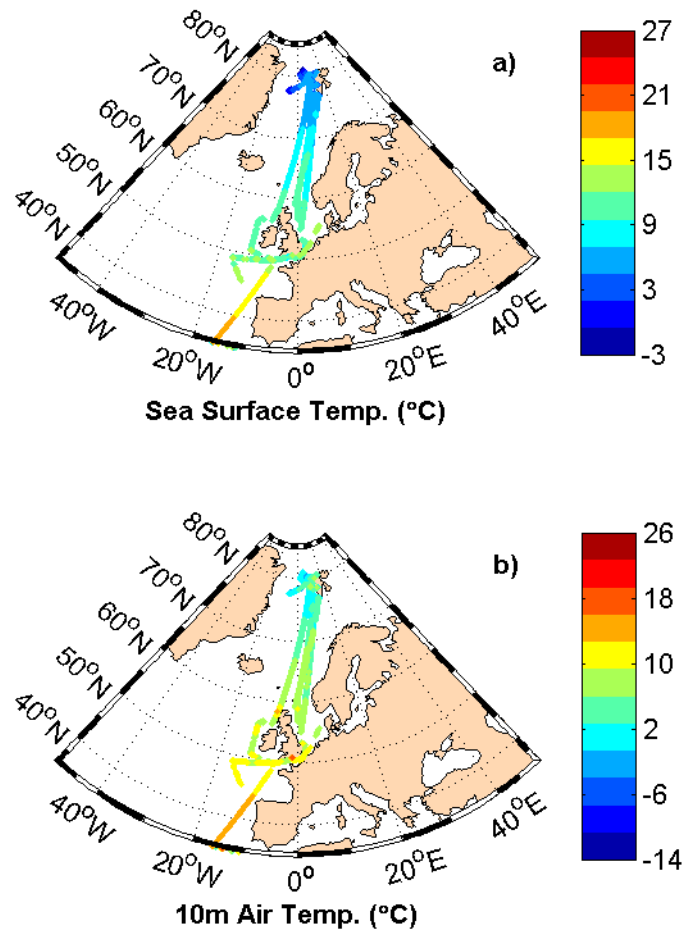
Figure 3.15 - Track plot in the Northern Hemisphere, coloured by a) sea surface temperature, and b) air temperature.

Relative Wind Dir. (180° = bow on, 270° = Stb. on)

10m Mean Wind Speed (m/s)
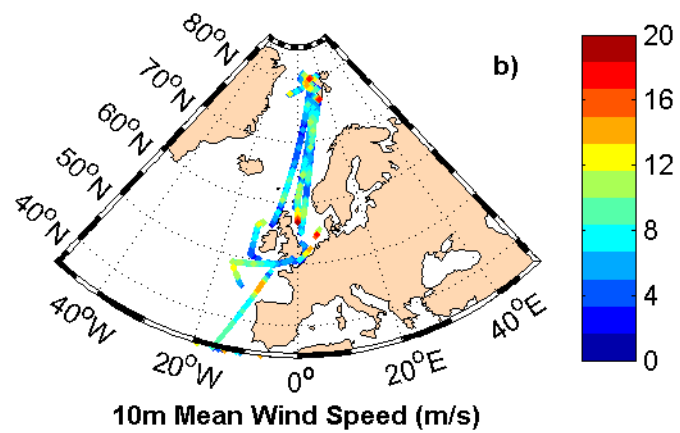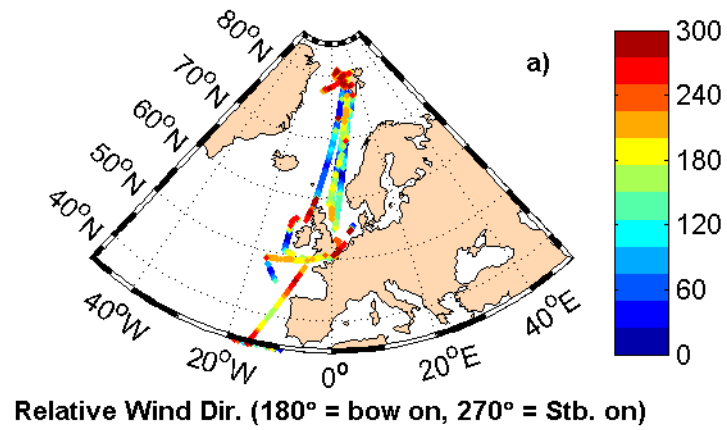
Figure 3.16 - Track plot in the Northern Hemisphere, coloured by a) relative wind direction and b) mean true wind speed. 180 degrees is for bow on flow, and 270 is for starboard on flow.
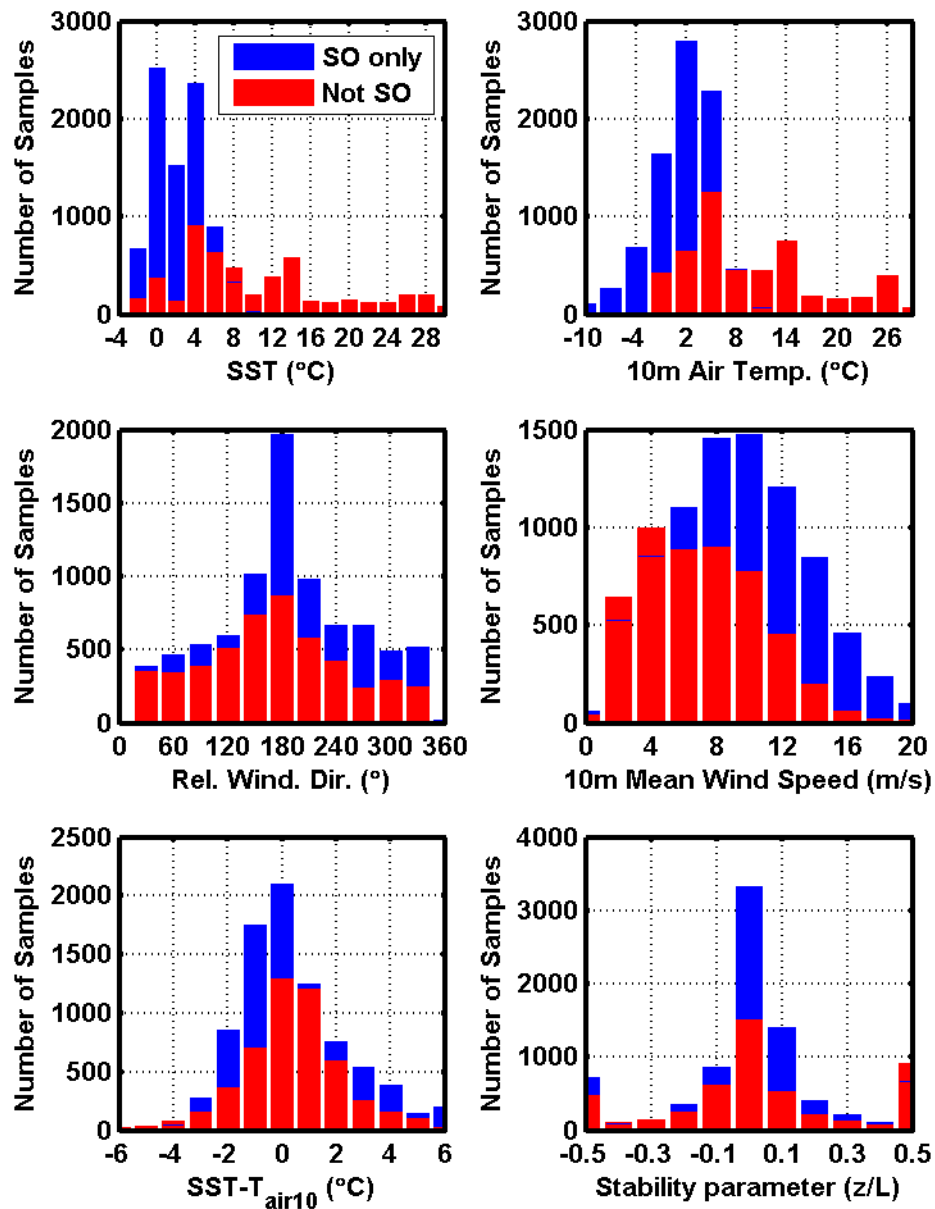
Figure 3.17 – Histograms of half hourly mean conditions; the blue indicates Southern Ocean data, and the red indicates data from elsewhere. Temperature and wind speed measurements are corrected to 10 m height above sea level.

The JCR cruise path during WAGES included areas as diverse as the Drake Passage, Weddell Sea, North Sea, Arctic Ocean, Equatorial Atlantic and English Channel. Records were screened for very short fetch cases by computing the distance to the nearest shore that lay opposite the mean true wind direction. The curvature of the earth was compensated for using the WGS84 spheroid projection. 906 records had fetches less than 50km, 1618 fetches less than 100km, 3544 fetches less than 500km, and 5716 fetches less than 1000km. 100km or more definitely removes the very short fetch cases and left easily enough records to achieve the aims of this thesis. 10552 records were therefore kept.

A separate method was required to remove records that were measured near to sea ice, with possible short fetches depending on the wind direction. A simple latitude filter was justified given the large volume of data available; in the north, 1652 records were taken above 75 degrees north, to the west of Svalbard and often in or around summer sea ice and rejected from the data. 80 records from the English Channel were rejected; mostly too close to the English south coast, where water depths are of order tens of metres around the cruise track. In the southern hemisphere, below 65 degrees south, there are two regions: one is the Weddell Sea, where the cruise track skirts the sea ice. The other is west of the peninsula – at least some of these data were taken near sea ice. To be conservative, all 907 data south of 65 degrees south was rejected. This left 7913 records of open ocean flux measurements along with reliable measurements of average conditions.

3.5   Flux Results

In this section, a first assessment of the flux results, and resulting drag coefficient vs. U_{N10} relationship, is presented. It became clear that the basic quality control described in the previous section was insufficient. The ID results matched the parameterisation of Yelland et al. (1998) near-perfectly, which was encouraging because the ship, location, and method were identical. However, understanding of air-sea momentum exchange is not improved because open ocean ID fluxes have been extensively published. The EC results were found to be extremely poor, after only basic quality control. However, after the novel corrections and quality control methods introduced in Chapters 4 and 5 were applied, then the EC results

showed close agreement with the parameterisations of others; this is discussed in due course.

Before direct comparison between EC, ID and COARE 3.0 could be carried out, it was apparent that the ID fluxes were biased low with respect to COARE 3.0 when the ship was steaming into the wind. However when the ship was holding position, there was an excellent match between the two. Of the 7319 records that passed all the basic quality control steps of the previous section, 1330 had relative wind directions close to bow-on (± 20 degrees). Of these records, 476 were taken when the ship was holding position and 854 taken when the ship was steaming ahead into the wind, usually at approximately 6 m s $^{-1}$. The ratio of the ID momentum flux and the flux output by COARE 3.0 was used to assess differences. As a first pass, any records where this ratio was more than 3, or less than 0.33, were discounted from the following statistics; at this point in the investigation it is sufficient to acknowledge that some records are of poor quality, without yet exploring the causes. The ratio of ID flux / COARE 3.0 flux was on average 0.95 with a standard deviation of 0.16, for the records taken when the ship was holding position. This ratio was 0.81 on average with a standard deviation of 0.21, when the ship was steaming ahead. The 5% low bias in the ID fluxes when the ship is on average stationary is expected, given the low bias of Yelland et al. (1998) with respect to COARE 3.0. However the additional 15% low bias introduced by steaming ahead is of concern; it means that the mean lateral motion is at some stage of the flux calculation introducing measurement bias. The application of Eq. 2.21 to calculate the ID flux requires input of the mean relative wind speed; careful checks were made that the relevant Matlab codes used the correct mean wind speed (and not for example the true wind speed). The bias is therefore not due to the apparent frequency of turbulence increasing, as seen by the sensor as it moves against the wind direction; use of the relative wind speed accounts for this effect. It must be concluded that the variance of the horizontal wind speed in the inertial sub range is reduced by lateral mean ship motion. As shown in Figure 3.8, the EC fluxes after all relevant corrections have been applied are not affected by lateral ship motion. The reasons of the ID low bias caused by mean motion can be speculated at, but it is not necessary to do so, because there are enough ID flux records taken when the ship is not steaming,

to demonstrate a well constrained flux parameterisation; therefore this issue is not investigated further.

A direct comparison of the ID, EC, and COARE 3.0 results were performed on the 476 records taken when the ship was nominally stationary and the mean wind direction was ±20 degrees from bow-on (Figure 3.18).
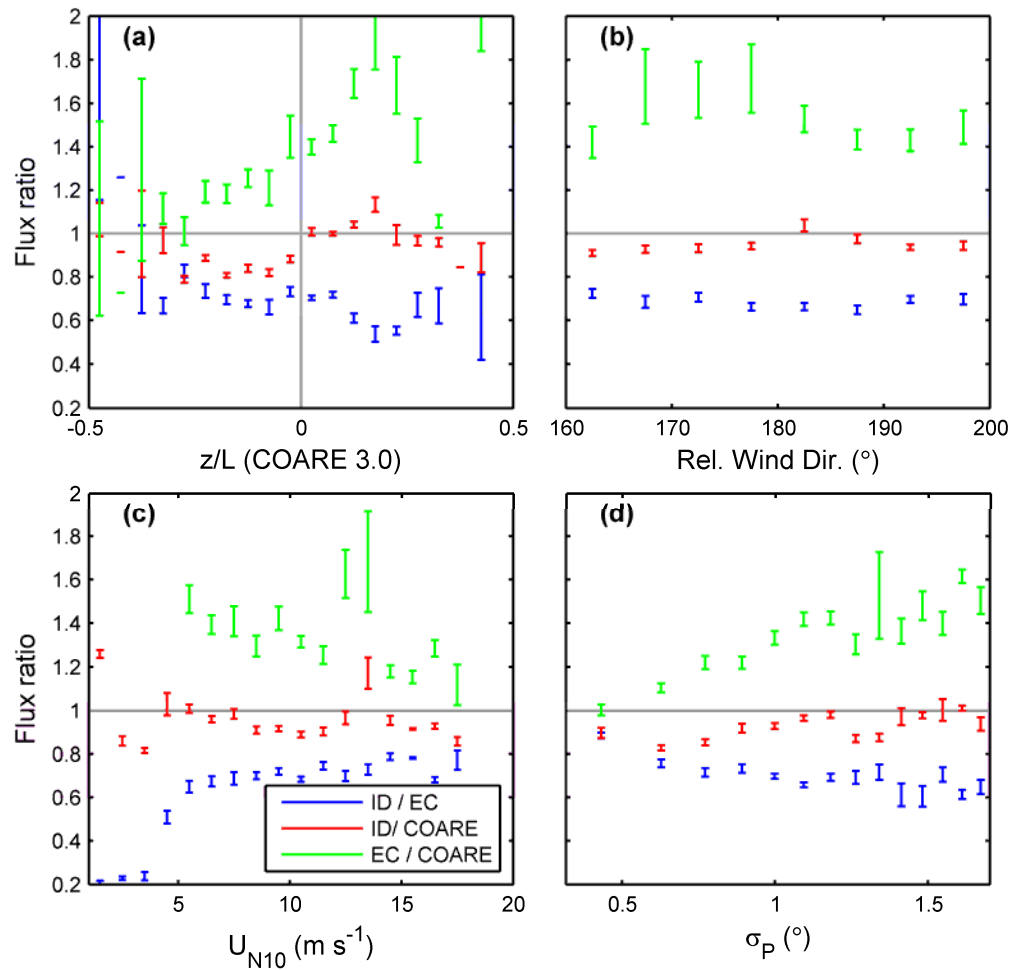
Figure 3.18 – Ratios of fluxes computed for each record, when the ship was holding position and the relative wind direction within ±20 degrees of bow-on. Displayed as a function of: a) the stability parameter output by COARE 3.0; b) the relative wind direction; c) The mean 10 m wind speed; and d) the standard deviation of pitch. Error bars are standard error of the mean.

.

Several important observations can be made:

- The stability parameter as calculated by COARE (z/L) has a strong influence on the momentum flux output, particularly evident from the EC / COARE ratio vs. z/L. It is likely that errors in the input of the mean air-sea temperature and humidity differences (Section 3.3.7) are the cause; bias in z/L as computed by COARE would propagate to the momentum flux computation. It is encouraging that the ID / EC ratio has relatively little dependence on z/L.

- EC fluxes are on average approximately 30% higher than ID fluxes. This bias is a strong function of how large the pitching motions of the ship are (as represented by the standard deviation of the pitch). It is likely that flow distortion of the turbulence induced by ship motion is causes bias to the EC fluxes; this is investigated in detail over the next two chapters.

- There is more scatter in the EC / COARE ratio when flow is from port than from starboard. The EC / ID ratio does not show as much dependence of scatter on the relative wind direction. It is therefore likely that the cause of EC / COARE scatter lies with COARE, so the scatter is linked to mean, rather than turbulent, flow distortion. This is sensible given that the sensors are on the starboard side so flow from starboard encounters less distortion.

- Below mean wind speeds of 4 m s^{-1}, disagreement between the three methods is very severe. As acknowledged by Yelland et al. (2002), flow distortion patterns are likely to change at very low wind speeds. The flux results at low wind speeds (U_{N10} less than 5 m s^{-1}) are therefore discarded from the remainder of this thesis; a ship is not the best platform to use in such benign conditions

It is clear that without further quality control and a method to account for turbulent flow distortion correlated to ship motion, the EC results are completely unreliable. It is demonstrated in due course that after application of many quality control and correction techniques developed as part of this thesis, the EC results

can be brought into a much more reasonable level of agreement (a few percent on average) with the ID and COARE results.

The ultimate objective of this work is to evaluate the relationship between the momentum flux and the wind speed, so plots of the drag coefficient feature prominently throughout this thesis. Only records with relative wind directions ±10 degrees from bow-on can be used to compute the drag coefficient because of the need for a flow distortion correction; it is demonstrated in the next chapter how much the relative wind direction biases the drag coefficient, and that only ±10 degrees is permissible. This criterion allows only 1710 of the 7931 records to be used. Further restrictions were imposed, allowing only records with relative and true wind speeds above 5 m s^{-1} to be used, leaving 1319. As a final, crude method of quality control, records in which CD_{N10} from either the EC or ID fluxes was greater than 0.01 were rejected, to remove very high outliers that prevented meaningful relationships to be plotted; this left 799 records, the results shown in Figure 3.19.
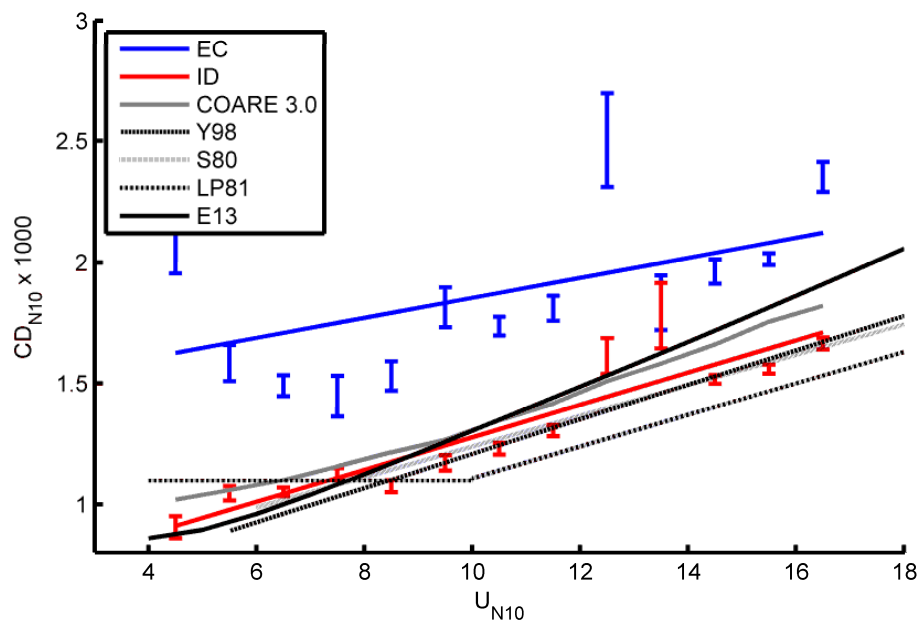
Figure 3.19 – 10 m neutral drag coefficient vs. 10 m neutral wind speed. The results of COARE 3.0 (Fairall et al, 2003), Yelland et al (1998; Y98), Smith (1980; S80). Large and Pond (1981; LP81) and Edson et al. (2013; E13) are shown. Error bars indicate one standard error of the mean.

Before considering the fluxes themselves, bias in the computed value of U_{N10} must be considered. Taylor and Yelland (2001) demonstrate by using synthetic data, that random scatter in the temperature and humidity measurements about the true value can have a non linear effect on the U_{N10} calculation. This they argue, explains the apparent stability dependence of the drag coefficient observed in other ID experiments. Other authors attribute this to a stability dependent 'imbalance' term in the TKE budget that must be parameterised in order to use ID flux measurements; no resolution to this controversy has yet been presented.

Any bias in U_{N10} should fortunately not be unequally distributed across the wind speed range. All modelling studies show a near zero dependence of mean flow distortion on the relative wind speed; with the exception of very low wind speeds. Over the range presented here, use of a single correction (modelled at 15 m s^{-1}; Yelland et al., 2002) is perfectly reasonable; any bias likely to be eclipsed by other sources, detailed in due course.

The ID results are well modelled by to a linear fit to U_{N10}, with an R^2 value of 0.95. The ID linear fit conforms to 1000 x (ID) $CD_{N10} = 0.61 + 0.065\ U_{N10.}$ This is near identical to Smith (1980); 1000 x (S80) $CD_{N10} = 0.61 + 0.063\ U_{N10}$, and similar to Yelland et al. (1998); 1000 x (Y98) $CD_{N10} = 0.5 + 0.061\ U_{N10}$. Two bin averages at 12.5 and 13.5 m s^{-1} deviate significantly, and since only very basic quality control has been applied at this stage, this is not surprising. The match to Yelland et al. (1998) is expected given that the same technique was used. However, controversy persists about the use of the ID method at sea as described in the previous chapter. The ID results are approximately 10% less than COARE 3.0. As noted in the literature review, there are two proffered explanations for this behaviour: one that the ID results are biased low because there is greater local creation of turbulence than is dissipated, because some turbulence energy is expended on wave growth; the other that the ship based measurements underpinning COARE 3.0 are biased high from flow distortion.

The eddy covariance results without careful quality control are unimpressive. There is a lot of scatter and a low level of confidence in a linear fit to the data, with an R^2 value of 0.19 for the bin averaged values. The linear fit conforms to 1000 x (EC) $CD_{N10} = 1.43 + 0.043\ U_{N10}$; this is substantially higher than given in

all publications. No attempt was made to do a higher order fit; the scatter is too high to have confidence. The standard error in the each mean bin is far larger than those of the ID method. Moreover there is a large positive offset in the linear fit, showing that most records have unreasonably large fluxes.

Many authors have found that EC momentum fluxes from ships, even after motion correction, are significantly biased with respect to inertial dissipation fluxes or those from co-located tower- or buoy-based EC measurements. Most (e.g.: Edson et al., 1998, Pedreros et al., 2003) simply quantify the average bias, and attribute it to a combination of airflow distortion and imperfect motion correction. No study has attempted to investigate the physics of motion correlated flow distortion; the present literature review is therefore fairly limited. It is noted that there are no published drag coefficient parameterisations that rely solely on ship-based open ocean EC measurements. The final outcome of this thesis is such a parameterisation that matches the work of others to within several percent.

Edson et al. (1998) found that ship-based EC momentum fluxes, made 11.5 m above sea level, were biased high on average by 15% compared to those measured from the stable platform *R/P FLIP*, and to the results of COARE 2.6 (Fairall et al., 1996) over the open ocean. However, Edson et al. restrict the wind direction to ±120; such a large range leaves too much variability on the results caused by wind direction dependent bias in the mean wind speed measurement. There also may be an (not proven or quantified) effect on the fluxes themselves from relative wind direction dependent turbulent flow distortion. After motion correction, the residual contamination in the vertical velocity spectra and momentum flux cospectra is stated to be negligible, although only a single example flux cospectrum is presented (Edson et al., 1998; their Figure 9) in which noise levels are high. Edson et al. (1998), also demonstrate that the bias in the momentum flux is dominated by flow distortion rather than imperfect motion correction using the following reasoning. Motion corrected fluxes from the ship and a catamaran were each compared to the results of COARE 2.6. The catamaran vs. COARE comparison had relatively small bias scatter than the ship vs. COARE comparison. The catamaran has a greater motion range but smaller

flow distortion than the ship, meaning that flow distortion is more important than imperfect motion correction.

Donelan et al. (1997) compare catamaran-based measurements of EC and ID fluxes, and conclude that during pure wind-sea conditions the two methods match well (RMS error of 9.8%), but during significant swell there is greater disagreement (RMS error of 22.7%). The bias direction of an individual record is dependent on the relative direction between wind and swell propagation. Their conclusion is that during swell the assumptions required for the ID method are invalid and the ID fluxes do not detect the swell-induced flux detected by the EC. They provide further evidence that flow distortion is more important than imperfect motion correction; at higher wind speeds with the same craft motion range, the wave field is more dominated by wind-sea. The EC vs. ID bias is reduced in these conditions, meaning that the motion correction is adequate and the bias is caused by swell.

Brut et al. (2005) found that EC fluxes were biased low by 30% with respect to both the ID fluxes and the results of the COARE 2.6 algorithm, although there was a good correlation between the EC and ID ($R^2 = 0.85$) results. Similarly to Edson et al. (1998), they provide one example motion corrected spectra, but it is noisy and a clear motion correlated residual bias is not evident. EC The bias is of a different direction but the authors stated that their motion correction in the horizontal plane is more limited than most ship-based EC setups.

Pedreros et al (2003) found that ship-based EC fluxes are biased high by 18% on average compared to those made from an ASIS buoy (Graber et al., 2000). Similarly they found a high EC bias compared to ID, when the ID method had included corrections for mean airflow distortion. They found no residual wave correlated anomaly in the EC spectra.

3.6 Summary

WAGES yielded around a thousand reliable measurements of the momentum flux over the open ocean momentum for which mean flow corrections were available and so could be used for developing a parameterisation of the drag coefficient. It

was found that WAGES inertial dissipation results agree well with similar studies from the literature. The EC method is in theory more robust, but rigorous quality control is required. It is shown in the following two chapters, which form the major contribution of the author to advancing the current state of knowledge, that quality control by examining spectra can be used to remove biases. Contamination of the wind from motion-correlated flow distortion was then investigated, to yield robust corrections.

4 Automated spectral quality control

The linear fit between the drag coefficient and. wind speed, derived using the EC momentum fluxes, had significant mean bias and low confidence when compared to a parameterisations from the literature, and one derived from the ID fluxes. However, the EC method, unlike the ID, yields a direct flux measurement and so avoids the need for the assumptions and empirically derived constants that make the ID method controversial. Bias in the EC fluxes is therefore worth studying and attempts made to introduce quality control and/or defendable corrections.

Making EC measurements from a ship introduces significant additional challenges when compared to measurements from a fixed platform. The direct influence of platform motion on the turbulent wind measurements must be corrected for (section 2.3.4). The superstructure of the ship causes flow distortion, which is likely to respond to periodic ship motion. Distortion of turbulent flow over a ship is poorly understood. Distortion of the mean flow has been shown to respond to the ship's pitch (Brut et. al., 2005), which would likely lead to pitch correlated aliasing of u_S into w_S after application of a single mean tilt rotation (section 3.3.5).

In addition to flow distortion and platform motion issues, eddy covariance measurements in any environment can be biased by a number of other factors, such as mesoscale variability that is unrelated to the local turbulent flux (Sun et. al., 1996), non-stationarity (Vickers and Mahrt, 1997), or when the assumption that the flux is constant with height is not valid; i.e.: during very stable conditions when the sensors are above the surface layer (Sjoblom and Smedman, 2002), of if there is significant flow divergence caused by mean flow acceleration.

A subjective quality control of EC flux estimates from ships is commonly undertaken via inspection of the flux cospectra or ogives to ensure that the turbulence is well behaved at all scales contributing to the flux (e.g. Fairall et. al., 1997). This becomes increasingly laborious as the data volume increases, and is unavoidably prone to some level of subjective error. In some instances, very large data sets are required to reduce the uncertainty in parameterisations to acceptable levels; for example, studies of the air-sea flux of CO_2 suffer from a small signal to

noise ratio (e.g. Prytherch et. al., 2010). Over the 18 month period during which the relevant data was collected, thousands of flux estimates were made of each five flux types (momentum, heat, water vapour, CO_2 and aerosol); it would be a daunting task to visually inspect each cospectrum, and almost impossible to guarantee consistency.

There are relatively few published quality control methods specific for EC measurements. Foken and Wichura (1996) outline two tests; one tests the variability between fluxes calculated from 5 minute sub sections of an individual record, to identify non-stationarity of the turbulence. The second test checks that records obey standard flux-variance relationships developed over land. The second test is not valid for ship use; the tests as published rejected almost all WAGES records because of the motion correlated flux contamination.

The work detailed here approaches quality control from a different and novel perspective: several parameters are derived from individual flux cospectra and ogives, and used to quantify deviations from an ideal cospectral form (Kaimal et al., 1972). The parameters allow classification of different types of spectral contamination with characteristic frequency ranges. The motion correlated contamination is corrected for using interpolation; a more sophisticated and defensible method of correction is the subject of the next chapter.

4.1 Common contamination types

The ogive function, $O(f)$, is the cumulative integral of the cospectral density:

$$O(f) = \int_f^\infty C_{uw}(f) df \qquad (4.1)$$

For the neutrally stratified case, the Kaimal cospectral form for momentum is (Kaimal et. al., 1972):

$$\frac{-f C_{uw}(f)}{u_*^2} = \frac{14n}{(1 + 9.6n)^{2.4}} \qquad (4.2)$$

where n is the normalised frequency $n=f\ (z/U_{REL})$, z is the measurement height (m) and U_{REL} is the mean relative wind speed past the sensor (m s^{-1}). Figure 4.1 shows an example of the frequency weighted cospectra and ogive that closely

match the Kaimal function. The underlying assumption of the quality control algorithm presented here is that well-behaved turbulence should follow the Kaimal form; evidence for this is presented in 2.2.1, providing that measurements are not taken in conditions of low winds *and* strong swell – one reason that records with U_{N10} less than 5 m s^{-1} were rejected from this analysis.
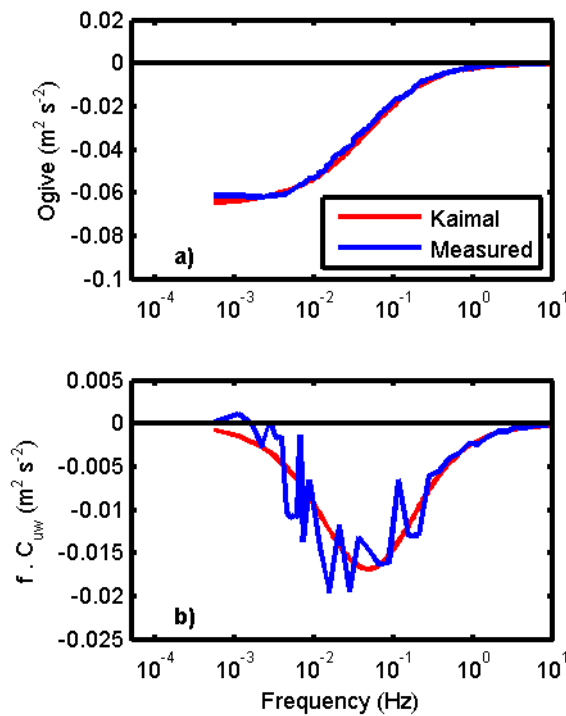
Figure 4.1- Example of the a) ogive function of the b) frequency weighted cospectrum computed from one momentum flux record. The cospectrum has been bin averaged with 8 frequency bins per decade. The Kaimal forms are shown in red, and the measurements in blue.

Several common deviations from the Kaimal form were found throughout the WAGES data set, examples are shown in Figure 4.2. Pairs of ogives and bin averaged cospectra are displayed from six records – the ogives are much less noisy and have not lost resolution through bin averaging. This meant that ogives rather than cospectra were used for quality control in this work. The ogive in Figure 4.2.a converges at both high and low frequencies and has little deviation from the Kaimal form across the turbulent spectrum; therefore there is confidence in this flux estimate. Severe contamination within the frequency band of the ship's motion is evident in Figure 4.2.b. This is likely to be caused by flow distortion correlated to ship motion. The ogive in Figure 4.2.c closely follows the

Kaimal form, with a clear upper and lower frequency convergence point, but a sharp spike is present around 10^{-3} Hz, the lowest range of frequencies. This is likely due to mesoscale wind variation or a ship heading change during the record. The convergence at frequencies just higher than the spike indicates that the turbulence is well behaved. Figure 4.2.d shows an ogive with significant covariance at frequencies above those expected for the turbulent flux, i.e. above 2-3 Hz (Stull, 1988). This may be caused to some extent by aliasing of true turbulence at frequencies above 10Hz (the Nyquist frequency; see Stull, 1988, for a full discussion), into the frequency range just below 10Hz. However it could also be instrument failure.
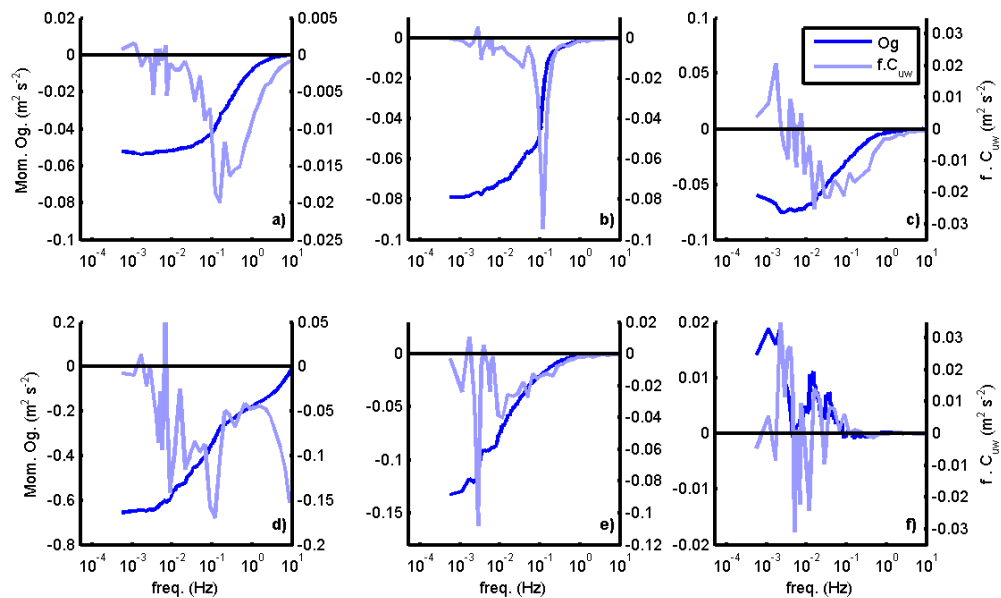
Figure 4.2 - Characteristic examples of the momentum flux ogive and frequency weighted cospectra, chosen to demonstrate six different types of commonly observed features. a) Well matched to the Kaimal form. b) Suspected ship motion correlated contamination. c) Low frequency contamination but a well defined turbulent flux range. d) High frequency contamination. e) Low frequency contamination and no well defined turbulent range. f) Poorly defined contamination.

Figure 4.2.e shows an ogive for it is which possible that the averaging time is too short for convergence to be reached at the low frequency range. It is also possible that mesoscale variance and the low frequency limit of turbulence overlap. Finally, Figure 4.2.f shows a record with poorly behaved turbulence and/or severe measurement bias; such a record should be rejected.

The automated quality control method was designed to identify specific types of contamination. All the features described above may be observed in isolation or in combination, and with a wide range of magnitudes and directions. Therefore the setting of thresholds for rejection of records based on ogive parameters is inevitably subjective to some degree. The purpose of the quality control method is to remove bias from EC flux measurements, and this purpose was adhered to throughout the development of quality control.

4.2 Overview

The data set used in this analysis had basic quality control applied as in section 3.4, accepting 7913 records. The relative wind direction acceptance range is ±60 degrees rather than ±10 degrees from bow-on, because the effect of relative wind direction (in addition to the ogive shape) on data quality was studied here. Records with true or relative mean wind speeds less than 5 m s^{-1} data are rejected, accepting 4615 records.

In the following sections, a set of parameters are defined that describe important ogive features. Four tests are described that define threshold values of these parameters in order to accept or reject data. In addition to the four tests, one correction is described; for motion contamination; note that none of the four tests modifies the resultant flux value, but the correction does. This correction is applied to every flux record and so no records are rejected on this basis. In order to set thresholds for each of the four tests, it was important to study a large set of records, in order to prove that bias is function of the tested parameter. Therefore it was necessary, when investigating the thresholds for each test, to only accept records that a) passed the other three quality control tests, and b) were corrected for motion contamination. Therefore there is not a common data set used for each section of this chapter. All efforts are made at the start of each section to highlight precisely which data are under examination. For additional clarity, a qualitative overview of this chapter is provided here; discussion is sequenced as follows:

- A method to fit the functional Kaimal form to the measured ogive is discussed (section 4.3). A small fraction of records have such poor ogives that the curve fitting procedure fails and the record is rejected.

- Correction for motion-correlated contamination (section 4.4). The ogive is interpolated over the range of ship motion frequencies. The Kaimal form is fit to both the unaltered and interpolated ogive. Differences between the unaltered and interpolated fits can be used to define thresholds for the detection of motion contamination. It is however shown that the vast majority of ogives have some level of unidirectional motion contamination, so that *all* ogives should be interpolated to ensure consistency and minimise bias in average flux results. Thus there is no rejection of records due to motion contamination. This is the only correction applied in this chapter; no other test applies alterations to the output flux value.

- Test for high frequency contamination (section 4.5). The fraction of the flux that is at high frequencies (above approximately 1 Hz) is found, and bias studied as a function of this fraction. It is shown that records with any non-negligible frequency contamination should be rejected.

- Cospectral peak frequency test (section 4.6). Records that have too large or small a peak frequency of the Kaimal fit to the interpolated cospectrum are rejected. If the peak frequency is too low, then the ogive on average does not converge; if the peak frequency is too high, then interpolation over motion scales is unreliable. Threshold frequencies are set.

- Relative wind direction test (section 4.7). This is not a test of ogive parameters, but of the bias in the drag coefficient related to deviations from bow-on winds. It is found that for a single modelled mean flow distortion correction, relative wind directions must be restricted to ± 10 degrees.

- General quality test (section 4.8). This allows detection of poor ogives, most of which have large low frequency contamination, but also those with unusual behaviour not captured by any of the other tests. It is based on the differences between the interpolated ogive and the Kaimal fit to the interpolated ogive.

So for example, when describing the cospectral peak test, the data set used passed the high frequency, general quality, and relative wind direction tests. The interpolated ogives are used, but no data is rejected because of motion contamination. The cospectral peak test is of course not applied because this is the parameter being tested, so a full range of values is permitted.

4.3   Kaimal form fitting

The Kaimal ogive is derived by the Leverson-Marquadt iterative nonlinear regression technique (Seber et. al., 2003) using the functional form relating the ogive to frequency that as derived by analytical integration of Eq. 4.2, using the constants there as initial values. It was found that a direct attempt to fit the Kaimal cospectral form in Eq. 4.2 to the measured cospectrum resulted in a much poorer fit than if the measured ogive was used. Prior to curve fitting, the measured ogive is bin averaged by frequency, using 8 bins per frequency decade. This is required because the increase in sample density at higher (logarithmic) frequencies would forces the Kaimal form to a good fit at high frequencies but often at the expense of a poor fit to the lower frequencies. The Kaimal ogive is not forced to converge at or high or low frequencies.

Two parameters were produced as part of the fitting process. The first was the frequency of the peak of the Kaimal frequency-weighted cospectrum (f_P), referred to hereafter as the cospectral peak frequency. Note that due to noise in the measured cospectrum, the Kaimal form is always preferred to the measured when estimating the cospectral peak frequency. The second is a general 'ogive quality' parameter that quantifies the difference between the measured and the Kaimal-fit ogives. The correlation coefficient between the fitted and measured ogives was ineffective to quantify differences, because there were a large number of points in the ogives that had near-perfect matches towards high frequencies, where the flux is typically near-zero. Even poorly fitted curves had R^2 values above 0.990. A more useful parameter was found to be:

$$\Delta O^2 = \int_{log_{10}(1/i)}^{log_{10}(sf/2)} (O_{Nk} - O_N)^2 d[log_{10}(f)] \tag{4.3}$$

where O_{Nk} and O_N are the Kaimal and measured ogive respectively, both normalised by the total covariance, denoted by the subscript 'N'. i and sf are the length of the record in seconds (1800 s here) and the sample frequency (20 Hz here), respectively. The integrals are carried out numerically by the trapezoid method over all of the computed ogive from the lowest frequency ($1/i = 1/1800$ Hz) to highest ($sf/2 = 10$ Hz) frequencies.

Use of the square of the difference in Eq. 4.3 (rather than the modulus of the difference, for example), increases the dependency of the quality parameter on large spikes in the ogive. Hence an ogive with bias that is limited to a narrow frequency range is distinguished from one with a similar level of bias that is spread across the full frequency range (e.g. caused by noise across the whole spectrum). A truncated ogive, O_T is also created, for which all points below 1/120 Hz are removed. The truncated form was only used for the detection of motion correlated contamination, because parameters derived from the truncated ogive have no influence from low frequency contamination. Note the truncated ogive is not used to quantify the flux at any point. The subscript 'T' hereafter indicates that a parameter was calculated using the truncated ogive.

In 120 records, the ogive was of such poor quality that the curve fitting process failed to converge to a solution. These ogives were found to be extremely contaminated and so rejected – they would all have failed at least one of the tests outlined here if visually inspected. This left 4495 records with which to continue the analysis.

4.4   Motion contamination

4.4.1   Ship motion frequency band detection

The frequency range of ship motion was determined from the variance power spectrum of the pitch angle of the ship. Pitch is a likely ship motion parameter to

be correlated with flow distortion for bow-on flow (Brut et. al., 2005). Any pitch variance above 1/3 Hz and below 1/25 Hz was first chopped from the spectrum, because variance outside of this range was due to noise, vibration, or low frequency changes in the pitch series, rather than wave induced motion. These generous limits were chosen after examination of many records; variance outside the limits was clearly unrepresentative of wave motion, and not part of a well behaved continuous distribution (such a distribution shown in Figure 4.3.b). The frequency limits for ship motion were then defined as the frequency range containing the central 96% of the pitch spectrum (Figure 4.3.a).

Some records had very low levels of pitch variance (less than 0.05 deg^2) and a relatively low signal to noise level. In these cases the frequency limits for ship motion as determined from the central 96% of the ogive were often dragged wider than would be physically realistic for wave-induced motion (e.g.: a lower frequency limit of 1/60 Hz could be automatically defined). Therefore for records with total pitch variance below 0.05 deg^2, default frequency limits were imposed; the defaults averaged from the limits of records with pitch variance between 0.05 to 0.1 deg^2. The default limits were 1/4 Hz to 1/14 Hz when the ship was on station and 1/3 Hz to 1/18 Hz when the ship was on passage. The range is wider in the latter case since the ship can be moving in any direction relative to the direction of the waves. Of the 4495 records examined, only 99 required use of the default frequency limits.
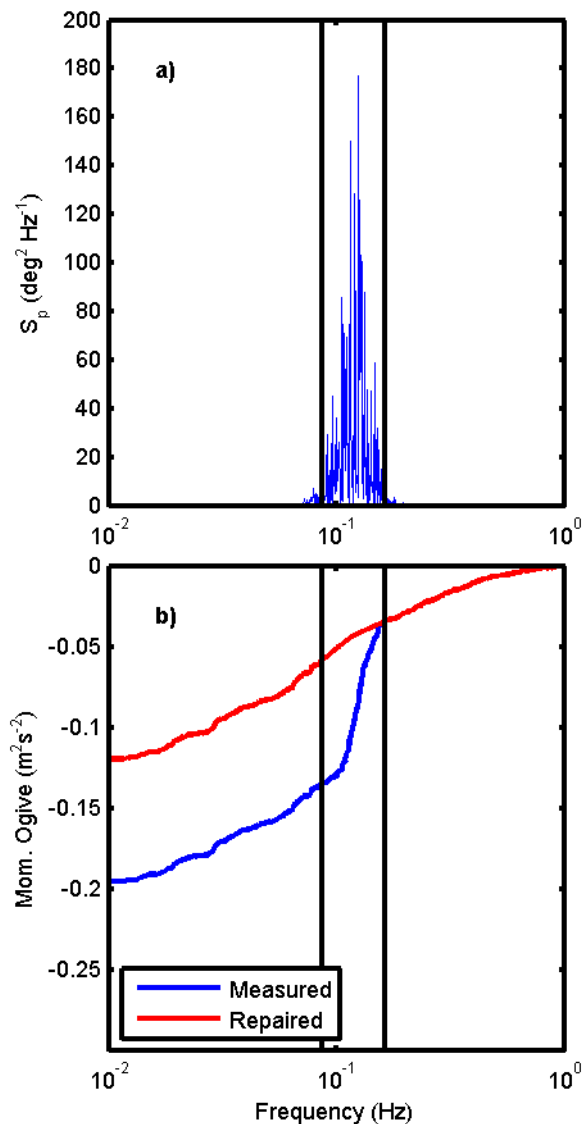
Figure 4.3 - a) Ship motion band identification using the central 96% of the pitch spectrum (S_P). b) The effect of interpolating over the perturbation in the momentum ogive using the gradient in the adjacent higher and lower frequency bands. Note the reduced frequency limits compared to full ogive plots.

4.4.2 Motion contamination and interpolation

To quantify the level of motion contamination, the ogive is interpolated across the motion frequency band, using the higher and lower adjacent parts of the ogive to establish a two part interpolation gradient (Figure 4.3.b). The measured ogive in the lower half of the motion band is replaced with a linear fit to ogive just below the motion band; the fit performed over the same frequency width as half the

motion band. Similarly, the measured ogive in the upper half of the motion band is replaced with a linear fit to the adjacent measured ogive just above the motion band. The new ogive is defined as the interpolated ogive (O_I). Kaimal form fits were then made to both the unaltered and interpolated curve, and these used to determine if motion contamination was present.

A subtle feature of Figure 4.4.b is representative of most records; most of the obvious motion-correlated contamination is toward the higher end of the frequency range, and not distributed evenly across the whole frequency range. This is physically meaningful; higher frequency motions of a given displacement range are faster than lower frequency ones. This indicates that motion-correlated flow distortion is not merely a function of the changing orientation of the ship, but is actually influenced strongly by the *motion* of the ship; i.e., the structure of the ship is pushing and pulling the flow, not merely deflecting it. This is demonstrated conclusively to be the case in chapter 5. However, at this point, the physics of motion-correlated flow distortion are not discussed; the spectral anomaly is simply removed, which is an empirical and unsatisfactory solution to be addressed in due course.

Two indicators were used to parameterise the size of the motion-induced anomaly, to allow redundancy should one indicator be inappropriate. The first indicator is the ratio of the logarithmic cospectral peak frequencies of the Kaimal fits to the truncated unaltered and motion-interpolated ogives ($log_{10}(f_{PT})/log_{10}(f_{PIT})$). The second is the ratio of the unaltered and motion-interpolated covariances (C_T / C_{IT}). 634 / 4495 records passed all the five quality control tests and, so these data were used to decide thresholds for the two indicators.

If both indicators have a value close to 1.0 for a given record then there is no significant motion anomaly. As they deviate from 1.0, then this indicates bias is present. There was a continuum of values of both indictors over the data set, and so the threshold was set empirically as follows. Figure 4.4 shows that the distributions of the two indicators are asymmetrical about 1.0, indicating that motion contamination predominantly contributes to the flux in the downward direction. The mean of the distribution of each indicator are shown to progress

from unity as the acceptance threshold for each indicator is relaxed. For example, if a very strict threshold was set for the indicator C_T / C_{IT}, of 1 ±0.01, this means that the value of C_T / C_{IT} for a given record may only deviate by 1% from unity to be accepted as 'not motion contaminated'. The result is a mean of (C_T / C_{IT}) of unity, but a mere 9 records would be accepted this way. Allowing the C_T / C_{IT} to take values of 1 ±0.09 leads to a mean of C_T / C_{IT} of 1.04, and still only accepts just 102 records. A threshold as high as 0.2, for which records very clearly have motion contamination, still allows only 220 records, and leads mean bias in C_T / C_{IT} of 1.09. It is clear that motion contamination is prevalent, and a significant fraction of most records. The 57 records that would be accepted by allowing the two indicators to take values of 1±0.05 are named here as the uncontaminated data set.
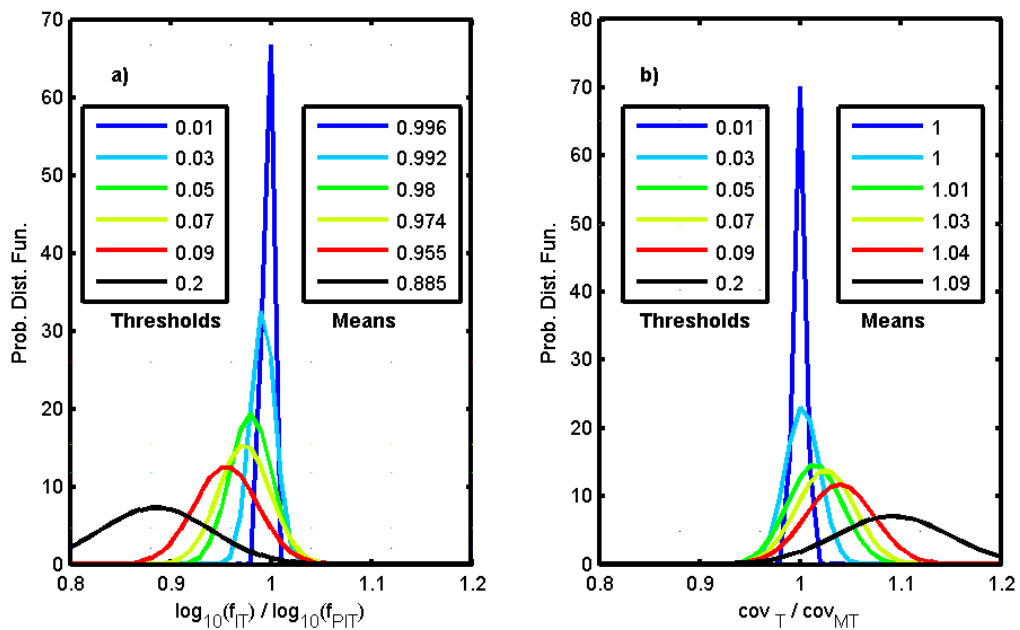
Figure 4.4 -How the distributions of the two indicators of motion contamination vary, as accepted deviations from unity are relaxed. The parameters are (a) **the ratio of the (logarithmic) cospectral peak frequencies, and** (b) **the ratio of the covariances. Both parameters use the truncated ogive to remove low frequency contributions. Note the progression of the mean of both distributions from unity as thresholds are relaxed. 'Thresholds' indicates the permitted positive and negative deviation of the parameter from unity, and 'Means' the mean of the parameter within the data restricted to be within the threshold value from one**

However, these records were found to be toward the lower wind speeds and smaller ship motions in the data set. In order to use the higher wind and sea data, interpolation is essential. Therefore to ensure consistency, interpolation was applied equally to all records.
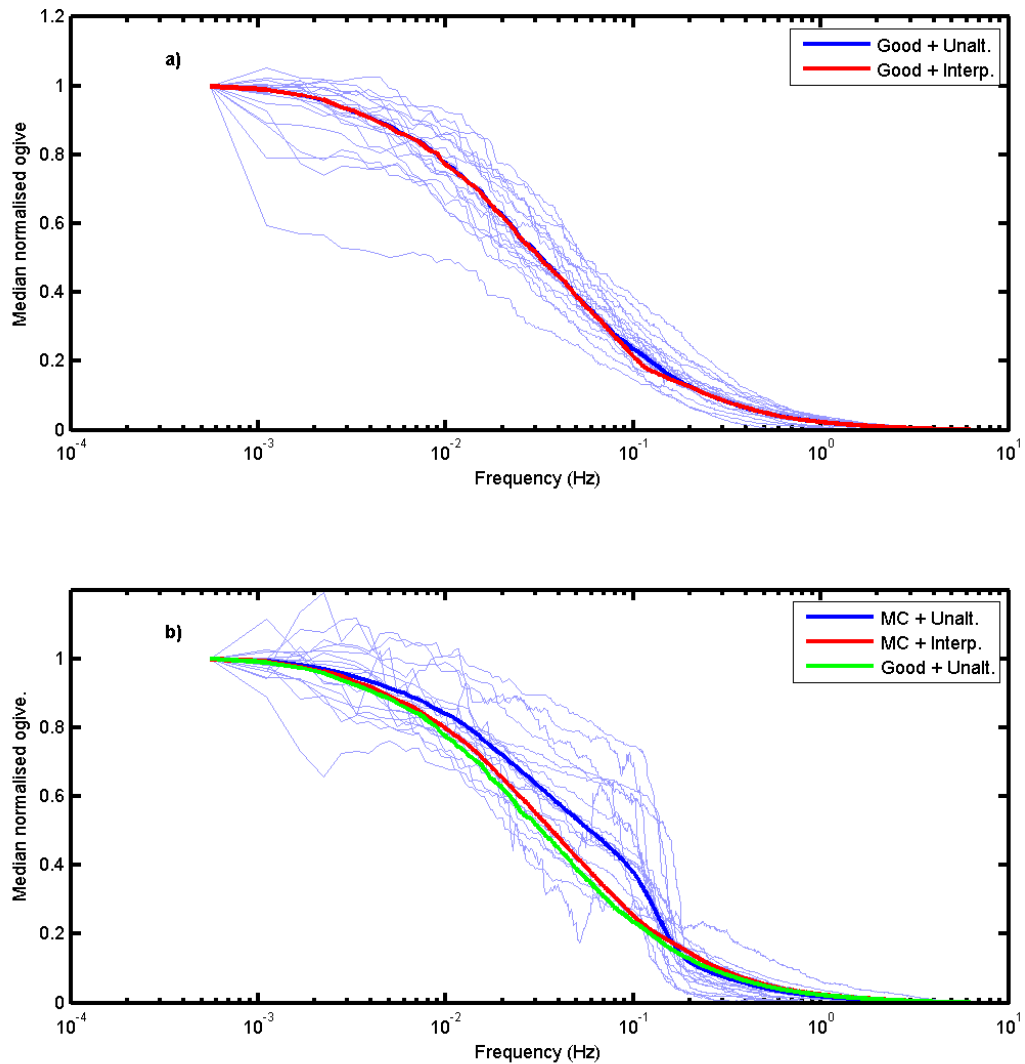
Figure 4.5 – Median ogives of all 634 data, split into a) **57 with no motion contamination (good), and** b) **the remaining 577 with motion contamination (MC). 20 randomly selected individual ogives from each category are also plotted in grey. Blue indicates unaltered, and red indicates interpolated. The green line in** b) **is the unaltered blue line from plot** a) **for comparison**

Figure 4.5 shows median ogives for the uncontaminated 57 records and the rest of the contaminated data; each ogive normalised by its total covariance. For the 57 uncontaminated data, interpolation has almost no effect on the median shape.

Interpolation of the contaminated data results in a similar median ogive to the uncontaminated median ogive, giving some confidence in the validity of using interpolated ogives to evaluate the flux.

4.5 High frequency contamination

A significant minority of WAGES ogives did not converge to a near-zero gradient at the high frequency limit. A representative example is shown in Figure 4.6, where the cospectrum shows a significant and un-physical deviation from the expected -2/3 gradient.

The lack of high frequency convergence prevents a fit being found to the Kaimal ogive form hence the algorithm cannot yield further parameters. To resolve the issue, all measured ogives are initially modified to force convergence so that a Kaimal fit can be made and the level of high-frequency contamination quantified for every sample period. 796 records passed all tests except the high frequency contamination test.

The high frequency contamination is added back on to the flux after the other tests are completed. This is done because one of the possible causes of contamination is aliasing; the presence of high frequency aliasing does not affect the total covariance for a given record, and so any flux artificially removed should be reintroduced to avoid inducing bias.

The ogives were forced to converge above a high frequency threshold (f_{HX}), that was selected by examining the gradient of the ogive at frequencies above 1/3 Hz (i.e. above frequencies affected by ship motion). The midpoint frequency of the bin with the smallest gradient is selected as the high convergence frequency, and the ogive is then artificially flattened at higher frequencies. The lost fraction of the covariance (C_{HX}) above f_{HX} is recorded. This lost fraction is negligible for most ogives because they converge toward high frequencies.
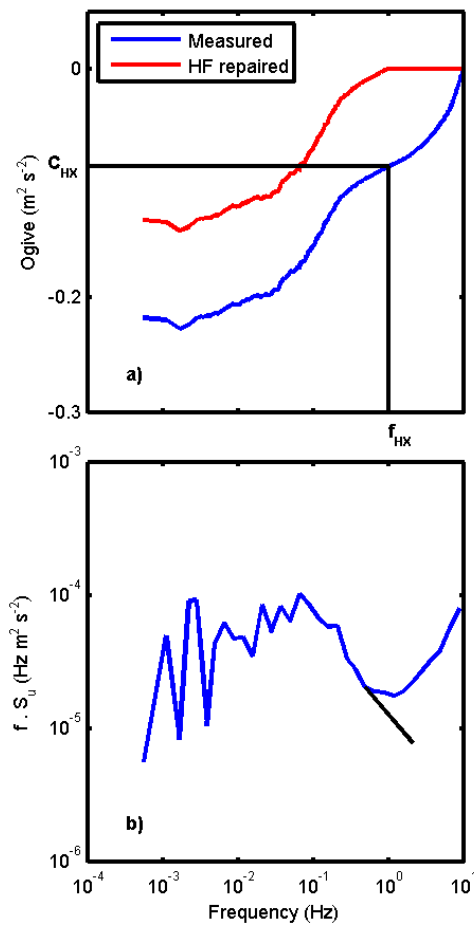
Figure 4.6 – a) **How an ogive is modified to force convergence at high frequencies in order to proceed with further quality control. The frequency of smallest ogive gradient (f_{HX}) and the covariance removed (C_{HX}) are shown. Note that C_{HX} is reintroduced at the end of the algorithm – this is not a flux correction.** b) **The frequency weighted streamline wind spectrum, binned into 8 bins per frequency decade, and the expected -2/3 gradient (black) line in the inertial subrange**

Data with high frequency contamination were then considered for rejection or acceptance. The majority of data had $|C_{HX} / C_I|$ less than 0.01. Data was split into those with and those without high frequency contamination, by using a threshold of $|C_{HX} / C_I| = 1.01$, which accepted 630/ 769 uncontaminated records; use of a threshold of 1.02 accepted 638 records. The distribution of C_{HX} / C_I in the contaminated data is unpredictable; C_{HX} / C_I ranges as high as 1, very probably caused by instrumental failure rather than aliasing, because aliasing would mean that even the low frequency eddies were passing the sensor at tens of Hz. Even the highest relative wind speeds of 30 m s^{-1} could not cause such large aliasing

effects. As a brief test, the median value of C_I / C_{COARE} was calculated; C_{COARE} being the output momentum flux from COARE 3.0; done for both the uncontaminated and contaminated data set. The uncontaminated set had a median C_I / C_{COARE} of 1.02, whereas the contaminated set had a median C_I / C_{COARE} of 2.1. This is further evidence that high frequency contamination is not likely to be solely caused by aliasing; such large disagreement with COARE should not be observed for realistic flux records. The cause could not be deduced from the data; the issue is left unresolved. For the purpose of obtaining an unbiased set of flux data, the high frequency contaminated records are therefore rejected.

4.6 Cospectral peak frequency rejection

The cospectral peak frequency of the cospectrum derived from the Kaimal fit to the interpolated ogive is denoted f_{PI} and varies from one record to another. Problems can be encountered if f_{PI} lies towards the high or low frequency limits. If f_{PI} is high enough to lie within the range of ship motion contamination then interpolating across the motion-frequency range effectively cuts off the peak of the cospectrum and a significant fraction of the real covariance is lost. It may be possible to adapt the interpolation method to account for this, although any attempt to re-create the lost peak would require a perfect Kaimal form, which itself depends on having perfect knowledge of the flux. For this reason it is preferable to reject records that had f_{PI} within the motion range of frequencies.

As f_{PI} tends towards lower frequencies, a larger fraction of the turbulent covariance is contained within the poorly-sampled low frequency part of the spectrum. At the extreme, if f_{PI} is low enough then it becomes ambiguous whether or not the ogive has converged. Use of a longer averaging period would be suitable to solve this problem for studies with typically longer period turbulence scales, but for the moderate to high wind speed WAGES data, 30 minutes is almost always adequate.

Figure 4.7-a shows a linear fit to the 841 interpolated CD_{N10} vs. U_{N10} values that passed all tests except for the cospectral peak restrictions. Figure 4.7-b shows the anomaly from the linear fit of each data point, as a function of f_{PI}, so describes how the drag coefficient is biased as a function of f_{PI}. The upper threshold can

clearly be identified as 0.07 Hz. Above 0.07 Hz the drag coefficients have a consistent low bias due to the loss of covariance caused by interpolating across the cospectral peak. This rejected 193 / 841 records.
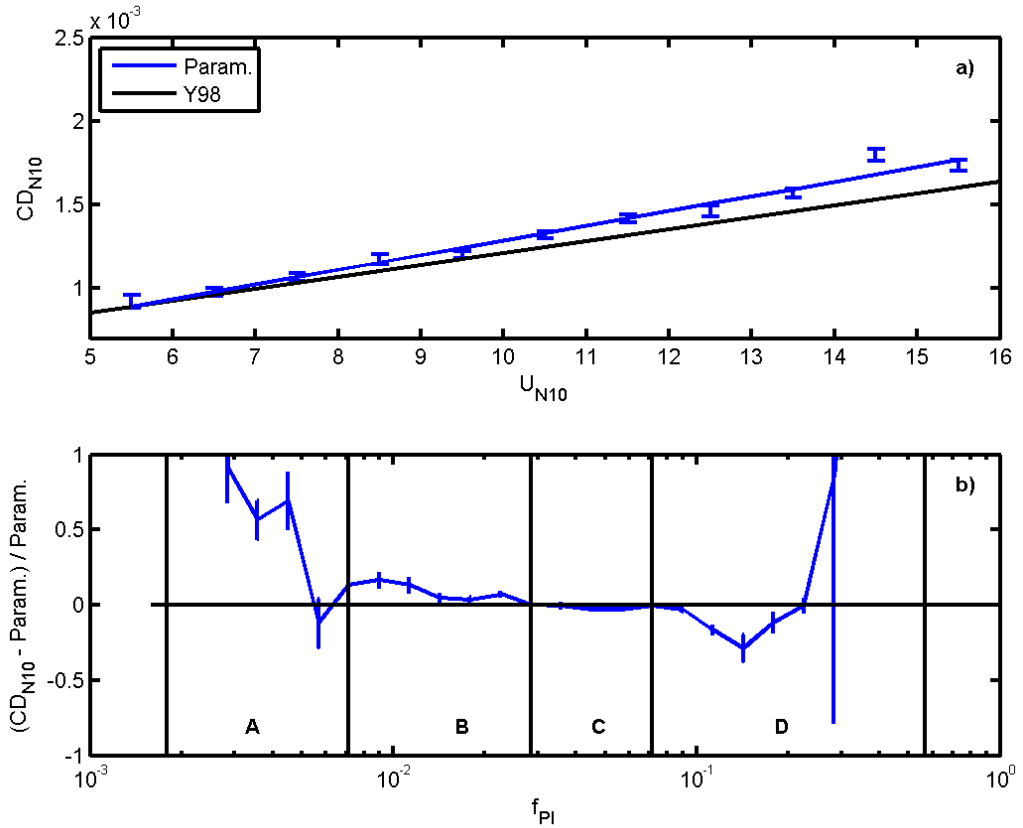
Figure 4.7 - a) **10m neutral drag coefficient (CD$_{N10}$) parameterisations derived using motion interpolated data, restricted to ±10 degrees of bow-on relative wind directions. The parameterisation of Yelland et. al. (1998) is provided for reference.** b) **The influence of the cospectral peak of the interpolated ogives on the deviation of individual data from the parameterisation line in panel a). Bin averages are taken using the central 95% of ranked data only to remove outliers**

At low frequency values of f_{PI}, the bias cause is different; the ogives found to be consistently contaminated at low frequencies. It is unlikely that the cause is a lack of convergence of turbulence; the bias would be low if this was the case. Therefore a low value of f_{PI} is indicates contamination from mesoscale effects or measurement bias (such as the ship changing heading during a record).

Setting the low frequency threshold on f_{PI} is somewhat subjective; A strict limit of 0.03 Hz (accepting the range of values within only 'C' in Fig. 4-8-b) left zero bias in the drag coefficients but rejected 264 / 841 records. A more lenient limit of

0.007 Hz (accepting the range of values within both 'C' and 'B' in Fig. 4-8-b) results in a high bias of 5.0% within that data, but rejected only 20 records. The more lenient limit of 0.007 Hz was chosen after visual inspection of example ogives with f_{PI} between 0.007 Hz and 0.03 Hz, found to be close to converge in the majority of cases.

Since the peak frequency varies with atmospheric stability (e.g. Kaimal et al., 1972) applying the f_{PI} thresholds limits the range of atmospheric stability conditions that will be represented in the final quality-controlled data set. For the WAGES dataset, the f_{PI} restrictions described result in a new stability distribution, with mean z/L of -0.039 (instead of 0.001 for data prior to frequency restriction), a std. dev. of 0.25 (instead of 0.59 for the unrestricted set), and skewness of -0.53 (-0.03 for the unrestricted set). The rejection is skewed almost entirely toward removal of stable records.

This is a serious limitation of the interpolation technique – in order to use it with confidence, a significant fraction of stable records must be rejected. This means that the final set from which flux averages are computed does not represent average open ocean conditions. However the motion contamination must be removed in order to have any confidence in EC results. The whole of the subsequent chapter is devoted to a more robust method of removing motion contamination that removes the need to reject stable cases; at this point discussion continues to further tests.

4.7   Relative wind direction restrictions

Several studies (e.g. Dupuis et. al., 2003, Yelland et. al., 2002, Brut et. al., 2005) have found that CD_{N10} has a strong dependence on the wind direction relative to the ship. A modelled correction for bow-on mean flow distortion was applied, but was only valid out to about ±10 degrees from bow-on. It is possible that turbulent flow distortion varies with wind direction. This means that bias in the drag coefficient related to the relative wind direction could be due to a combination of these effects.

Figure 4-9 drew on 1951 records that passed all ogive tests, but were not restricted to relative wind directions within ±10 of bow-on. The interpolated, unaltered, and the inertial dissipation fluxes are presented.
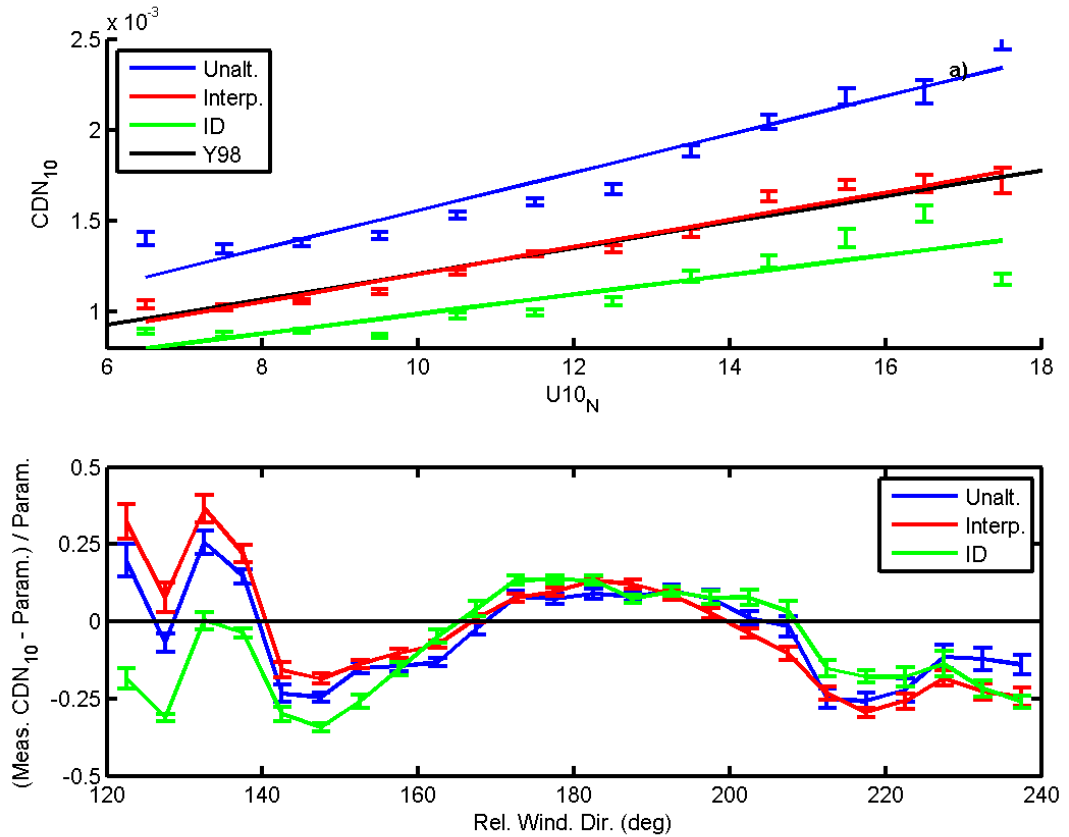
Figure 4.8 - a) **Drag coefficient parameterisations derived using unaltered ogives (blue), interpolated ogives (red), and the inertial dissipation fluxes (green). The parameterisation of Yelland et. al. (1998) is provided for reference.** b) **The influence of relative wind direction (180 degrees is bow on, 270 degrees is starboard on) on the anomaly of individual data from the relevant parameterisation for the 3 data sets.**

A mean U_{10N} vs. CD_{N10} relationship is obtained for each flux type (Fig. 4-9-a), and the anomaly of individual data from their respective parameterisation are shown as a function relative wind direction in Fig. 4-9-b.

Several conclusions can be made. The effect of the relative wind direction on each anomaly set is very similar. This suggests that the bias in the drag coefficient from relative wind direction is mostly from bias in the U_{N10} term caused by mean flow distortion. If the flux bias was significant compared to the than the U_{N10} bias, then the three anomaly plots would be show more variability

because the relative wind direction should affect the interpolated fluxes, the unaltered fluxes, and the ID fluxes differently. The ID is known to be more sensitive to mean flow distortion (Yelland et al, 1998), which explains why the anomaly dependence is different than for the EC types.

The interpolated anomaly shows a slightly better constrained relation to the relative wind direction than the unaltered fluxes. This suggests that interpolation is effective at removing flow distortion bias in EC flux measurements, although the effect is largely masked by the fact that both drag coefficient types are biased similarly by error in U_{N10}.

For flows within about ±30 degrees of bow-on, the anomalies vary between roughly -20% and + 10%. Winds from about 50 degrees to port of the bow result in much larger anomalies, probably due to flow distortion about the foremast and navigation lights mounted on it. The use of the ±60 degree range of wind directions has fortuitously led to the various positive and negative biases cancelling out, and hence to the nearly perfect agreement of the interpolated fluxes with Y98; highlighting the need for a direction specific flow distortion correction to use ship-board data to develop flux parameterisations.

Further evidence of the effectiveness of interpolation is shown in Figure 4-10, which shows the effect of pitch variance on the anomalies of the interpolated and unaltered drag coefficients. These 634 data have been restricted to be within ±10 degrees of bow-on and pass all four ogive quality tests. The pitch variance dependence of the drag coefficient is clearly removed by interpolation.
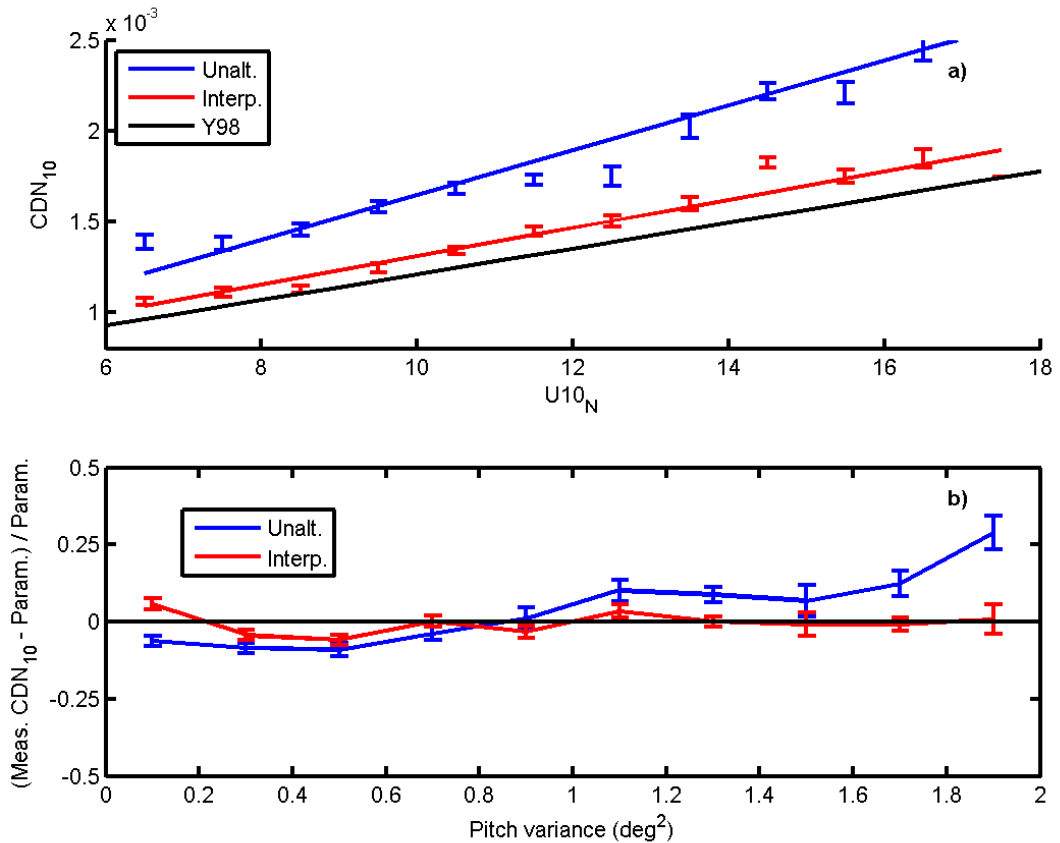
Figure 4.9 -a) **Drag coefficient parameterisations derived using unaltered ogives (blue), and interpolated ogives (red). The parameterisation of Yelland et. al. (1998) is provided for reference.** b) **The anomalies of each data from their respective parameterisation as a function of the pitch variance.**

4.8 General quality test

There are a minority of records that pass the relative wind, cospectral peak frequency, and high frequency tests; however even after interpolation they are still not a good match to the Kaimal curve. These records are detected using the general ogive quality parameter (ΔO^2) defined in Eq. 4.3. Most fail this test had contamination at low frequencies, but the test also identified records where other causes for rejection were apparent. For example if there was a sharp step in the motion pack series for a records, perhaps an electronic fault, then the ogive is often badly formed over the frequencies used by the filtering during motion correction (between 1 and 2 minute period). This test was regarded as a 'safety

net' to identify records that passed the other tests but were inappropriate for inclusion in the final data set.

Of the 735 records that passed the other three tests, almost all were good matches to the Kaimal form after interpolation, and this was used to set the acceptance threshold for ΔO^2. The vast majority of the 735 data had ΔO^2 below 0.02; above 0.02 there was a large range of values that parameterised a wide variety of ogives, from those with a low frequency spike, to those that were junk quality. No clear relationship of ΔO^2 with mean factors such as wind speed or direction could be observed. 634 data passed this, and therefore all tests. They are considered to be the best available momentum flux data from the WAGES dataset. Figure 4.10shows each of the 634 ogives in the quality controlled data set, each normalised by the interpolated covariance, and their mean. The individual forms show a well-defined range of deviations from the mean. There is no frequency dependent anomaly in the mean ogive, and there is also convergence in the mean at high and low frequencies; meaning that no discernible bias in flux averages is present after quality control.
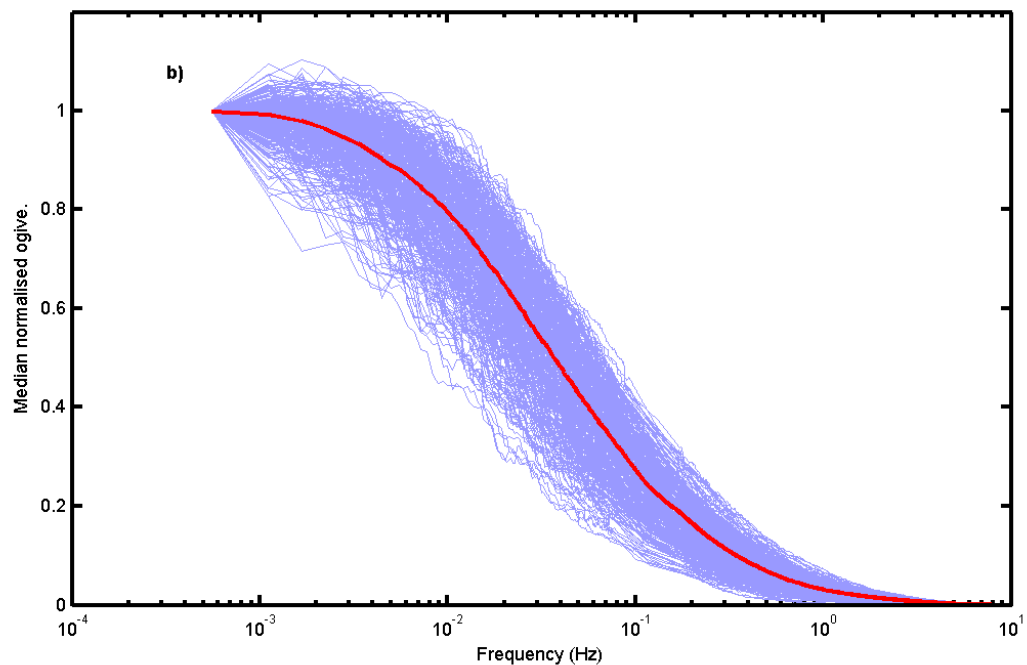
Figure 4.10 - Mean ogive curve of the final quality controlled 634 data. All individual ogives are also plotted in grey, normalised by each interpolated covariance value.

4.9   Results

Figure 4.11 shows how the linear fits of CD_{N10} against U_{N10} are affected by sequential and accumulative applications of each quality control stage. Figure 4.11.a incorporates all the 4495 records that passed basic quality control and shows the effect of interpolation to be significant. The unaltered and interpolated linear fits to the bin averaged values both have similar R^2 values of 0.85 and 0.82 respectively - whilst it would not be expected for the fit to the interpolated ogive to have less confidence, both fits have serious contamination from other sources at this point. The unaltered linear fit is biased high by 69% at 10 m s^{-1} with respect to Y98, and the interpolated fit high by 30%.

Further improvement is made by restricting the relative wind direction from ±60 to ±10 degrees (4495 to 1264 records) from bow-on. R^2 is still similar (0.84), but the mean bias at 10 m s^{-1} has dropped from 30% to 23%. Inclusion of the high frequency test (1264 to 1010 records) improves R^2 to 0.96, and reduces the mean bias to 6%. The final two tests, for the cospectral peak frequency and general quality test (shown combined because each had a relatively minor effect compared to the other three) were applied (1010 to 634 records); R^2 improves to 0.98, but increases mean bias to 10%. That the last two tests increase bias from Y98 is of concern; however this can be interpreted as the two tests bringing the linear fit closer to the parameterisation used by COARE 3.0 (which is about 10% higher than Y98 over moderate wind speeds). A fit to the rejected data (green; Figure 4.11.d) matches Yelland et al. (1998) near perfectly. However the level of scatter is far larger and so this outcome is almost certainly a coincidental sum of all the positive and negative biases.
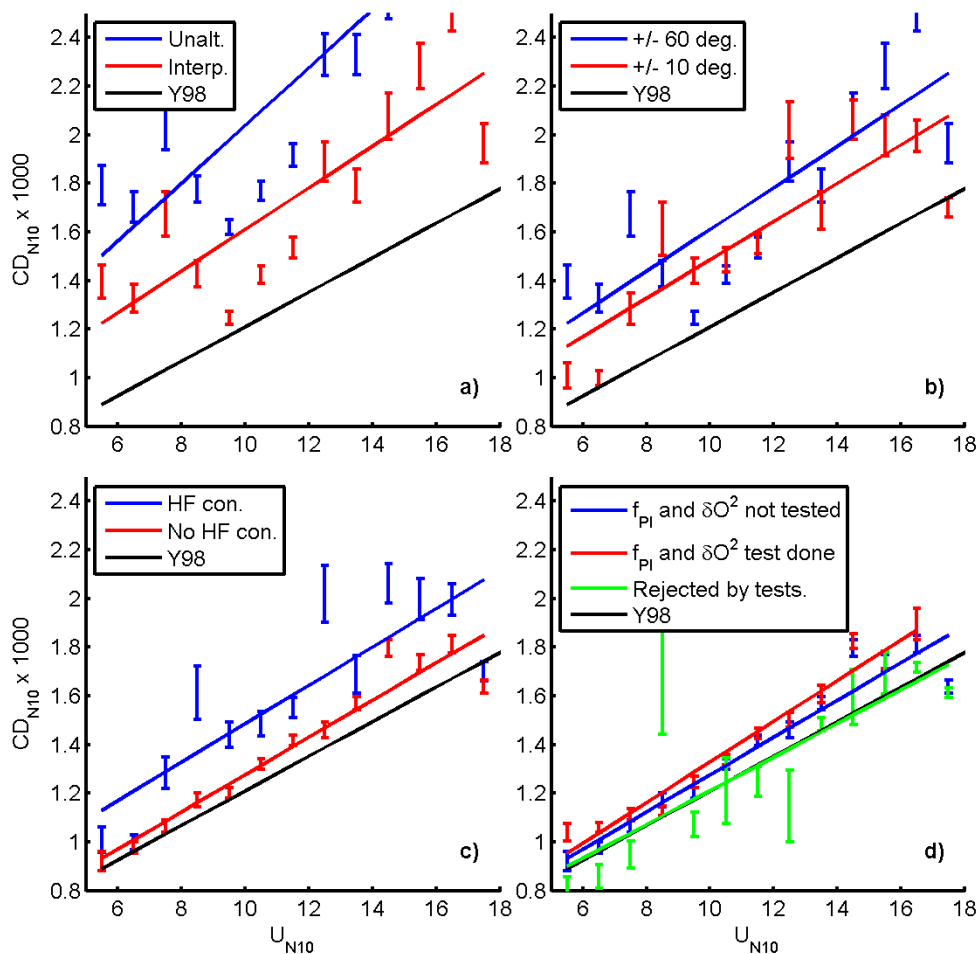
Figure 4.11 - The effect of individual quality control steps on CD_{N10} vs. U_{N10} parameterisations. a) Unaltered vs. interpolated, all 4495 data. b) Relative wind directions of ±60 deg. (4495) and +/- 10 degrees (1264). c) Including (1264) and rejecting (1010) high frequency contamination. d) The combined effect of the cospectral peak, and quality parameter quality controls. The blue line is derived from 1010 data, the quality controlled red line derived from 634 data. In this panel a line derived from the rejected data (372) is also shown

Figure 4.12 below shows far greater agreement between the quality controlled EC fluxes and the ID and COARE results. Note that for comparison purposes, the y-axis of Figure 4.12 has a much smaller range than Figure 3.18, which is a similar plot produced pre-quality control and interpolation.
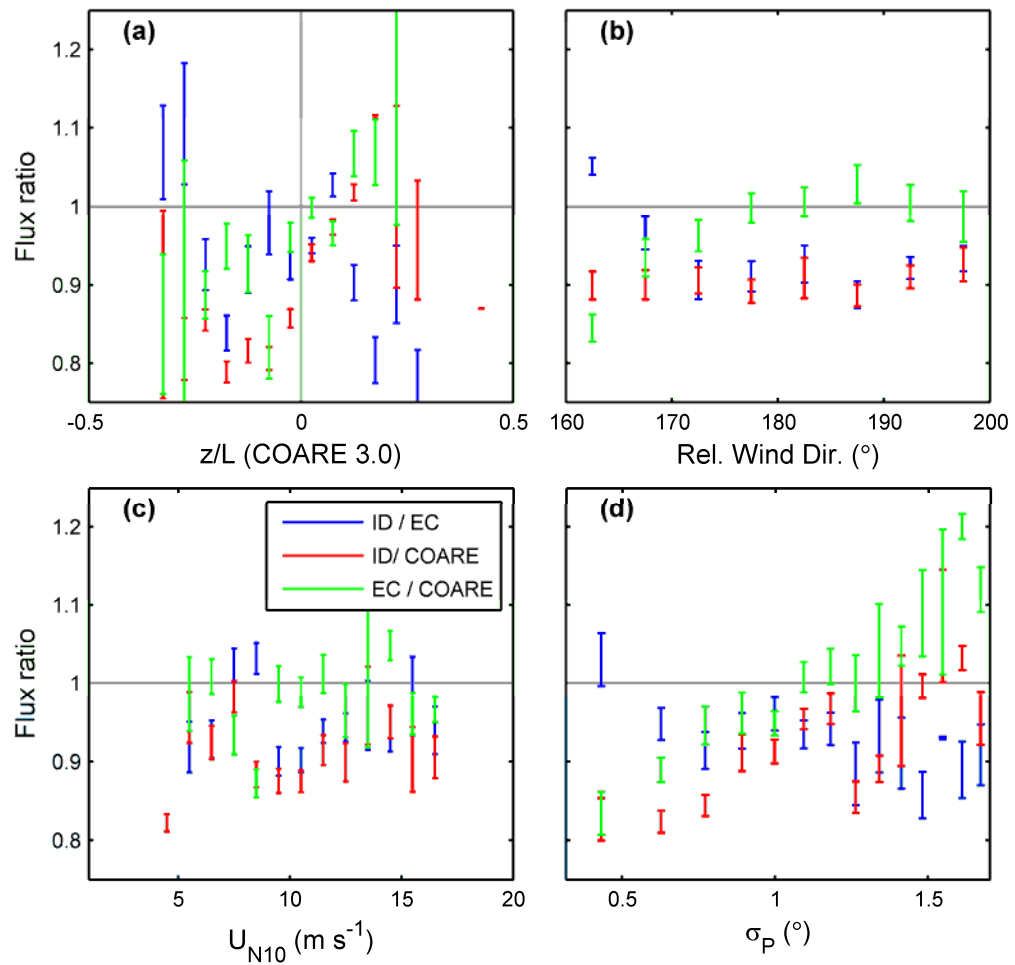
Figure 4.12 – Similar figure to Fig. 3.18, except all spectral quality control and motion interpolation have been performed. Ratio of EC, ID and COARE fluxes as a function of: a) COARE stability output; b) relative wind direction; c) ten metre wind speed; d) standard deviation of pitch.

There is no clear bias correlated to stability or the ten metre wind speed. When the wind is from port, distortion of the mean flow likely causes bias in the COARE and ID fluxes, further evidence that the relative wind direction must be restricted to within just ±10 degrees of the modelled flow distortion corrections. Some dependence of the EC/ COARE ratio and ID / COARE ratio on the standard deviation of pitch is evident. This may be caused by using a single mean flow distortion correction rather than one that has some pitch dependence; Brut et al. (2005) demonstrate that mean flow corrections for a range of pitch angle are not symmetrical about a pitch of zero. Therefore the positive and negative biases

of the mean flow speed do not cancel out over a record. However, by comparing the present figure to Fig. 3.18, it is clear that the quality control and corrections of this chapter vastly improve the EC results; to the point where they may be considered and discussed rather than simply rejected.

Figure 4.13 shows the interpolated data set with all tests (634 records) with additional comparisons from the literature. Note that the ID fluxes have an additional restriction that the ship was not steaming ahead. The fully quality controlled results lie within the range of all these curves, although only the COARE results are higher than our own. Our results are biased 10% high at 10 ms^{-1} with respect to Y98 and approximately equal to COARE 3.0. A linear fit is avoided here, given the curvature of the points around 8.5 m s^{-1}; this would be consistent with the recent results of Edson et al (2013), who identify a transition from rough to smooth flow from 8.5 to 4 m s^{-1}. We may therefore consider our results to be particularly high across the range of parameterisations, but within the accepted realistic range.
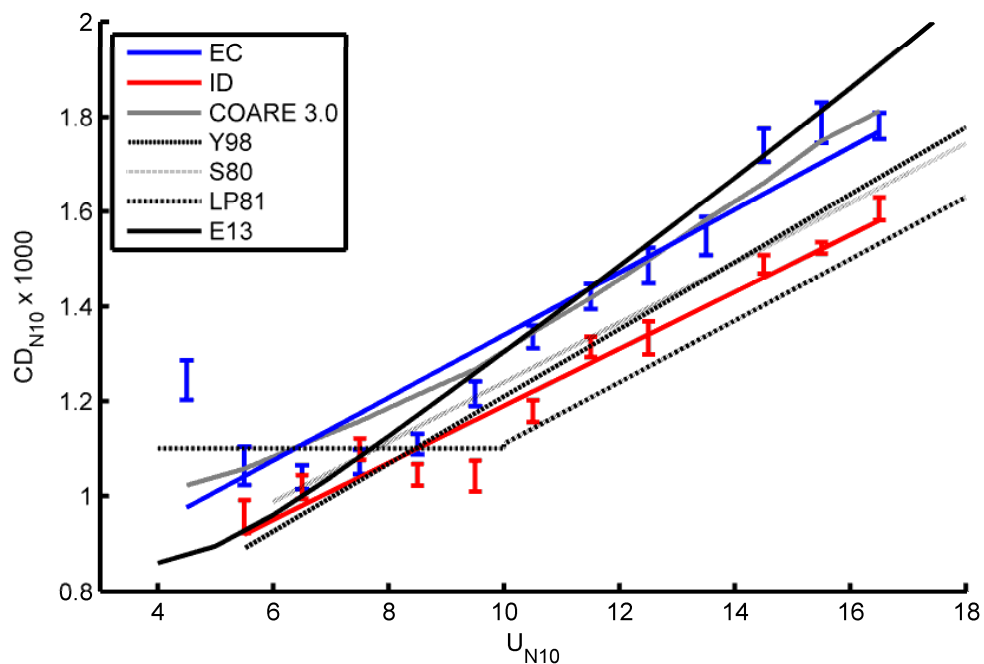
Figure 4.13 - CD$_{N10}$ vs. U$_{N10}$ parameterisation linear fit derived from the data with all quality control (634 data). Also plotted are the results of the COARE 3.0 algorithm, and the parameterisations of Yelland et al. (1998), Smith (1980), Large and Pond (1981), and Edson et. al (2013).

4.10 Summary

Spectral quality control and carefully justified restrictions in relative wind direction, when applied to a very large set of ship based EC measurements of the air-sea momentum flux, significantly improves the agreements between WAGES results and other parameterisations. Prior to quality control the EC results were simply not useful, in line with findings of Edson et al (1998) and Pedreros et al (2003); that ship board EC momentum flux results are biased from flow distortion and platform motion.

Whilst large improvements have been made using the spectral tests, the reliance on interpolation of the ogive to correct for motion contamination is not satisfactory. It is not theoretically justifiable, and enforces preferential rejection of stable cases. This is particularly important if the quality control tests are to be used to examine the WAGES scalar transfer coefficients; these have been demonstrated to have a strong stability dependence (e.g. Large and Pond, 1982; Pedreros et. al., 2003, Smith 1980). A more robust method of correcting for motion contamination is developed over the next chapter.

At this point in the investigation, the WAGES EC results agree more with the higher parameterisations of COARE 3.0 and Edson et al., 2013, than with Smith (1980) or Yelland et al. (1998). Whilst interpolation has been demonstrated to be effective at removing motion correlated flow distortion, there is a possibility that it also removes any upward flux contribution caused by swell, which if not removed might possibly bring the WAGES results into agreement with Smith and Yelland et al. There is also the possibility that flow distortion is not restricted to motion frequencies; only a direct reference measurement from a flux tower could resolve this issue.

5   Motion correlated flow distortion

It was demonstrated in the previous chapter that an anomaly within the range of ship motion frequencies is consistently found in most WAGES momentum flux cospectra. The anomaly is present even after standard correction (Edson et al., 1998) of the measured wind components using the motion sensor, so it is referred to hereafter as the residual motion anomaly/contamination. In the previous chapter, the residual anomaly was removed by interpolating the momentum ogive over ship motion frequencies. Interpolation was shown to reduce the momentum flux by $20 \pm 15\%$. The drag coefficients calculated from interpolated ogives were in better agreement with other CD_{N10} vs. U_{N10} parameterisations (Yelland et al., 1998; Smith, 1980; Large and Pond, 1981; Fairall et al., 2003), compared to the results from unaltered ogives.

Interpolation is limited in its usefulness for at least four reasons. First, it is a purely empirical solution that yields no insights into the causes of the motion-correlated anomaly. For example the cause of the anomaly may be movement of the sensor in a vertical gradient of the measured field, attitude dependent flow distortion, or bias correlated to physical forces acting on the sensors (such as the effect of rotation on any moving parts, or flexion of the sensor). Second, interpolation becomes more uncertain as noise in the ogive increases, which is related to the magnitude of the flux and the capability of sensors. Third (Figure 5.1), the results of interpolation may be biased low if the true peak in the cospectrum lies within the ship motion frequency range. This leads to a systematic low bias of the interpolated flux at higher relative wind speeds, and at more positive stabilities, since both factors shift the turbulence peak to higher frequencies (Kaimal et al., 1972). Fourth, interpolation removes a potential true wave-correlated flux contribution that may be induced during low-wind and swell-dominated conditions, meaning ships are of limited use for such studies if interpolation is used.

This chapter describes the development of a more sophisticated and defensible motion contamination correction technique. The weaknesses of interpolation are avoided, and some new qualitative insights into the physics of time-varying flow distortion are discussed. The novel method is shown to match the results of

interpolation near perfectly for bow-on winds; with the exception of records during which rolling motions are high and the physical problem becomes too complex to solve.
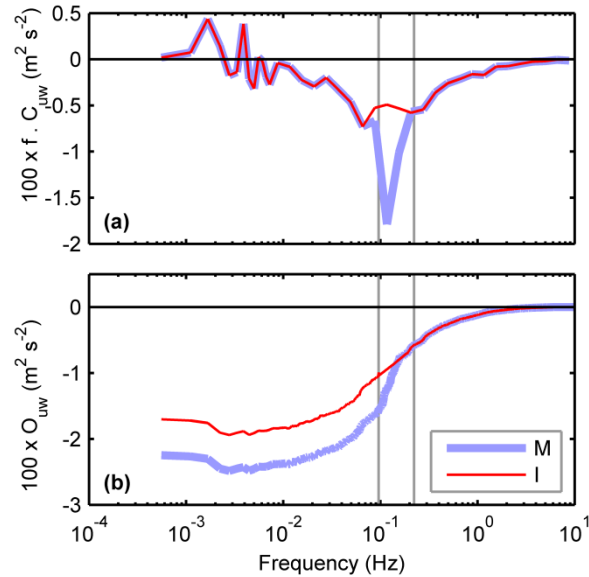
Figure 5.1 – The a) frequency weighted cospectrum and b) ogive, of the momentum flux during an example record for which interpolation of the ogive over the motion frequency range is not satisfactory. 'M' is the unaltered flux, and 'I' has been interpolated over the motion frequency range

5.1 Tilt correction method – conceptual introduction

5.1.1 Wind and motion correlations

Consider a hypothetical case: A single turbulence record is measured when the mean wind is moderate and bow-on, and wave induced ship motion is significant. The ship and sensors have no mass, allowing air flow to pass completely undisturbed. There would certainly not be any correlation between the turbulent wind perturbations and ship motion *caused by* flow distortion for this hypothetical case, because there is no flow distortion at all. However, there is potential for *coincidental* correlation between the motion and turbulent series; this for turbulent fluctuations that have frequencies similar to those of motion.

It is possible to demonstrate theoretically that for a half hour record, such coincidental correlation is negligible. The coincidental correlation should tend

toward zero as the sampling time of the record increases, providing that turbulent eddies with frequencies similar to ship motion have a random probability of any possible phase difference with respect to the motion. Motion periods are typically between 5 and 15 seconds, and so upper and lower limits of 360 and 120 motion cycles per half hour may be expected. The time series can thus be segmented into 120 fifteen second sub-series, and the correlation coefficient between ship motion and the wind (R^2 (*wind,motion*)) calculated for each; note that Pearson's product moment correlations between *A* and *B* are denoted R^2 (*A,B*).

If the distribution of the 120 R^2 (*wind,motion*) values is normal, with a mean of 0 and a standard deviation of 0.34, then the standard error of the mean of R^2 (*wind,motion*) for a half hour sample would be 0.34 / √120 = 0.03. If the distribution of R^2 (*wind,motion*) is uniform (a 'top hat' distribution with limits of -1 and 1), then the standard deviation is equal to 2 / √12, and the standard error of the mean is 0.05. Whichever of the normal or top hat distributions is better representative; there are enough motion cycles per half hour to average out almost all coincidental correlation between motion and tilt for any given record. There may be coincidental correlations up to 0.05 for a given record; this value can be thought of as a limit below which R^2 (*wind,motion*) is not due to flow distortion, but simply an artefact of using a limited sampling time. R^2 (*wind,motion*) values above 0.05 for a half hour record are thus almost certainly caused by systematic measurement bias that is correlated to motion.

Such measurement bias is likely to be caused by flow distortion. The alterations to turbulent flow caused by a moving and bulky obstacle are likely to be extremely complex; there are no published results as yet. A semi-empirical investigation approach is attempted in this section; by examining *which* motion parameters are best correlated with the wind. By assessing how R^2 (*wind,motion*) varies with conditions, conclusions can be made of the physics of motion correlated flow distortion. The wind series are then altered to remove motion correlations, in order to correct for the motion anomaly in the cospectra. The problem is demonstrated to be complex, requiring corrections for multiple motion modes. Motion modes are often inter-correlated, so aliased correlations between

the wind and motion types affect the interpretation of the physics, and the technical application of the correction procedure.

5.1.2 High frequency tilt definition

The double rotation method (e.g., Aubinet et. al., 2010) is commonly used by practitioners of eddy covariance to transform the earth-frame wind components into a streamline frame of reference. The time series of the three orthogonal earth frame wind components, after motion correction, are defined (all in m s^{-1}) as u_E, v_E, and w_E: positive to the east, to the north, and upward, respectively. The two mean horizontal components are used to define the first rotation, in the horizontal plane

$$\theta_M = tan^{-1}\left(\frac{\overline{v_E}}{\overline{u_E}}\right) \tag{5.1}$$

$$u_H = u_E.\cos(\theta_M) + v_E.\sin(\theta_M) \tag{5.2}$$

$$v_H = -u_E.\sin(\theta_M) + v_E.\cos(\theta_M) \tag{5.3}$$

where θ_M is the angle (radians) between the mean true east and mean streamline wind directions, positive anticlockwise. Subscript 'M' indicates that the mean wind components have been used to calculate the angle. u_H and v_H are the streamline and cross-stream wind components, positive in the wind direction, and at 90 degrees anti-clockwise, respectively. The subscript 'H' indicates horizontal streamline coordinates (to be distinguished from tilted streamline coordinates, see below). The mean of u_H is the mean horizontal wind speed (prior to application of the second rotation), and the mean of v_H is zero. At this point, the Yelland correction (section 3.3.5) to the vertical wind is applied. The justification for, and details of this correction are not repeated here; it is defined as

$$w_H = w_E - [\overline{w_E}.(1 - \beta)] \tag{5.4}$$

where β is the true mean streamline horizontal wind speed divided by the relative mean streamline horizontal wind speed.

The second rotation is in the plane of the horizontal streamline and the true vertical directions, and rotates the horizontal streamline wind components into tilted streamline wind coordinates:

$$\gamma_M = tan^{-1}\left(\frac{\overline{w_H}}{\overline{u_H}}\right) \tag{5.5}$$

$$u_{SM} = u_H.\cos(\gamma_M) + w_H.\sin(\gamma_M) \tag{5.6}$$

$$w_{SM} = -u_H\sin(\gamma_M) + w_H.\cos(\gamma_M) \tag{5.7}$$

where γ_M is the angle (radians) between the mean horizontal streamline and mean tilted streamline wind components; positive upward from the horizontal plane. Subscript '*SM*' indicates tilted streamline coordinates, derived using one mean tilt rotation. The kinematic momentum flux, is then defined by the time averaged product of the turbulent parts of w_{SM} and u_{SM}

$$C_M = \overline{u_{SM}\ w_{SM}} \tag{5.8}$$

where C_M is the kinematic momentum flux in units of m^2 s^{-2}. The flux calculated in this way typically has a residual anomaly in the cospectrum at motion frequencies.

The above is all standard methodology, and was applied to derive the streamline wind components used to compute the fluxes discussed in previous chapters. What follows is all non-standard and unpublished. Alternatively to use of a single mean tilt rotation, a high frequency tilt series (γ_F) can be computed using the turbulent wind components w_H' and u_H':

$$\gamma_F = tan^{-1}\left(\frac{w_H}{u_H}\right) \tag{5.9}$$

Nothing can be learnt from directly substituting γ_F into Eqs. 5.6 and 5.7 to perform the tilt rotation and compute the flux; if that was done then every turbulent perturbation of the tilted vertical wind speed (w_{SM}') and therefore the flux, would be forced to zero. However, the high frequency tilt is a useful parameter with which to investigate flow distortion, because it directly represents any changes in wind direction as opposed to either w_{SM}' or u_{SM}'.

5.1.3 Ship motion parameters and inter-correlations

The anemometer has 6 degrees of freedom: pitch (*P*), defined here as positive when the bow lifts, roll (*R*), positive when port-side lifts, yaw (*Y*), positive when the bow turns to port, (*x*), positive to fore, (*y*), positive to port, and (*z*) positive

upward. All angles are in degrees and all motions in metres. There is also the time derivative of each, e.g. dz/dt. There are thus a large number of motion series (12), which can be correlated with each other in a complex manner. Some are usually strongly correlated (e.g.: the pitch and vertical displacement), some unambiguously out of phase with each other by $\pi/2$ radians (e.g.: vertical displacement and vertical velocity), and some pairs correlated in an unpredictable way dependent on the specifics of a given record (e.g.: the correlations between pitch and fore-aft horizontal motion can take a wide range of values, influenced not merely by the wave field but the ballast distribution of the ship, which is actively altered regularly).

All of these motion series may directly influence the wind, although it is shown in due course that P, z, and their first derivatives alone dominate the motion bias for bow on winds. Note that the translational velocity components of the anemometer induced by rotation about the motion pack are small (order 1 cm s^{-1}) compared to the directly measured motion pack velocities (order 1 m s^{-1}). This means the motion sensor vector (what is measured) is nearly equal to the anemometer vector (what is desired), so the two are assumed equal. The correlations between P, z, dP/dt and dz/dt are of critical importance to the remainder of this work.

After defining all appropriate parameters above, a representative example record is used to introduce several facets of the present investigation. First, which motion parameters are best correlated to the wind? Second, how do inter-correlations between the most important motion parameters complicate the interpretation of R^2 (γ_F,*motion*)? Third, a novel correction method is introduced that uses a time-varying, motion-parameterised tilt, rather than a constant value, in Eqs. 5.6 and 5.7. Fourth, the influence of motion inter-correlations on the correction outcome is discussed. After these issues have been introduced using a single example, the analysis extends to the average behaviour of the set of quality controlled records with bow-on winds that was the objective of the previous chapter. Validation against the interpolated flux results is finally presented; the findings are that the correction method performs excellently, although appears biased high by approximately 10% with respect to the interpolated results during the rare instances of a combination of low wind speeds and large rolling motions.

5.2 Example record correction

5.2.1 Tilt and motion correlations

A typical 30-minute record was selected that displayed multiple modes of ship motion. U_{N10} was a moderate 10 m s^{-1}. Standard deviations of P, R, and Y were 0.95, 0.75, and 0.77 ° respectively. Standard deviations of x, y, and z were 0.57, 0.42, and 1.04 m respectively. The relative mean wind direction was 10 ° to port of bow-on and the ship was steaming in to the wind at 6 m s^{-1}. Note;

Table 5.1 is referred to at several instances in this section; at this point in the discussion only the second column is of interest. The information in columns 3 and 4 is presented here to allow direct comparison and to avoid repetition. Explicit mention of the appropriate column is always provided in the text.

The second column of

Table 5.1 lists the correlations between high frequency tilt and each of the 12 types of motion. Highlighted in the table are significant correlations of γ_F with P and z, and with their time derivatives dP/dt and dz/dt. This is intuitive for bow-on wind directions; as the bow moves up and down, it pushes up and pulls down the airflow, which is consistent with the positive correlations observed between the high frequency tilt and the bow velocity. The bow orientation/position is correlated with the tilt. This is also sensible given that the ship profile as 'seen' by the flow changes so flow distortion should alter accordingly. It is not intuitive what sign the correlation between the high frequency tilt and the bow orientation should be; it happens to be negative for the JCR. As the bow goes down the superstructure downwind presents a larger object for flow distortion, which – speculatively - could explain why the correlation is negative. There are also significant correlations between the high frequency tilt and other motion types that are less obviously linked to flow distortion, e.g. motion perpendicular to the flow; dy/dt. It shall be demonstrated in due course that such correlations are spurious; i.e. artefacts of motion inter-correlations.

Motion	No Correction $R^2(\gamma_F,\text{motion})$	dP/dt Correction $R^2(\gamma_{F(dP/dt)},\text{motion})$	dP/dt, P Correction $R^2(\gamma_{F(dP/dt,P)},\text{motion})$
P	**-0.19**	**-0.21**	0
dP/dt	**0.55**	**0**	0
R	-0.09	-0.02	-0.06
dR/dt	-0.10	0.02	0.06
Y	0.09	0.02	0
dY/dt	-0.15	0.06	-0.01
x	0.11	-0.01	0.04
dx/dt	0.26	0.05	-0.04
y	-0.23	-0.14	-0.08
dy/dt	0.27	-0.08	0
z	**-0.40**	**-0.22**	-0.03
dz/dt	**0.45**	**0.03**	0.04

Table 5.1 – Column 2 contains correlations between the high frequency tilt and each motion series. Column 3 contains similar correlations but using the high frequency tilt after a linear trend with respect to dP/dt has been removed. In Column 4, the high frequency tilt has had two successive linear trends removed, with respect to dP/dt, then to P

Each of the bow-position and bow-velocity pairs of correlations are not identical; i.e. *dP/dt* appears better correlated to flow distortion than *dz/dt*, and *z* better correlated to flow distortion than *P*. However, it should be noted that this 'face value' interpretation does not account for the inter-correlations between each of the major motion types (*z*, *P*, *dz/dt*, and *dP/dt*). There is in fact an aliased component in the correlations between the high frequency tilt and each motion series, discussed below.

P and *z* are very well correlated with each other because the sensors are sited very close to the front of the ship. As the bow tilts upward, the sensors lift (Figure 5.2.a), with *z* usually (but not always) lagging behind *P* in phase.
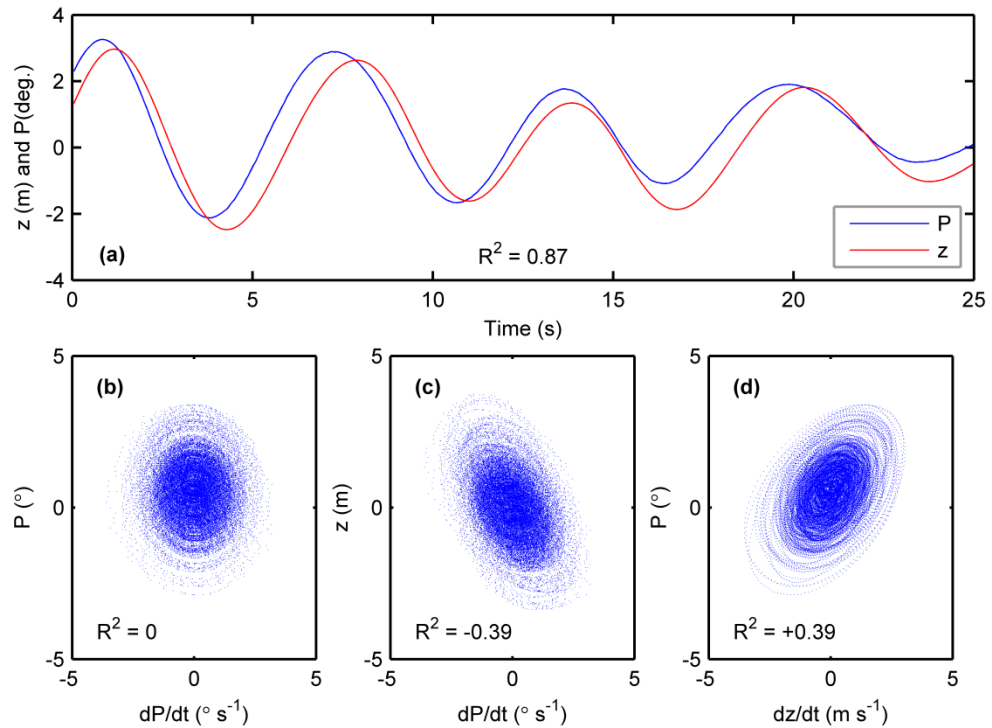
Figure 5.2 - (a) Time series of pitch (*P*) and vertical displacement (*z*). (b) *dP/dt* vs. *P*; no correlation (c) *dP/dt* vs. *z*; negative correlation. (d) *dz/dt* vs. *P*; positive correlation

Three results are important, and true for the vast majority of records with bow-on winds:

- The correlation between *P* and *dP/dt* is zero (Figure 5.2.b). This is also true between *z* and *dz/dt*

- *dP/dt* and *z* are correlated to some extent (Figure 5.2.c). The correlation is usually negative for most records, when *z* lags *P*, but can be positive when *z* leads *P*

- The correlation between *dz/dt* and *P* (Figure 5.2.d) is equal in magnitude but of the opposite sign to the correlation between *dP/dt* and *z*. This is because the differences between *z* and *P* are almost completely described by a simple phase lag

Generally speaking; if parameter 1 influences the result of an experiment, and parameter 2 independently influences the result, then a fraction of the correlation between parameter 1 and the result is aliased from parameter 2, if parameters 1 and 2 are themselves correlated. The high frequency tilt has differing correlations

with *dz/dt* and with *dP/dt* because of aliasing from *P* and *z* (respectively). This issue means it is not trivial to discern which motion parameter best represents the effects of flow distortion; deeper investigation was required. Nevertheless, it is clear that there are two types of flow distortion; the dominant type influenced by the velocity or rotation rate of the bow (*dz/dt* or *dP/dt*), and a secondary type influenced by the position or orientation of the bow (*z* or *P*).

A correction method for flow distortion must incorporate one of *dz/dt* or *dP/dt*, *and* one of *z* or *P*, in order to account for both flow distortion types. The aliasing effect caused by correlations between the important motion types must be accounted for by the correction method. In addition, flow distortion from other modes of motion, such as roll, cannot be discounted; this is indeed a problem in a minority of records, discussed in due course.

5.2.2 Application of correction

It is standard practice to apply a single mean rotation to the wind series to tilt the coordinate system from the earth horizontal streamline frame to the tilted streamline frame. To improve upon this, a motion-parameterised component can be added to the mean tilt. For each 30-minute record, the gradient of a linear fit between γ_F and *dP/dt* (Figure 5.3.a) is evaluated and used to calculate the motion induced, time-varying tilt:

$$\gamma_{dP/dt} = \gamma_M + \alpha.\frac{dP}{dt} \tag{5.10}$$

where γ_M is the mean tilt during the whole record as calculated by standard methods, $\gamma_{dP/dt}$ is the time-varying component of the tilt, parameterised by *dP/dt*, and   is $d\gamma_F / d[dP/dt]$. In this case the goodness of fit between the model (the linear fit) and γ_F is 0.31. This value is less than $R^2(\gamma_F, dP/dt)$ (which is 0.55) because a fraction of the variability of γ_F is from turbulence; it is not desired to remove this variability. Coordinate rotation using the parameterised tilt rather than the mean tilt reduces the variance in the streamline vertical wind: Figure 5.3.c   shows $w_{S,dP/dt,}$, the tilted vertical wind series derived using $\gamma_{dP/dt}$.
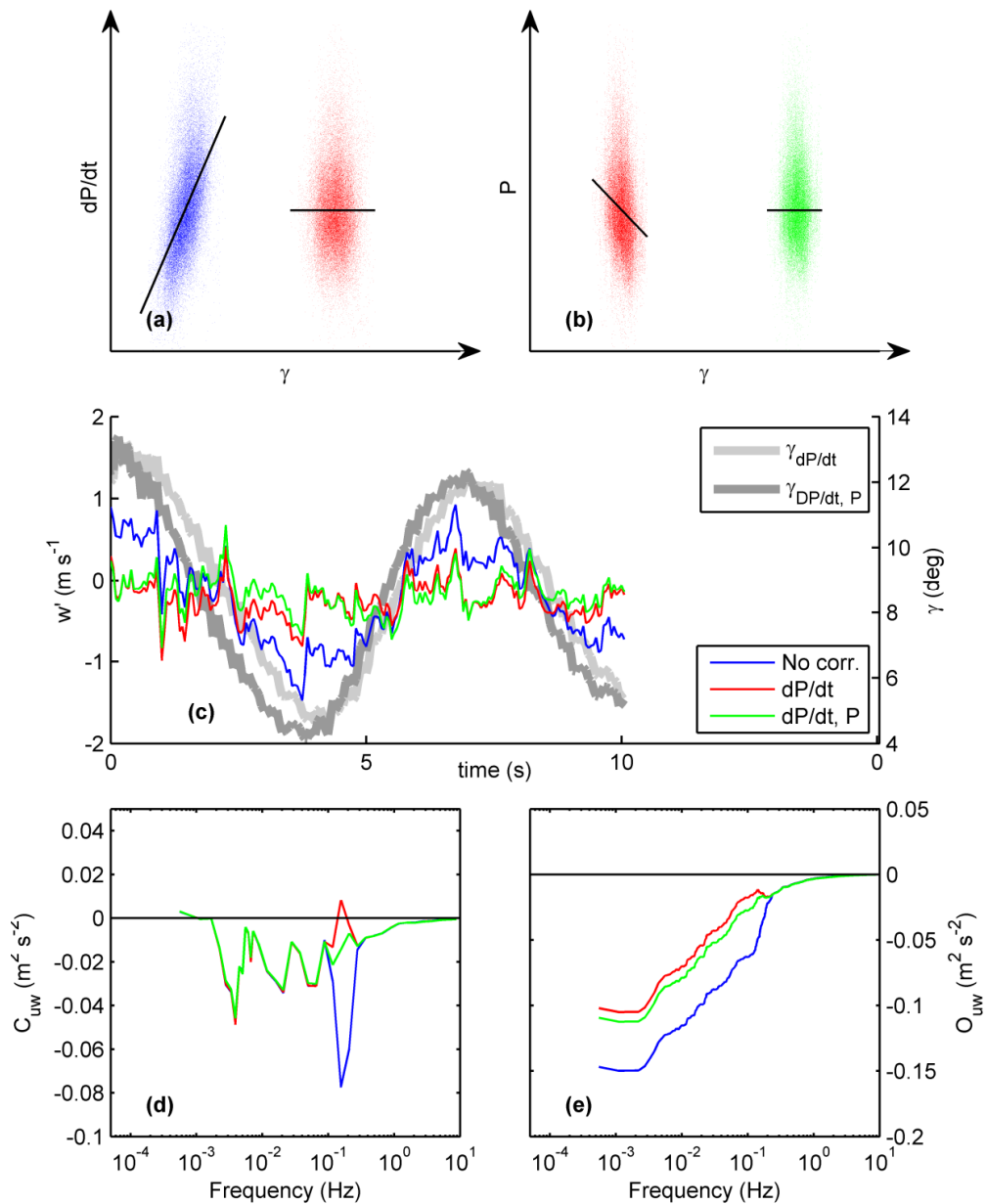
Figure 5.3 - Demonstration of the correction of one record using *dP/dt* then *P*. First the dependency of the high frequency tilt on *dP/dt* is removed (a; transition from blue to red). Subsequently with *P* (b; transition from red to green). Linear fits are shown in black. The effect of using the corrected tilt to compute the vertical wind series (c), and the effect shown on the frequency-weighted flux cospectra (d) and ogive.

Incorporation of a second motion type into the tilt parameterisation leads to further improvement. The second correction is applied subsequently (Figure 5.3.b); i.e. the linear fit is computed between *P* and the high frequency tilt that has had *dP/dt* dependency removed ($\gamma_{F(dP/dt)}$).

$$\gamma_{dP/dt,P} = \gamma_M + \alpha.\frac{dP}{dt} + \beta.P \qquad\qquad (5.11)$$

where $\gamma_{dP/dt,P}$ is the time-varying tilt, parameterised by both dP/dt and P, and β is $d\gamma_{F(dP/dt)} / dP$. In this example the goodness of fit of the model is only 0.05, which explains the relatively small effect of the second correction. The motion contamination is now almost entirely removed (Figure 5.3.c-d; green lines). The momentum flux, as corrected for by dP/dt then P in this way, is defined by $\tau_{dP/dt,P}$ (N m^{-2}).

Removal of the dependency of the high frequency tilt on dP/dt, and then on P, alters the correlations between the high frequency tilt and the other motion types (Table 5.1; columns 3 and 4) because of the motion inter-correlations. Importantly, the difference between R^2 (P, γ_F) and (P, $\gamma_{F(dP/dt)}$) is small, i.e. the dP/dt correction barely affects the correlation of the high frequency tilt with P. This is because dP/dt and P are not correlated, and means that the resulting flux value is not affected by the order in which the two corrections are applied; i.e. $\tau_{dP/dt,P}/\rho = \tau_{P,dP/dt} / \rho = -0.110$ m^2 s^{-2}.

In contrast, corrections using cross-correlated motion types (e.g. dP/dt and z) are not commutative, i.e. the result varies depending on the order in which the corrections are applied. This is illustrated in Table 2, where correction for dP/dt has altered the correlation between the high frequency tilt and z; $\gamma_{dP/dt,z} \neq \gamma_{z,dP/dt}$. In this example, $\tau_{dP/dt,z}/\rho = -0.105$ and $\tau_{z,dP/dP}/\rho = -0.125$, a difference of 20% (c.f. the value of -0.110 above). However an iterative derivation of $\lambda_{dP/dt,z}$, i.e. removing dP/dt dependency, then z, then dP/dt etc., resulted in a converged flux solution where $\lambda_{iter(dP/dt,z)} = -0.115$ regardless of which parameter was chosen first. Iteration allows the use of correlated motion parameter pairs (as opposed to being limited to uncorrelated pairs) to be investigated, It was found that the only pairs of motion parameters that were consistently uncorrelated were all parameters with their own first derivative (e.g. dP/dt and P). Iteration also allows the potential inclusion of more than two parameters in the correction. In the example, after correction for dP/dt then P, there were no correlations of the high frequency tilt with motion. This is not always the case, as will be demonstrated in due course, during a combination of low relative wind speeds and large rolling motions.

5.2.3 Physical manifestation of flow distortion

Some qualitative deductions regarding two separate mechanisms of flow distortion can be made using the evidence described thus far (Figure 2.1Figure 5.4). It was suggested (pers. comm. Ian Brooks) that the up and down motions of the foredeck push up and sucks down the air mass above it. This effect is most significant during the highest velocity phase of the motion cycle, hence the tilt correlation with velocity parameters. The positive sign of the tilt vs. velocity correlation is coherent with this theory. The effect is strongly correlated to increasing ship motion, which is sensible given that larger deck motions are faster as they cross the horizontal when the motion range is larger, because the gravitational restoring forces act over a greater motion range. The negative correlation of the velocity effect with wind speed is also sensible; the pressure induced term is not related to wind speed, and so a larger wind speed would reduce its relative importance.

It is also reasonable to assume that the aspect of the ship to the flow alters the mean airflow. If this is not accounted for when performing the tilt correction, by using only a single mean tilt, (eq. 5.6 and 5.7) then there is likely to be position correlated aliasing of u_{SM} into w_{SM}. Aliasing of u_{SM} into w_{SM} would increase as the mean horizontal wind speed increased, further supporting the theory.

If these two theorised mechanisms are accurate, it would be expected that the mean relative wind speed would control the relative importance of each. This is demonstrated to be true in the next section. Whether or not the two flow distortion mechanisms are truly independent is difficult to assess from the measurements because of the aliasing effect.

It is not possible from the measurements to ascertain whether the tow mechanisms are the result of flow distortion from either: the large but relatively distant foredeck and superstructure or; the small but relatively close mast, instruments, and mast deck. Modelling studies have found that the latter has influence on the mean flow distortion, so it is likely that the motion-correlated flow distortion would have some contribution from the close objects.

Adequate turbulent pressure measurements were not available to test the hypothesis of dynamic pressure fluctuations causing bow-velocity correlated flow

distortion. Tracer photography from a nearby boat might be a reliable way fo testing the flow distortion explanations given here. Also, there has been some work (Popinet et al., 2004) running Large Eddy Simulations over a ship; it may be possible to incorporate boat motion into such a study, although additional dynamic forces would have to be included, as opposed to a static model. The author is not aware if this is currently possible.
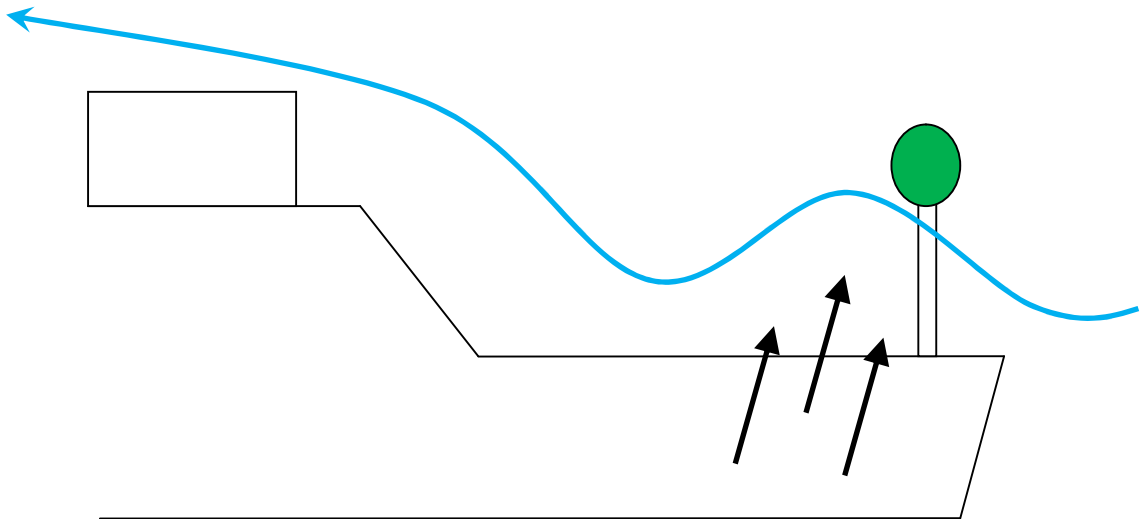
Ship moving upward; high pressure bulb reshapes airflow.
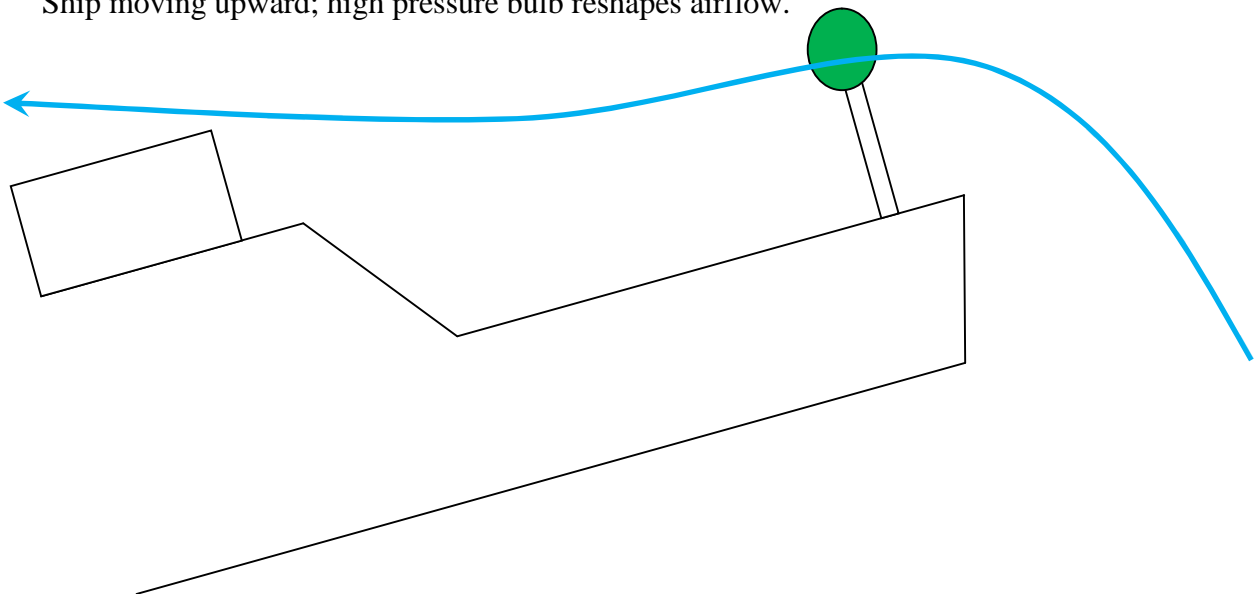
Ship tilted upward; flowlines respond to different object profile.

Figure 5.4 – Schematic of two different flow distortion modes. Top panel: streamlines alter from dynamic pressure effect. Bottom panel: streamlines alter as the aspect of the ship to the flow changes shape. Sensors in green; ship dimensions are approximately accurate.

5.3   Tilt vs. motion correlation coefficients over all records

Data were restricted to those with bow-on relative wind directions in order to simplify the physical problem. Only these records are suitable for drag coefficient calculations because of the need for a mean wind speed correction; only one bow-on correction for the JCR was available. 2235 records that had relative wind directions ±20 degrees of bow-on were included, rather than the more strict ±10 degree limit, to increase the volume of data. When drag coefficients are calculated (toward the end of the chapter) and U_{N10} is required, the ±10 degrees restriction was reinstated. Any records taken when the ship heading range was more than the norm for wave-correlated motion were removed using a simple threshold on the standard deviation of yaw; 1750 records had standard deviation of yaw less than 5 degrees, with a long tail of higher values indicating records with significant heading change. Records measured during relative and true mean wind speeds below 5 m s^{-1}, were removed, and all the ogive quality control stages outlined in chapter 4 were applied, leaving a data set of 947 records that covers all encountered ship motion characteristics (e.g.: beam-on swell inducing roll motions, or following swell propagating against the wind).

The correlations between the high frequency tilt and the four major motion types are clearly controlled by the mean relative wind speed and characteristics of motion (Figure 5.5). Several qualitative insights into the physics of motion-correlated flow distortion can thus be deduced.
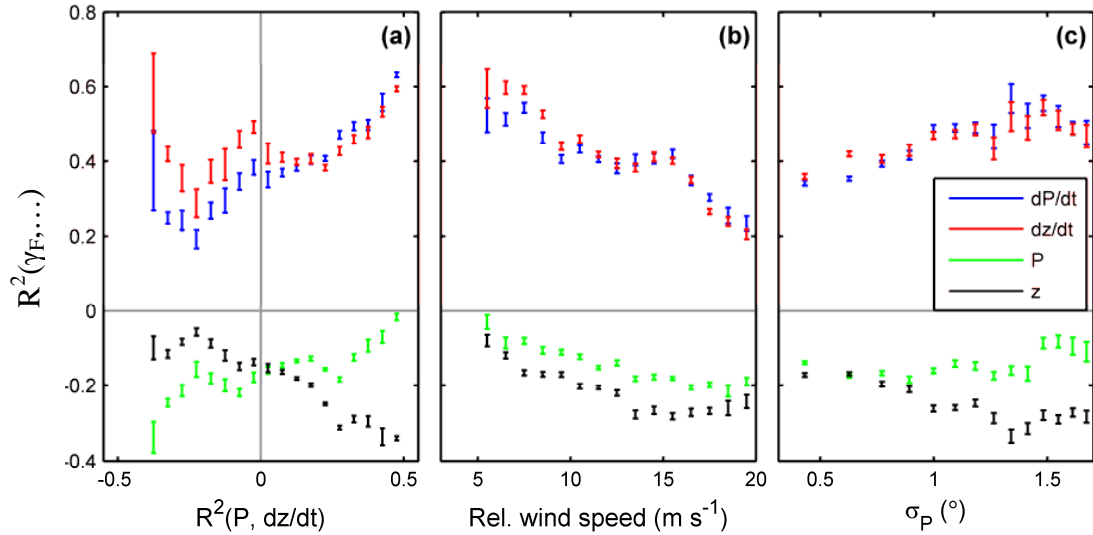
Figure 5.5 - Correlations between the high frequency tilt and the 4 major motion types, shown as a function of the a) correlation between *P* and *dz/dt*, b) the mean relative wind speed, and c) standard deviation of pitch. Error bars indicate standard error of the mean

The correlations of *P* and *z* with the high frequency tilt are controlled largely by the cross-correlations of *P* and *z* with *dz/dt* and *dP/dt*, respectively (Figure 5.5.a). However, the correlations of the high frequency tilt with *P* and *z* are not *completely* aliased from the bow-velocity motion types; evident when $R^2(P, dz/dt)$ is zero, $R^2(P, \gamma_F)$ and $R^2(z, \gamma_F)$ are not zero. For most records, the correlation of the high frequency tilt with the bow-velocity is typically greater in magnitude than with the bow-orientation. This explains why flow distortion correlated to the bow-orientation is more heavily influenced by aliasing than flow distortion correlated to the bow-velocity.

As the relative wind speed increases (Figure 5.5.b), flow distortion correlated to the bow-orientation increases, and flow distortion correlated to the bow-velocity reduces. This is sensible: first, a pumping effect correlated to the bow-velocity would have less impulse time and therefore less influence on faster flow; second, faster flow should be deflected more than slower flow by a given perturbation from the mean of the bow-orientation.

The transition in correlations over the wind speed range is not controlled by aliasing; evident because the correlations of *P* and *z* with the high frequency tilt

do not diverge toward the lower wind speeds, toward which aliasing caused by bow-velocity flow distortion should be at its largest. Such divergence *is* observed over the range of the standard deviation of pitch (σ_P; Figure 5.5.c); the divergence is evidence that aliasing is significant. Therefore σ_P does not have a clear direct control on bow-position correlated flow distortion, although σ_P does control bow-velocity correlated flow distortion.

In order to implement the correction described in section 5.2, a combination of parameters must be chosen: one from *P* and *z*, and one from *dP/dt* and *dz/dt*. This choice should be guided by results from the whole data set. Toward the lower relative wind speeds, *dz/dt* is more strongly correlated than *dP/dt* with the high frequency tilt. This reverses toward the higher relative wind speeds. The transition is unlikely to be caused by aliasing, because at the lower wind speeds the bow-orientation flow distortion is at its smallest; i.e. divergence caused by aliasing is at a minimum, so differences between the tilt correlation with *dP/dt* and *dz/dt* are controlled by wind speed directly. This implies that to remove the effect of bow-velocity flow distortion, it is unlikely that either of *dP/dt* or *dz/dt* is universally the best motion type to use in the correction. We cannot determine from Figure 5.5 which of *P* or *z* which is better to use in a correction method because the aliasing effect is severe.

To summarise; there are two flow distortion mechanisms, related to the position and velocity of the bow, respectively. The relative wind speed controls the proportional influence of each. It is unclear which combination of *dP/dt*, *dz/dt*, *z* and *P* is best in a correction algorithm because of the influence of motion cross-correlations. Each combination is therefore tested against the interpolated results in the next section.

5.4 Validation

Interpolation is acknowledged to be an imperfect reference measurement, but no alternative is available. However, it was demonstrated in the previous chapter that that a parameterisation of the drag coefficient derived from the interpolated results is in good agreement with several commonly cited parameterisations.
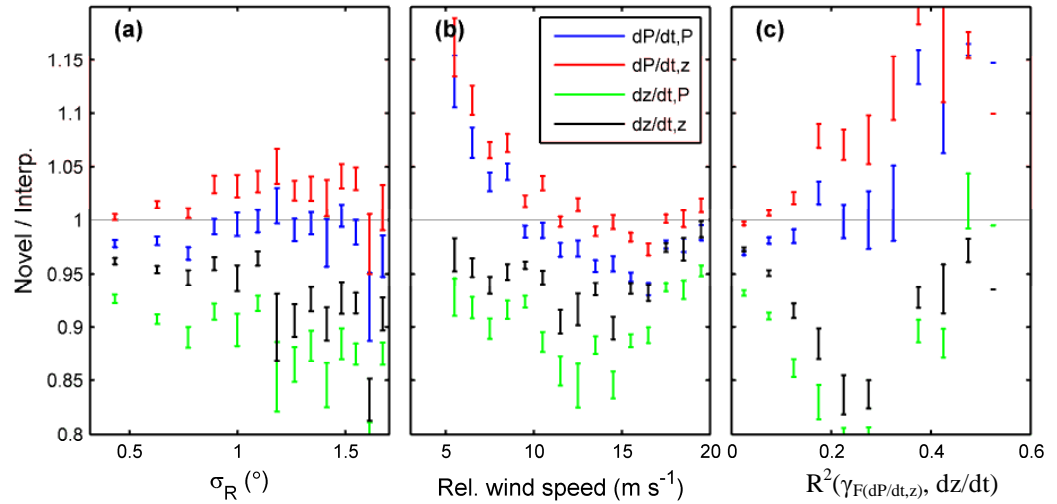
Figure 5.6 - Direct comparison between the novel corrected fluxes with the interpolated fluxes, using the four combinations of motion parameters, shown as a function of the: a) standard deviation of roll; b) mean relative wind speed; and c) the remaining correlation between the high frequency tilt and *dz/dt* after correction for *dP/dt* and *z*. Error bars indicate standard error of the mean.

The ratio between each corrected and interpolated record is evidently a function of the standard deviation of roll (Figure 5.6.a; σ_R) and the relative wind speed (Figure 5.6.b). The correction method using the pair of *dP/dt* and *z* performs exceptionally well on average when either the relative wind speed (U_{REL}) is above 10 m s^{-1}, or the standard deviation of roll is below 0.8 °. However the correction method is biased high (i.e. gives a more negative momentum flux) with respect to the interpolated results during low relative wind speeds or high roll variances. The data were split into 4 groups using 0.8 ° and 10 m s^{-1} as thresholds: high/low σ_R and high/low U_{REL}. It was found that only the combination of high σ_R and low U_{REL} caused a lack of agreement between the *dP/dt* and *z* correction and interpolation. The mean cospectra (Figure 5.7) demonstrate this clearly. The corrected results using *dP/dt* and *z* for the 114 records with low relative U_{REL} and high σ_R were biased $15 \pm 15\%$ high from the interpolated results, and the bias clearly increases as the wind speed reduces (Fig. 6b). The remaining three data groups, which comprised the other 866 records, were biased by $0 \pm 10\%$, $0 \pm 6\%$ and high by $3 \pm 6\%$.
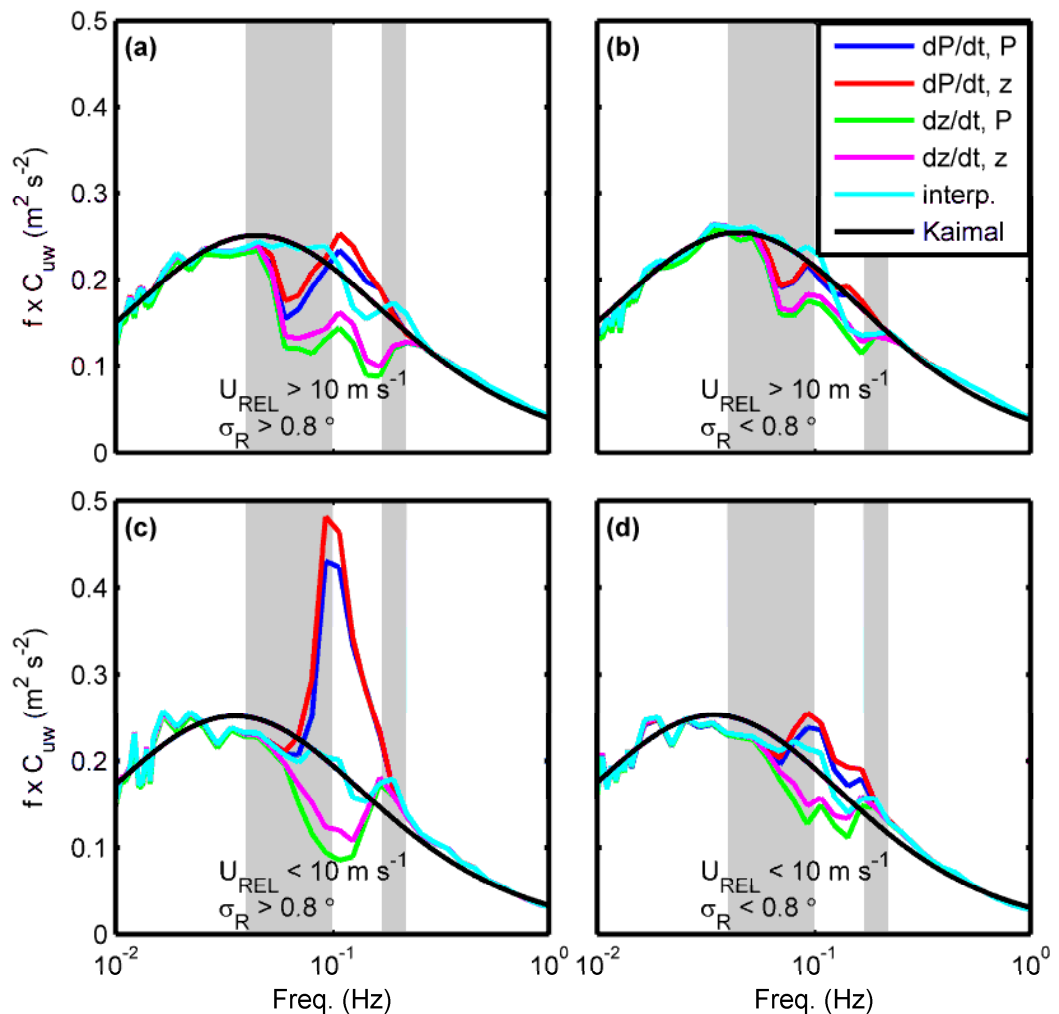
Figure 5.7 - Average cospectra; each cospectrum normalised by interpolated covariance before calculation of mean. Mean cospectrum then bin-averaged. Four types of record selected: a) high U_{REL} and high σ_R; b) high U_{REL} and low σ_R; c) low U_{REL} and high σ_R; and d) low U_{REL} and low σ_R. Grey bands indicate the range of upper and lower limits for the pitch frequency range.

During large rolling motions, given that records are restricted to bow-on winds, it is almost certain that that strong swell is present, assuming that the wind sea induces pitching motion alone. If the residual anomaly in the cospectrum was swell-induced upward momentum transfer, it would be expected to manifest as an upward contribution at the lowest ship motion frequencies (e.g. Grachev and Fairall, 2001; Hristov et al., 2003; Hanley et al., 2008; Sullivan et al., 2008);

however the anomaly is on average downward and peaks at frequencies around 0.1 Hzs, too high for typical swell. Therefore the bias is most likely a limitation of the *dP/dt* and *z* correction pair rather than a contribution from a swell induced component.

After application of the *dP/dt* and *z* correction, it was found that the remaining correlation of the high frequency tilt with *dz/dt*; R^2(*dz/dt* ,$\lambda_{f(dP/dt,z)}$); best explained the deviation from the interpolated value (Figure 5.6.c). Is a different correction pair more suitable during low relative winds and large rolling motions? Applying *dz/dt* instead of *dP/dt* in the correction does not lead to agreement with the interpolated fluxes, but this may be a better correction because the residual motion-correlated anomaly in the cospectrum is upward and could therefore be swell-induced. Without a reference measurement, from a buoy or tower for example, it is not possible to make a defensible case for any of: the method being limited; swell effects; or some combination of both.

It was attempted, unsuccessfully, to reduce the motion-correlated anomaly by including more than two motion series in the correction loop. During the records with low U_{REL} and high σ_R, the high frequency tilt was correlated to both the roll and change of rate of roll. Both were in turn correlated to some/all of *dP/dt, dz/dt, P* and *z* in an unpredictable way. An iterated correction was applied that used all 6 motion types, repeated 5 times, to test for improved agreement with the interpolated fluxes; applying three random sequences of the 6 parameters. Results from each of the three sequences did not even agree with each other to within 15% on average, therefore a correction that requires more than two parameters is clearly not valid.

5.5   Drag coefficient and Charnock parameter vs. wind speed

The 558 records that had relative mean wind directions within ± 10 ° of the bow were selected; this because the modelled mean flow corrections of Yelland et al. (2002) are only valid within this range. The relationship between U_{N10} and our results were compared (Figure 5.8.a) to a set of drag coefficient parameterisations from the literature; including the values output from the COARE 3.0 bulk flux algorithm (Coupled Ocean Atmosphere Response Experiment; Fairall et al.,

2003). It is apparent that the WAGES results are higher than Yelland et al. (1998) and Smith (1980), and more in agreement with COARE 3.0 and Edson et al. (2013); although differences are within several percent, which is within the variability that may be expected due to different swell and fetch conditions encountered during the different experiments.

Interestingly, if the records with high roll variance are removed, accepting 281 records, then the results fall more into line with those of Yelland et al (1998), and Smith (1980). However the removal of such records is controversial; filtering by roll variance is almost certain to remove all of the cases with significant swell propagating in the cross wind direction. It was also shown that the correction method itself may be limited in this regime. Without a reference measurement it is not possible to ascertain which, or both, of these two effects contributes to the change.

Above U_{N10} of 10 m s^{-1} the results match COARE 3.0 exceptionally well. The COARE 3.0 algorithm was tuned to a large number of ship-based studies; both EC and inertial dissipation flux estimates were merged. Therefore flow distortion may have influenced the COARE 3.0 data set, although a recent aggregation of measurements by Edson et al. (2013) showed that within the moderate wind speed regime (covering the 10-15 m s^{-1} range discussed here). Results from ships were avoided; Edson et al. (2013) used results from buoys and moorings (CLIMODE; Climate Mode Water Dynamic Experiment; Marshall et al., 2009) and the stable low profile research platform *FLIP* (MBL; Marine Boundary Layer Experiment; Hristov et al., 2003) matched the COARE 3.0 results.
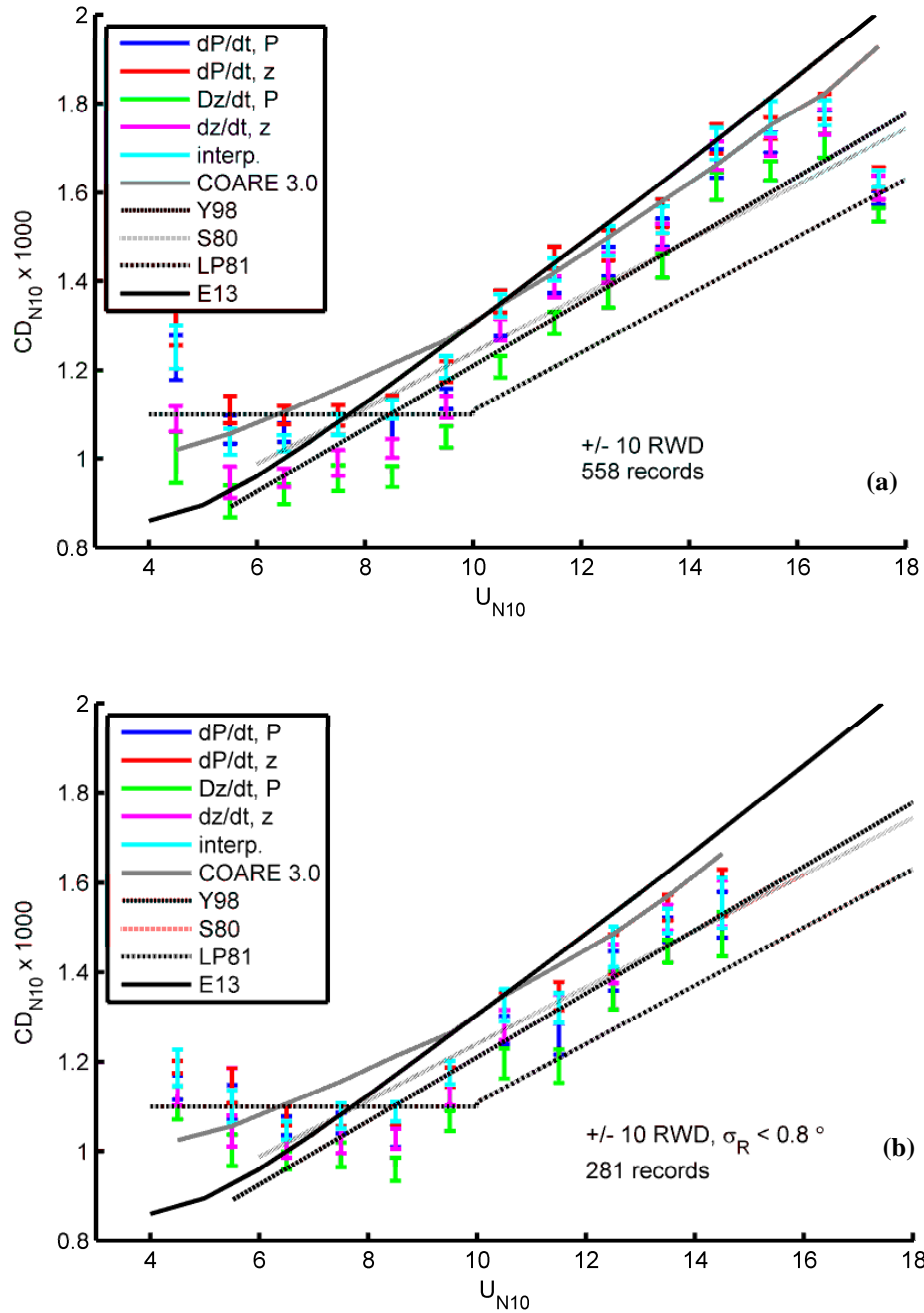
Figure 5.8 - 10 m neutral drag coefficients (CD$_{N10}$) versus mean 10 m wind speed (U$_{N10}$) computed from the interpolated fluxes, and those from each parameter permutation of the novel correction method. Several parameterisations are displayed: Yelland et al. (1998; Y98), Smith (1980; S80), Large and Pond (1981; LP81), the output of the COARE 3.0 bulk flux algorithm, and Edson et al. (2013). (a) All records that passed spectral QC and had relative wind directions (RWD) within ±10 degrees of bow-on accepted. (b) Additionally a restriction on the standard deviation of roll was imposed.

Toward lower wind speeds the WAGES results are biased low by several percent with respect to COARE 3.0. The recent results of Edson et al. (2013) at low wind speeds were taken from coastal towers (CBLAST-LOW; Coupled Boundary Layers Air-Sea transfer at Low winds; Edson et al. 2007) are in fact lower, noted by those authors to be likely due to the upward contribution from swell that may have been missed in the ship-based data of COARE 3.0. Two of the parameterisations presented (Yelland et al., 1998 and Large and Pond, 1981) relied on the inertial dissipation method, which has shown not to capture the influence of swell (Donelan et al., 1997). Smith (1980) used EC measurements from a stable platform but there are so few data (approximately 80 records) that trying to assess differences of order of a few percent is futile. We also did not have access to surface current measurements throughout WAGES so the true wind speed over ground is used in lieu of the wind speed relative to the water; this could cause a few percent in U_{N10}. Bias from the U_{N10} computation is also possible from the modelled corrections. However the JCR benefits from having an extremely small 1.3% correction for bow-on winds (error of 2%; Yelland et al., 2002). The influence of different swell fields and other measurement errors mean that the contribution to the total error from imprecision in the CFD correction is likely to be a minor term in comparison.

Whilst it is not possible to make further assertions by examining the drag coefficient, the Charnock parameter shows robust wind speed dependence (Figure 5.9), even when only records with low roll variances were used. The confidence in each linear fit (made above U_{N10} of 8 m s^{-1} only) is high; each R^2 value for data with large roll permitted is 0.91. When data are restricted to low roll, the R^2 values are less (0.67 and 0.78 for the interpolated and tilt corrected) but still significant; likely because there are simply less data after the roll restriction. The implications of a wind speed dependent Charnock parameter are that the drag coefficient parameterisation is not linear with respect to the wind speed. However it is noted that below U_{N10} of 8 m s^{-1}, the novel corrected WAGES results appear far too high with respect to Edson et al. (2013); this is expected because the novel method was shown to fail at low wind speeds. That the interpolated results are also too high with respect to Edson et al. (2013) at low wind speeds is interesting; it means that by removing all of the cospectral anomaly within the motion

frequency band, some real upward directed flux contribution has been removed. This upward contribution would act to reduce the overall drag, explaining why the parameterisation of Edson et al. (2013) is lower at the low wind speed range. The uncertainty in the WAGES results is in the offset - rather than the gradient - of the wind speed dependence of the Charnock parameter. It is possible, as stated previously, that removal of the records with high roll motions removes cases of cross wind swell. However, at the higher wind speeds, when there is little roll, it is clear from the WAGES measurements that the Charnock parameter is not a constant. This is a defensible result that may help to reconcile this debate.
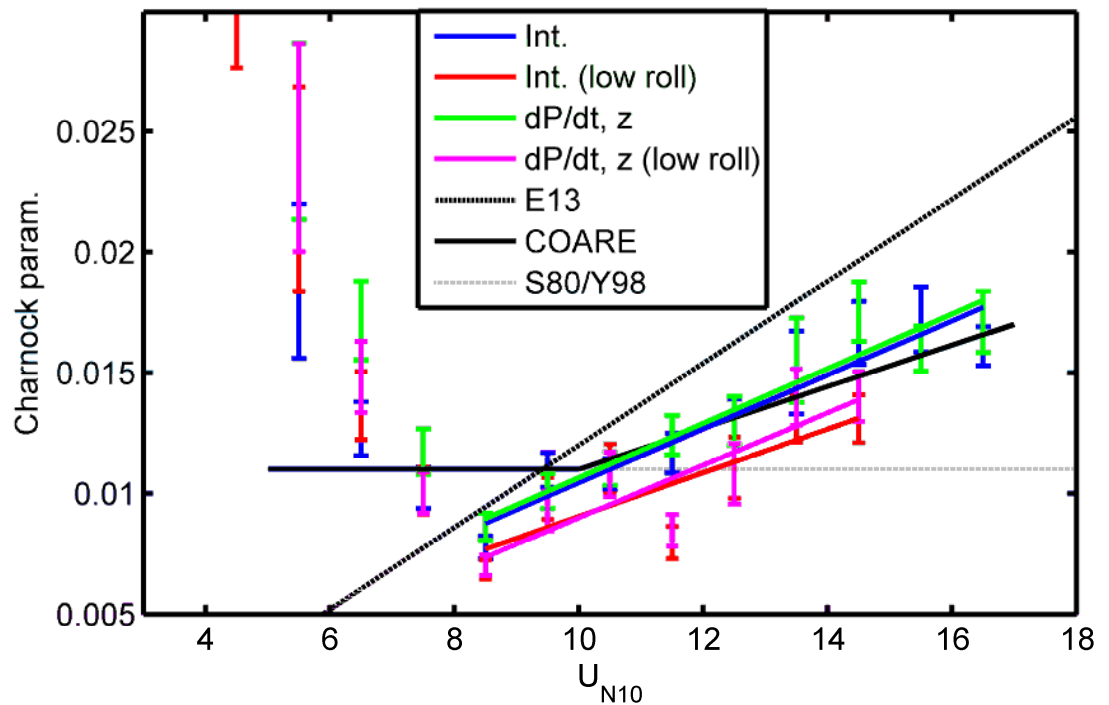
Figure 5.9 – Charnock parameter as a function of U_{N10} for the interpolated and tilt corrected fluxes. Records with only standard deviation of roll values less than 0.8 m are filtered for two of the lines. The results of Edson et al., (2013; E13), COARE 3.0, and Yelland et al. (1998; Y98) and Smith (1980; S80) are presented for comparison. The lines represent linear fits to the bin averaged data.

5.6 Conclusions

We have derived and validated a novel method for the correction of motion-correlated flow distortion for bow-on flow over a single research vessel. Correlations between the time series of turbulence and motion over a half hour period are removed. This avoids the need for spectral correction (interpolation), which is biased depending on how much of the cospectral peak lies within the ship motion frequency range; therefore the bias is a function of conditions. Two major independent types of flow distortion were found for bow on flow, one correlated to the bow orientation to the flow, and one correlated to the up and down motion of the bow. For the overwhelming majority of WAGES records with bow-on winds, a correction iterated between *dPdt* and *z* performs outstandingly well, providing the relative wind speed is at least moderate *or* the ship motion is mostly constrained to the fore-upward plane only. The level of agreement with other parameterisations of the momentum flux is excellent, and unique for a data using EC from a ship; no such parameterisations are published.

The correction method proposed is vulnerable to cross-correlations between relevant motion parameters, but this can be overcome if the correction is looped iteratively, if only two motion series directly control flow distortion. During low relative wind speeds *and* when significant roll is present, more than two motion types control flow distortion, and the correction method fails to agree with interpolated results by order 10%. The residual anomaly in the cospectra in such cases is downward directed, so not likely to be caused by swell; although the cause is not possible to determine without a reference measurement that is not subject to major flow distortion. Buoys and moorings can adequately measure fluxes in low wind conditions, so fortunately the need is not great from the air-sea flux measurement community for ship based EC measurements at low winds speeds. Ships are valuable platforms during high winds and rough seas, and here the method was demonstrated to work excellently.

We speculate that the JCR may be particularly vulnerable to motion-correlated flow distortion, because the height of the sensors is lower than the height of the superstructure, which is only tens of metres downwind of the sensors for bow-on flow. Preliminary checks of similar measurements from the *RRS Discovery*

(Norris et al., 2012) showed much less motion correlated flow distortion; the sensors being above the top of the superstructure. The correction may be simpler for other research vessels, and more robust at the lowest wind speeds. The method proposed here should be considered a template only for application to other research vessels.

No further work can be performed using the WAGES momentum flux measurements. The following short chapter investigates the sensible and latent heat fluxes, applying some of the new quality control techniques developed throughout the thesis.

6   Preliminary scalar flux study

The thesis thus far has solely been an investigation into the momentum fluxes, novel corrections and quality control methods, and how their application allows a sensible relationship between U_{N10} and CD_{N10}, derived from the EC fluxes, to be computed. A preliminary study was undertaken of the scalar fluxes with the following objectives:

- Do the scalar fluxes suffer from motion-correlated contamination? If so, how severely and prevalently?

- Can the spectral quality controls developed in chapter 4 be directly applied without modification, to the scalar fluxes, and does this reduce uncertainty in the computed scalar transfer coefficients?

- How do the WAGES scalar transfer coefficients, after quality control, compare to the work of others?

This chapter is divided into two sections, where the sensible heat and latent heat fluxes are treated identically. It was found that for both flux types, if the spectral quality control tests were not performed, then bin averaged results have such high standard errors of the mean as to be meaningless. This in itself is a very strong argument in favour of the spectral quality control tests. However, a problem arises when the records are restricted by the cospectral peak frequency; if it is too high then interpolation was demonstrated to be biased. This skewed the accepted range of atmospheric stabilities toward the unstable range, because the peak frequency is higher at positive (stable) stabilities. The cospectral peak frequency test is therefore discarded, on the grounds that interpolation is not as important a correction for the scalar fluxes; this is demonstrated below. Therefore in all plots, all spectral quality control has been conducted except the peak frequency restriction.

First the ratio of the interpolated and unaltered EC fluxes are shown to demonstrate the level of motion contamination, and also compared to the inertial dissipation flux estimates. The scalar transfer coefficients are used to validate the WAGES flux measurements, and are defined by:

$$CT_{N10} = \frac{\overline{w\,T}}{U_{N10}.\Delta T_{10}} \tag{6.1}$$

$$CQ_{N10} = \frac{\overline{w\,q}}{U_{N10}.\Delta Q_{10}} \tag{6.2}$$

where ΔQ_{10} is the difference between the specific humidity at 10 m and the saturated specific humidity of air at the sea surface. ΔT_{10} is the difference between the air temperature at 10 m and the sea surface temperature..

7931 records passed the basic quality control required in order to use the momentum fluxes. In this chapter another criterion was applied – if both Li-7500s were either shrouded or otherwise unavailable, records were rejected. This left 5296 records. 2711 records had relative and true mean wind speeds higher than 5 m s^{-1} and also passed the basic ogive quality control – a fit to the latent heat flux ogives could be found. 759 of these records had winds within ±10 degrees of bow-on, so were suitable for parameterisation calculations.

6.1   Latent heat fluxes

629 records passed spectral quality control. In order to compare results to the ID fluxes, a further restriction was required for the ID comparison alone, forcing the ship to hold position; this accepted 242 records. Figure 6.1 demonstrates that motion contamination is fairly small; the median of the unaltered fluxes over the interpolated fluxes was 1.05. This is sensible given that only the vertical wind component is sensitive to flow distortion. It is possible that the H_2O density may vary as a function of vertical displacement; a direct effect from vertical gradient of specific humidity, or a more subtle density effect caused by a temperature gradient. The contamination is a weak function of the pitch standard deviation. The direct comparison of the interpolated fluxes to the ID fluxes is highly scattered, with strong stability dependence.

.
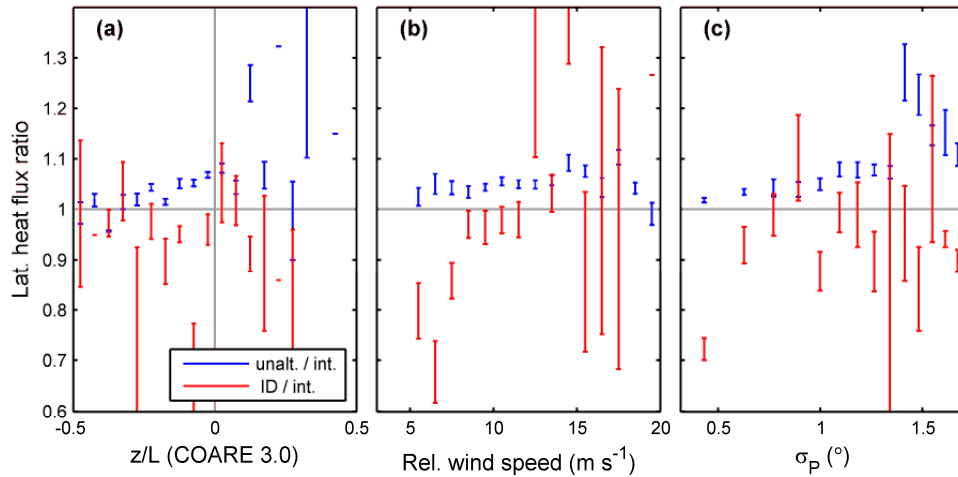
Figure 6.1 – Ratios of the EC unaltered, EC interpolated, and ID latent heat fluxes. Plotted as a function of a) the COARE 3.0 stability parameter, b) the relative wind speed and c) the standard deviation of pitch. The red data have had records with significant low frequency ship motion removed.

There appears to be a threshold in the pitch standard deviation beyond which motion-correlated contamination becomes severe; but not such a threshold for the relative wind speed. This indicates that the range of motion controls H_2O contamination; possibly movement of the sensor in a vertical gradient of humidity.

Figure 6.2 demonstrates that after full quality control, the latent heat transfer coefficient has weak dependence on the mean wind speed and stability. The respective means of the unaltered, interpolated, and ID latent heat transfer coefficients is 1.05, 1.00, and 0.9 respectively. Note that according to similarity theory, CQ_{N10} and CT_{N10} should be the same; both are transferred across the interface by molecular diffusion across a gradient. CD_{N10} differs because form drag and shear stress are different processes. Dupuis et al. (2003) found a near neutral value of 1000 x CQ_{N10} (and CT_{N10}) of 1.0 using shipboard inertial dissipation fluxes (with mean flow distortion corrections). Pedreros et al. (2003) used EC results from the same vessel and found mean values of 1.2 for unstable conditions and 1.1 for stable conditions. Large and Pond (1982) found 1.2 in unstable conditions, from a platform. Smith (1988) found a near neutral value of 1.2. Therefore, the WAGES results are biased low on average, with respect to the consensus, although the results are not completely unreasonable. Given that all

the records that passed spectral quality control have the same quality of cospectrum as the momentum flux cospectra that passed; the fluxes themselves are likely to be of high quality. The disagreements in parameterisations of the mean transfer coefficient may be caused by incorrect interpretation of the mean RH measurement; therefore a biased computation of ΔQ_{N10}. This is likely in large part to be the location of the mean meteorological sensors, on top of the bridge, where flow displacement is of order 7 m.
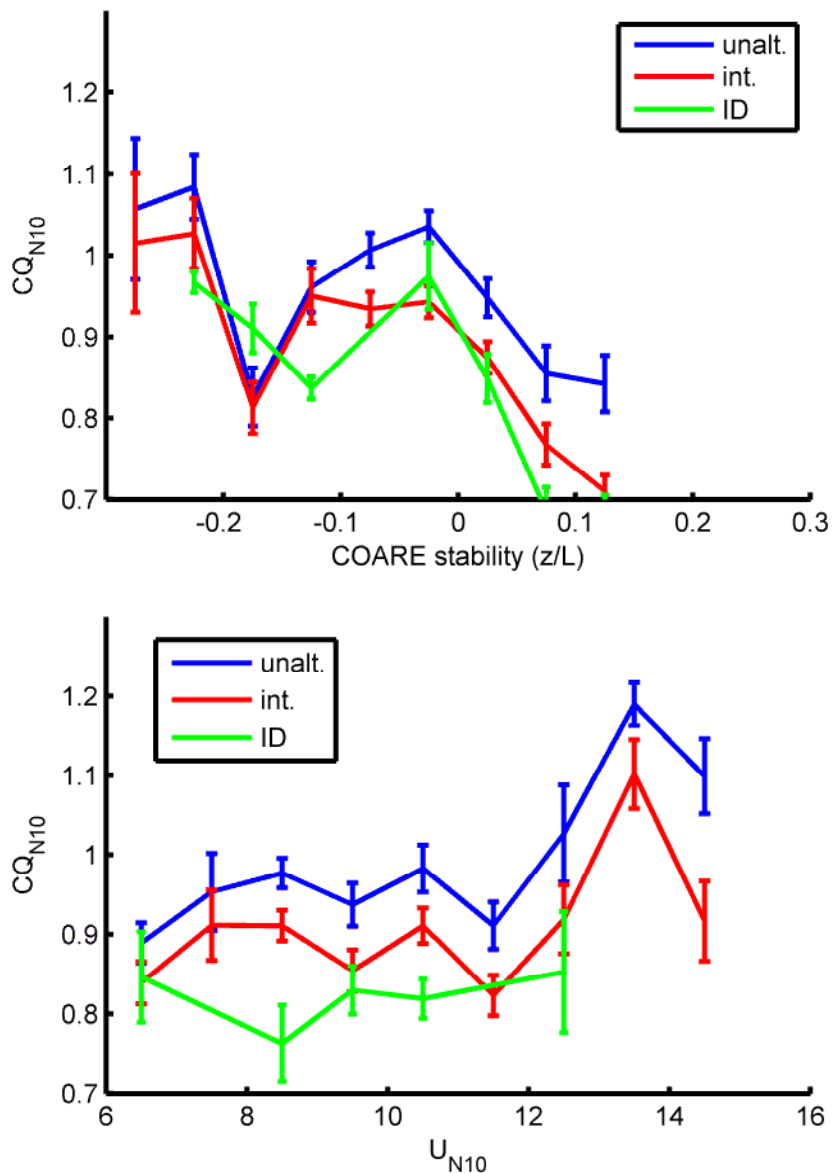
Figure 6.2 – Latent heat transfer coefficients from EC interpolated (int.), EC unaltered (unalt.), and inertial dissipation (ID) fluxes vs. the stability parameter as output by COARE 3.0, and the mean 10 m wind speed. All records passed spectral quality control, and the ID data additionally was restricted to when the ship was nominally stationary.

6.2 Sensible heat fluxes

662 records passed spectral quality control, with 268 records that had no significant low frequency ship motion. Figure 6.3 shows that, like the latent heat fluxes, motion-correlated contamination is small – the mean of the unaltered / interpolated EC fluxes is 1.10.
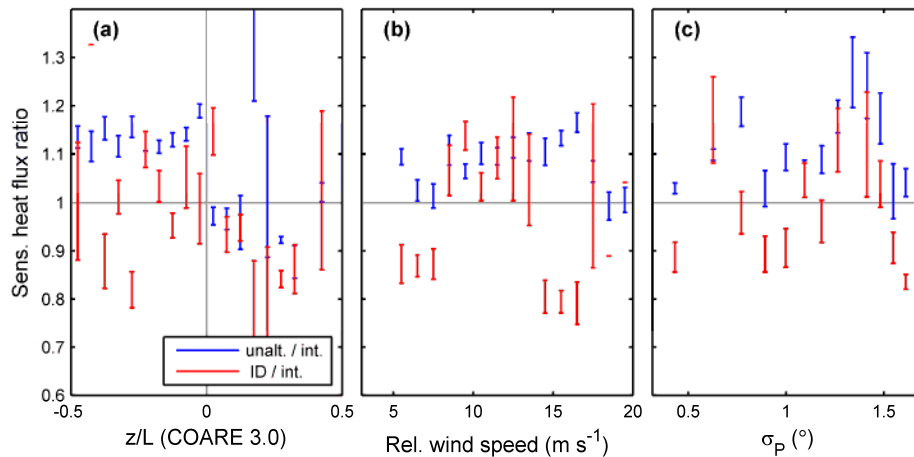
Figure 6.3 - Ratios of the EC unaltered, EC interpolated, and ID sensible heat fluxes. Plotted as a function of a) the COARE 3.0 stability parameter, b) the relative wind speed and c) the standard deviation of pitch

Motion contamination seems to have little dependence on the wind speed but there is clear dependence on the stability; Consistent contamination of about 10% of the flux is observed in unstable conditions.

The sensible heat transfer coefficients are biased very high during near-neutral conditions (Figure 6.4), which is to be expected given that air sea temperature differences are typically small, and the error in the computed air-sea temperature difference is likely to be large. The apparent dependency of CT_{N10} on the wind speed is likely an artefact of the tendency for near-neutral stability values toward higher wind speeds. Latent heat fluxes have on average a more favourable signal to noise ratio than the sensible heat fluxes, and yet still are biased with respect to the literature. It is therefore unlikely that attempts to constrain CT_{N10} using the WAGES measurements could succeed. Although, during unstable conditions, when sensible heat flux signal to noise ratios are more favourable than during

neutral conditions, the average transfer coefficient more closely matches the parameterisations of others.
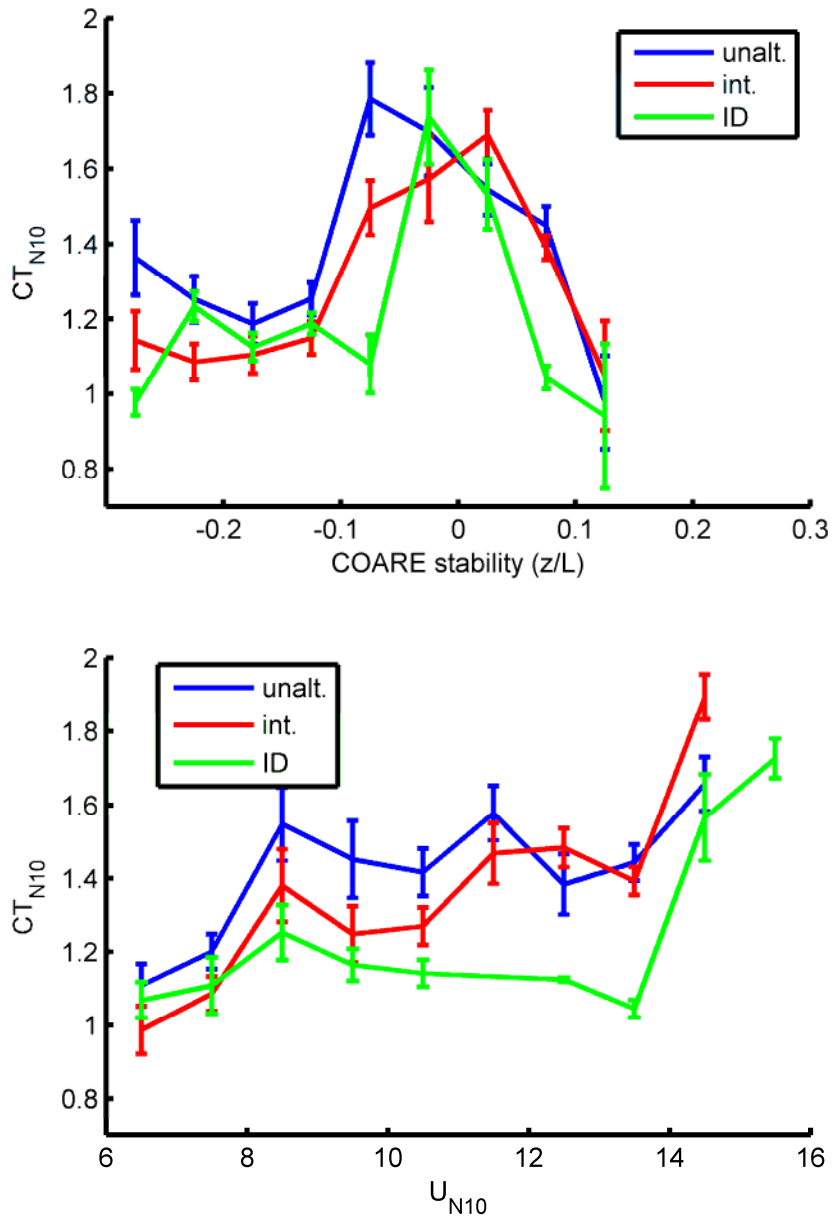
Figure 6.4 - Sensible heat transfer coefficients from EC interpolated (int.), EC unaltered (unalt.), and inertial dissipation (ID) fluxes vs. the stability parameter as output by COARE 3.0, and the mean 10 m wind speed. All records passed spectral quality control, and the ID data additionally was restricted to when the ship was nominally stationary.

6.3 Summary and further work

Preliminary application of the automated quality control technique on the latent heat fluxes shows success in removal of outliers in CQ_{N10}, and mean values agree well with the literature. The low levels of motion correlated flow distortion are promising for ship-based studies of other scalars. The latent heat fluxes have a good signal to noise ratio in typical open ocean mid-latitude conditions, using the available sensors. If motion contamination is low for these measurements then it may be assumed that for other scalars, flow distortion has a low impact on the fluxes. This does not mean that ship board measurements of other scalar fluxes would not show significant motion correlated bias; the design of the instrument may leave it prone to measurement correlated bias in the scalar signal, for example the head deformation effect observed by Yelland et al (2009) in the CO_2 fluxes.

A serious issue in computing the 10 m temperature and relative humidity has adversely affected attempts to study the WAGES scalar fluxes; the mean meteorological sensors are not sited optimally to avoid serious flow distortion. The associated uncertainty of a large height displacement at the bridge is likely the cause of systematic low bias in the average CQ_{N10}. Even if it were the case that in fact the WAGES scalar transfer coefficients were correct and the literature incorrect; without accurate flow distortion corrections at the sensor location, such claims could not be justified.

The measured series of temperature and humidity could be analysed, if time were available, using the same methodology of Chapter 5 in order to deduce which types, if any, of ship motion are correlated over a record to the scalar signal. Consistent correlations between scalars and motion may lead to better understanding of the mechanisms of instrument motion-bias, or may indicate that ant motion-correlated contamination is due to, e.g. the sensors motion up and down a vertical gradient of the scalar.

7   Summary

7.1   Conclusions

Parameterisations of the open ocean drag coefficient still have disagreements, in part due to the difficulty of obtaining large volumes of reliable open ocean eddy covariance measurements. Much of the work of this thesis discussed novel quality control tests and corrections for ship-based EC flux measurements. Previously, there have never been publishable quality data sets of EC momentum fluxes from ships, because of the large bias from motion-correlated flow distortion. This has led to a reasonably small level of disagreement persisting as to how to parameterise the open ocean drag coefficient, and whether the Charnock parameter is a constant or not.

What is of greater concern is the impact of motion-correlated flow distortion on sets of EC fluxes that have a far greater level of disagreement between studies. For example the carbon dioxide and sea spray aerosol fluxes have uncertainties between different parameterisations of several factors, even orders of magnitude; see reviews by Wannikhof et al., 2010, and de Leuww et al., 2012. If the effect of motion correlated flow distortion on the relatively well understood momentum flux cannot be quantified, then serious doubts over the validity of any ship based EC measurement must be raised. Whilst the heat and moisture time series from WAGES were not severely contaminated over the motion frequency range, the carbon dioxide series for example, can be far more heavily contaminated (e.g., Miller et al., 2010). EC studies should always explicitly address motion-correlated flow distortion, and motion-correlated contamination of the scalar measurements. To that end the work in this thesis can provide a template for studying motion-correlated contamination in other craft/instruments.

The work undertaken in this thesis has gone some way to bringing EC momentum fluxes from ships into line with open ocean flux parameterisations of others. The development of a set of new spectral based quality control tests was unambiguously a success. The fact that the quality controlled EC fluxes compared reasonably to the ID fluxes and other parameterisations is significant; recalling how poor comparisons were prior to the new quality control. If the debate rising

from the WAGES results is whether the corrected EC results are biased a few percent high or low means that, broadly speaking, vast improvements have been made to the data quality.

Likely high bias of order 10% remains when the wind speed is low and the ship rolls heavily; in this case the problem of flow distortion becomes too complicated to solve using the present methods. Since at low wind speeds, and high rolling motions, there must be a strong crosswind swell, it is not possible to disentangle a failure of the present corrections with a true wave-correlated flux contribution from swell. However, this problem is not insurmountable; a set of co-located measurements from a coastal flux tower, as a reference, would be sufficient to validate the correction method, or to put limitations on the conditions of its use. In any case, other platforms such as buoys and moorings are more suitable for deployment than ships during measurement campaigns conducted in low wind and sea conditions.

The comparisons between the ID and EC momentum flux measurements, after all corrections have been made to the EC, indicate that the ID fluxes are biased low by approximately 10%. The ID fluxes are certainly more vulnerable to mean flow distortion, and as demonstrated by modelling efforts, corrections to the mean wind speed are extremely sensitive to the relative wind direction. Additionally, the ID method is an indirect estimate of the flux rather than a true measurement, so requires more assumptions. Therefore EC measurements are more robust; providing that bias from motion-correlated flow distortion is successfully removed. It is not possible, using the WAGES measurements without proper validation, that the ID fluxes or the corrected EC fluxes are more reliable. Perhaps the strongest evidence for the success of the corrected EC fluxes comes from their agreement at moderate wind speeds with Edson et al. (2013), who avoided the use of ships entirely. However, until direct validation of the EC corrections are carried out using co-located and unbiased coastal tower measurements, it is not possible to defend either the ID or EC sets.

Some interesting insights into the physics of turbulent flow distortion over a moving platform were also revealed. The dominant mode of flow distortion, a dynamic pressure-induced bias that is correlated to the velocity of the bow, is not

recognised in the literature. Identification of the presence of two mechanisms of motion-correlated flow distortion is important; the author has had discussions with other practitioners of ship-based eddy covariance about how a simple 'de-correlation' of the vertical wind speed with respect to the pitch can be performed to remove motion-correlated bias. A simple correction in the manner was demonstrated to be totally inadequate, at least for the JCR.

Understanding and being able to make reliable predictions of air-sea exchanges is crucial to our understanding of weather, climate change, and how the ocean and atmospheric composition might change over the coming decades. Whilst models and satellite data are immeasurably useful they require validation from in-situ data. Ships provide versatile platforms from which to make these measurements over the open ocean, but understanding of bias is important when interpreting ship based data sets. This thesis has attempted to address the complex problem of motion correlated flow distortion, and some level of success has been shown using a standard air-sea flux sensor set, with the potential for additional interesting results if more measurements are analysed.

7.2   Further work

The volume of WAGES data useful for flux parameterisations could be increased from hundreds to thousands if a few more corrections for mean flow distortion were available for different relative wind directions. The wave radar installed throughout WAGES could be used to parameterise background swell levels in the open ocean, which may show influence on the drag coefficient. The continued measurements of the Li-7200 from November 2011 may provide a potentially (measurements have not yet been examined) unrivalled open ocean set of CO_2 flux measurements; with co-measured in situ whitecap fraction estimates. The physics of bubble mediated gas exchange are poorly understood, and a key unsolved problem in air-sea gas exchange is the production of a universal sea state dependent trace gas parameterisation.

The analysis of any air-sea eddy covariance data set can be assisted by application of the quality control methods and flow distortion analysis techniques outlined in this thesis. Using results across different platforms, validation of the

theories of turbulent flow distortion outlined here may be attempted; for example by looking at how the height of the sensors above the foredeck affects flow distortion. If the scalar fluxes are analysed in a similar way, it may be possible to develop parameterisations for the bias induced by motion and flow distortion. Such parameterisations could be applied to scalar fluxes for which the signal to noise ratio is not adequate for detailed spectral analysis to be undertaken (for example the Li-7500 CO_2 fluxes. Parameterisations may also allow simple corrections when re-analysing historical data for which spectra are not available.

8 References

Anguelova M.D. and Webster F.: Whitecap coverage from satellite measurements: a first step toward modelling the variability of oceaninc whitecaps, J. Geophys. Res., 111, C03017, 2006.

Anctil, F. and Donelan, M.A., Air-water momentum flux observations over shoaling waves, J. Phys. Oceanogr., 26, 1344-1358, 1996.

Aubinet, M., Vesala, T., Papala, D.: Eddy covariance: a practical guide to measurement and data analysis, Springer, 2012.

Brut, A., Butet, A., Durand, P., Caniaux, G. and Planton, S.: Air-sea exchanges in the equatorial area from the EQUALANT99 data set: bulk parameterizations of turbulent fluxes corrected for air flow distortion, Q. J. R. Meterorol. Soc., 131, 2497-2538, 2005.

Blomquist, B.W., Fairall, C.W., Huebert, B.J., Kieber, D.J. and Westby, G.R.: DMS sea-air transfer velocity: direct measurements by eddy covariance and parameterization based on the NOAA/ COARE gas transfer model, Geophys. Res. Lett., 32, L07601, 2006.

Brooks, I. M.: Spatially distributed measurements of platform motion for the correction of ship-based turbulent fluxes, J. Atmos. Oceanic Technol., 25, 2007-2017, 2008.

Brooks, I. M., M. J. Yelland, R. C. Upstill-Goddard, P. D. Nightingale, S. Archer, E. d'Asaro, R. Beale, C. Beatty, B. Blomquist, A. A. Bloom, B. J. Brooks, J. Cluderay, D. Coles, J. Dacey, M. DeGrandpre, J. Dixon, W. M. Drennan, J. Gabriele, L. Goldson, N. Hardman-Mountford, M. K. Hill, M. Horn, P.-C. Hsueh, B. Huebert, G. de Leeuw, T. G. Leighton, M. Liddicoat, J. J. N. Lingard, C. McNeil, J. B. McQuaid, B. I. Moat, G. Moore, C. Neill, S. J. Norris, S. O'Doherty, R. W. Pascal, J. Prytherch, M. Rebozo, E. Sahlee, M. Salter, U. Schuster, I. Skjelvan, H. Slagter, M. H. Smith, P. D. Smith, M. Srokosz, J. A. Stephens, P. K. Taylor, M. Telszewski, R. Walsh, B. Ward, D. K. Woolf, D. Young, H. Zemmelink: Physical Exchanges at the Air-Sea Interface: Field Measurements from UK-SOLAS. Bull. Amer. Meteorol. Soc., 90, 2009.

Brooks, I. M., M. J. Yelland, R. C. Upstill-Goddard, P. D. Nightingale, S. Archer, E. d'Asaro, R. Beale, C. Beatty, B. Blomquist, A. A. Bloom, B. J. Brooks, J. Cluderay, D. Coles, J. Dacey, M. DeGrandpre, J. Dixon, W. M. Drennan, J. Gabriele, L. Goldson, N. Hardman-Mountford, M. K. Hill, M. Horn, P.-C. Hsueh, B. Huebert, G. de Leeuw, T. G. Leighton, M. Liddicoat, J. J. N. Lingard, C. McNeil, J. B. McQuaid, B. I. Moat, G. Moore, C. Neill, S. J. Norris, S. O'Doherty, R. W. Pascal, J. Prytherch, M. Rebozo, E. Sahlee, M. Salter, U. Schuster, I. Skjelvan, H. Slagter, M. H. Smith, P. D. Smith, M. Srokosz, J. A. Stephens, P. K. Taylor, M. Telszewski, R. Walsh, B. Ward, D. K. Woolf, D. Young, H. Zemmelink: UK-SOLAS Field Measurements of Air-Sea Exchange: Instrumentation. Bull. Amer. Meteorol. Soc., 90, (electronic supplement), 9-16, 2009.

Businger, J. A., Wyngaard, J. C., Izumi, Y., Bradley, E. F.: Flux profile relationships in the atmospheric surface layer, J. Atmos. Sci., 28, 181-189, 1971

Callaghan, A. H. and White, M.: Automated processing of sea surface images for the determination of whitecap coverage, J. Atmos. Oceanic Technol., 26, 383-394

Champagne, F. H., LaRue, C. A., Wyngaard, J. C.: Flux measurements, flux estimation techniques, and fine-scale turbulence measurements in the unstable surface layer over land, J. Atmos., Sci., 34, 515-530, 1977.

Cooper, D. J., Watson, A, J. and Ling, R. D.: Variability of pCO_2 along a North atlantic shipping route (UK to the Carribean): a year of autonomous observations. Marine Chemistry, 60, 147-164, 1998.

Dobson, F.W., Smith, S.D., and Anderson, R.J.: Measuring the Relationship between wind stress and sea state in the open ocean in the prescence of swell, Atmos-Ocean, 32, 237-256, 1994.

Drennan, W.M., Kahma, K.K., Donelan, M.A.: On momentum flux and velocity spectra over waves, Bound. Layer. Meteor., 92, 489-515, 1999.

Drennan, W.M., Graber, H.C., Hauser, D, Quentin, C.: On the wave age dependence of wind stress over pure wind seas, J. Geophys. Res., 108, 8062, 2003.

Dupuis, H., Geurin, D., Hauser, D., Weill, A., Nacass, P., Drennan, W.M., Cloche, S. and Graber, H.C.: Impact of flow distortion corrections on turbulent fluxes estimated by the inertial dissipation method during the FETCH experiment on R/V L'Atalante, J. Geophys. Res., 108, 8064, 2003.

Dyer, A. J.: A review of flux-profile relationships, Boundary Layer Meteorology, 7, 363-372, 1974

Dyer, A. J. and Hicks, B. B.: Flux-gradient relationships in the constant flux layer, Quart. J. R. Met. Soc., 96, 715-721, 1970

Dyer, A. J. and Hicks, B. B., Kolmogoroff constants at the 1976 ITCE, Bound. – Layer Meteor., 22, 137-150, 1982

Dyer, A. J. and Bradley, E. F.: An alternative analysis of flux-gradient relationships at the 1976 ITCE, Boundary Layer Meteorology, 22, 3-19, 1982.

Edson, J.B. and Fairall, C.W.: Similarity relationships in the marine surface layer, J. Atmos. Sci., 55, 2311-2328 (1998)

Edson, J.B., Hinton, A.A., Prada, K.E, Hare, J.E., Fairall, C.W.: Direct covariance flux estimates from mobile platforms at sea, J. Atmos. Ocean. Technol., 15, 547-562, 1998.

Edson, J.B., Zappa, C.J., Ware, J.A. and McGillis, W.R.: Scalar flux profile relationships over the open ocean, J. Geophys. Res., 109, C08S09, 2004.

Edson, B. J., Jampana, V., Weller, R. A., Bigorre, S. P., Plueddemann, A. J., Fairall, C. W., Miller, S. D., Mahrt, L., Vickers, D., and Hersbach, H., On the exchange of momentum over the open ocean, J. Phys. Oceanogr., 43, 1589-1610, 2013.

Fairall, C.W., Bradley, E.F., Rogers, D.P., Edson, J.B., Young, G.S.: Bulk parameterization of air-sea fluxes for Tropical Ocean Global Atmosphere Coupled Ocean Atmosphere Response Experiment, J. Geophys. Res., 101, C2, 3747-3764, 1996

Fairall, C.W. and Larsen, S.E.: Inertial-dissipation methods and turbulent fluxes at the air-ocean interface, Boundary Layer Meteorology, 34, 287-301, 1986.

Fairall, C. W., White, A.B., Edson, J.B and Hare, J.E.: Integrated shipboard measurements of the marine boundary layer, J. Atmos. Oceanic Technol., 14, 338–359, 1997.

Fairall, C.W., Hare, J.E., Edson, J.B., McGillis, W.: Parameterization and micrometeorological measurement of air-sea gas transfer, Bound. Layer. Meteor., 96, 63-105, 2000.

Fairall, C.W., Bradley, E.F., Hare, J.E., Grachev, A.A., Edson, J.B.: Bulk parameterization of air-sea fluxes: updates and verification for the COARE algorithm, J. Clim., 16, 571-591, 2003.

Foken, T.: Micrometeorology, Springer, 2008.

Garratt, J.R.: The Atmospheric Boundary Layer, Cambridge University Press, 1983.

Hare, J.E., Hara, T., Edson, J.B., Wilczak, J.M.: A similarity analysis of the structure of air flow over surface waves, J. Phys. Oceanogr., 27, 1018-1037, 1997.

Hill, M. K., Brooks, B. J., Norris, S. J., Smith, M. H. and Brooks, I. M.: A compact lightweight aerosol spectrometer probe (CLASP), J. Atmos. Oceanic Technol., 25, 1996-2006, 2008.

Hogstrom, U.: Review of some basic characteristics of the atmospheric surface layer, Boundary Layer Meteorology, 78, 215 – 246, 1996.

Hogstrom, U.: Non-dimensional wind and temperature profiles in the atmospheric surface layer – a re-evaluation, Boundary Layer Meteorology, 42, 55-78, 1988

Hogstrom, U., Hunt, J. C. R., Smedman, A-S.: Theory and measurements for turbulence spectra and variances in the atmospheric neutral surface layer, Boundary Layer Meteorology, 103, 101-124, 2002

Huebert, B.J., Blomquist, B.W., Yang, M.X., Archer, S.D., Nightingale, P.D., Yelland, M.J., Stephens, J., Pascal, R.W. and Moat, B.I.: Linearity of DMS transfer coefficient with both friction velocity and wind speed in the moderate wind speed range, Geophys. Res. Lett., 37, L01605, 2010.

Hicks, B. B. and Dyer, A. J., The spectral density technique for the determination of eddy fluxes, Quart. J. Roy. Meteor. Soc., 98, 838-844, 1972.

Hwang, P. A., Garcia-Nava, H., Ocampo-Torres, F. J., Dimensionally consistent similarity relation of ocean surface friction coefficient in mixed seas, J. Phys. Oceanogr., 41, 1227-1238.

Janssen, P. A. E. M.: On the effect of ocean waves on the kinetic energy balance and consequences for the inertial dissipation technique, J. Phys. Oceanogr., 29, 530-534, 1999

Janssen, P.: The interaction of Ocean Waves and Wind, Cambridge University Press, 2004.

Janssen, P.A.E.M., Komen, G.J.: Friction velocity scaling in wind wave generation, Bound. Layer Meteor., 38, 29-35, 1986.

Kaimal, J. C., Finnegan, J. J.: Atmospheric Boundary Layer Flows – their structure and measurements, Oxford University Press, 1984.

Kaimal, J. C. and Gaynor, J. E.: Another look at sonic anemometry, Boundary Layer Meteorol., 56, 401-410, 1991.

Kaimal, J.C., Wyngaard, J.C., Izumi and Y., Cote, O.R.: Spectral characteristics of surface-layer turbulence, Quart. J. R. Met. Soc., 98, 563-589, 1972

Kawai, T.: Structure of air flow separation over wind wave crests, Boundary Layer Meteorology, 23, 503-521, 1982

Kolmogorov, A. N., The local structure of turbulence in incompressible viscous fluid for very large Reynolds numbers, Proceedings of the Royal Society of London, Series A: Mathematical and Physical Sciences, 434, 15-17, 1980 (originally published in Russian, 1941)

Large, W.G, Pond, S.: Open ocean momentum flux measurements in moderate to strong winds, J. Phys. Oceanogr., 11, 324-336, 1981.

Large, W.G, Pond, S.: Sensible and latent heat flux measurements over the ocean, J. Phys. Oceanogr., 12, 464-482, 1982.

Lee, X., Massman, W. and Law, B.: Handbook of micrometeorology, Kluwer Academic Publishers, 2004.

Makin, V.K. and Mastenbroek, C.: Impact of waves on air-sea exchange of sensible heat and momentum, Boundary Layer Meteorology, 79, 279-300, 1996.

McBean, G. A. and Ellion, J. A.: The vertical transport of kinetic energy by turbulence and pressure in the boundary layer, J. Atmos. Sci., 32, 753-766, 1975.

McGillis, W.R., Edson, J.B., Hare, J.E., Fairall, C.W.: Direct covariance of air-sea CO_2 fluxes, J. Geophys. Res., 106, 16729-16745, 2001.

Miller, S. D., Hristov, T. S., Edson, J. B., and Friehe, C. A.: Platform motion effects on measurements of turbulence and air-sea exchange over the open ocean, J. Atmos. Oceanic Technol., 25, 1683-1694, 2008.

Miller, S.D., Marandino, C., Saltzman, E.S.: Ship based measurement of air-sea CO_2 exchange by eddy covariance, J. Geophys. Res., 115, D02304, 2010.

Moat B. I., Yelland, M. J., Pascal, R. W. and Prytherch, J.: Metadata for the WAGES instrumentation deployed on the RRS James Clark Ross between May 2010 and September 2011, National Oceanography Centre Internal Document 4, National Oceanography Centre, UK, 54pp, 2010.

Monin, A. S. and Obhukov, A. M.: Basic laws of turbulent mixing in the surface layer of the atmosphere, Tr. Akad., Nauk SSSR Geofiz. Inst, 24, 163-187, 1954

Monin, A. S. and Yaglom, A. M.: Statistical fluid mechanics, M. I. T. Press, 1971.

Norris, S. J., I. M. Brooks, M. K. Hill, B. J. Brooks, M. H. Smith, and D. A. J. Sproson, 2012: Eddy Covariance Measurements of the Sea Spray Aerosol Flux over the Open Ocean. J. Geophys. Res. 117, 2012.

Norris, S. J., I. M. Brooks, B. I. Moat, M. J. Yelland, G. de Leeuw, R. W. Pascal , B. J. Brooks: Field Measurements of Aerosol Production from Whitecaps in the Open Ocean. Ocean Science, 9, 133–145, 2013

Norris, S. J., I. M. Brooks, D. J. Salisbury: A Reynolds number parameterization of the sea-spray aerosol source flux, Geophys. Res. Letts. 40, 1-5, (IN PRESS), 2013.

Pascal, R. W., Yelland, M. J., Srokosz, M. A., Moat, B. I., Waugh, E. M., Comben, D. H., Cansdale, A. G., Hartman, M. C., Coles, D. G. H., Hsueh, P. C., Leighton, T. G.: A spar buoy for high-frequency wave measurements and detection of wave breaking in the open ocean, J. Atmos. Oceanic Technol., 28, 590-605, 2011

Paulson, C. A.: The mathematical representation of wind speed and temperature profiles in the unstable atmospheric surface layer, Journal of Applied Meteorology, 9, 857-861, 1970.

Pedreros, R., Dardier, G., Dupuis, H., Graber, H.C, Drennan, W.M., Weill, A., Geurin, C., Nacass, P.: Momentum and heat fluxes via the eddy correlation method on the R/V L'Atalante and an ASIS buoy, J. Geophys. Res., 108, C11, 2003.

Phillips, O. M.: The dynamics of the upper ocean, Cambridge University Press, 1977.

Pierson, W. J. and Moskovitz, L. A.: Proposed spectral form for fully developed wind seas based on the similarity theory of S. A. Kitaigorodskii, Journal of Geophysical Research, 69, 2181-5190, 1964.

Popinet, S., Smith, M. and Stevens, C.: Experimental and numerical study of turbulence characteristics of airflow around a research vessel, J. Atmos. Oceanic Technol., 21, 1575-1589, 2004.

Prytherch, J., Yelland, M. J., Pascal, R. W., Moat, B. I., Skjelvan, I. and Neill, C. C.: Direct measurements of the CO_2 flux over the ocean: Development of a novel method, Geophys. Res. Lett., 37, L03607, 2010a.

Prytherch, J., Yelland, M. J., Pascal, R. W., Moat, B. I., Skjelvan, I. and Srokosz, M. A.: Open-ocean gas transfer velocity derived from long term direct measurements of the CO_2 flux, Geophys. Res. Lett., 37, L23607, 2010b.

Reider, K.F. and Smith, J.A.: Removing wave age effects from the wind stress vector, J. Geophys. Res., 103, C1, 1363-1374, 1998.

Sahlee, E., Smedman, A.-S.,Rutgersson, A. and Hogstrom, U.: Spectra of CO_2 and water vapour in the marine atmospheric surface layer, Boundary Layer Meteorology, 126, 279-295, 2008.

Seber, G.A.F. and Wild, C.J.: Nonlinear Regression, Wiley-Interscience, 2003.

Sjoblom, A. and Smedman, A.: The turbulent kinetic energy budget in the marine atmospheric surface layer, J. Geophys. Res., 107(C10), 3142, 2002

Sjoblom, A. and Smedman, A.: Vertical structure in the marine atmospheric boundary layer and its implication for the inertial dissipation method, Boundary Layer Meteorology, 109, 1-25, 2003

Smedman, A., Hogstrom, U., Bergstrom, H., Rutgersson, A., Kahma, K. and Pettersson, H.: A case study of air-sea interaction during swell conditions, J. Geophys. Res., 104, 25833-25851, 1999.

Smedman, A., Hogstrom, U., and Sjoblom, A.: A note on velocity spectra in the marine boundary layer, Boundary Layer Meteorology, 109, 27-48, 2003.

Smith, S. D.: Wind stress and heat flux over the open ocean in gale force winds, J. Phy. Oceanogr., 10, 709-726, 1980.

Smith, S.D: Coefficients for sea surface wind stress, heat flux, and wind profiles as a function of wind speed and temperature, J. Geophys. Res., 93, 15467-15472, 1988

Sorensen, L.L. and Larsen, S.E: Atmosphere-surface fluxes of CO_2 using spectral techniques, Boundary Layer Meteorology, 136, 29-81, 2010.

Stull, R.B.: An introduction to boundary layer meteorology, Kluwer Acad., 1988.

Sun, J., Howell, J.F., Esbensen, S.K., Mahrt, L., Greb, C.M., LeMone, M.A.: Scale dependence of air-sea fluxes over the western equatorial pacific, J. Atmos. Sci., 53, 2997-3012, 1996.

Taylor, P.K., Yelland, M.J.: On the apparent 'imbalance' term in the turbulent kinetic energy budget, J. Atmos. Oceanic Technol., 17, 82-89, 2001.

Vickers, D. and Mahrt, L.: Quality control and flux sampling problems for tower and aircraft data, J. Atmos. Oceanic Technol., 14, 512-526, 1997.

Voronovich, V. and Kiely, G.: On the gap in the spectra of surface-layer atmospheric turbulence, Boundary Layer Meteorology, 122, 67-83, 2007.

Wanninkhof, R., Asher, W.E., Ho, D.T., Sweeney, C., McGillis, W.R.: Advances in quantifying air-sea gas exchange and environmental forcing, Annu. Rev. Mar. Sci., 2009.1, 213-244, 2009.

Wilczak, J.M., Oncley, S.P. and Stage, S.A.: Sonic anemometer tilt correction algorithms, Boundary Layer Meteorology, 99, 127-150, 2001.

Willis, G. E. and Deardorff, J. W.: On the use of Taylor's translation hypothesis for diffusion in the mixed layer, Quart. J. R. Meteor. Soc., 102, 817-822, 1976.

Woolf, D.K.: Parameterization of gas transfer velocities and sea state dependent wave breaking, Tellus, Ser. B, 57, 87-94, 2005.

Wyngaard, J. C. and Cote, O. R.: The budget of turbulent kinetic energy and temperature variance in the atmospheric surface layer, J. Atmos. Sci., 28, 199-200, 1971.

Yelland, M.J., Moat, B.I., Taylor, P.K, Pascal, R.W., Hutchings, J. and Cornell, V.C..: Wind stress measurements from the open ocean corrected for airflow distortion by the ship, J. Atmos. Oceanic Technol., 28, 1511-1526, 1998.

Yelland, M.J., Pascal, R.W., Taylor, P.K. and Moat, B.I.: Autoflux: an autonomous system for the direct measurement of the air-sea fluxes of CO_2, heat and momentum, J. Operational Oceanography Oceanic Technol., 2(1), 15-23, 2009.

Yelland, M.J. and Moat, B.I.: CFD model estimates of the airflow distortion over research ships and the impact on momentum flux measurements, J. Atmos. Oceanic Technol., 19, 1477-1499, 2002.